

Overview of the MOSAiC expedition – Snow and Sea Ice

Marcel Nicolaus¹, Donald K. Perovich², Gunnar Spreen³, Mats A. Granskog⁴, Luisa von Albedyll¹, Michael Angelopoulos⁵, Philipp Anhaus¹, Stefanie Arndt¹, H. Jakob Belter¹, Vladimir Bessonov⁶, Gerit Birnbaum¹, Jörg Brauchle⁷, Radiance Calmer⁸, Estel Cardellach⁹, Bin Cheng¹⁰, David Clemens-Sewall², Ruzica Dadic¹¹, Ellen Damm¹, Gijs de Boer^{8,12,13}, Oguz Demir¹⁴, Klaus Dethloff⁵, Dmitry V. Divine⁴, Allison A. Fong¹, Steven Fons^{15,16}, Markus M. Frey¹⁷, Niels Fuchs^{1,18}, Carolina Gabarró¹⁹, Sebastian Gerland⁴, Helge F. Goessling¹, Rolf Gradinger²⁰, Jari Haapala¹⁰, Christian Haas^{1,3}, Jonathan Hamilton^{8,13}, Henna-Reetta Hannula¹⁰, Stefan Hendricks¹, Andreas Herber¹, Céline Heuzé²¹, Mario Hoppmann¹, Knut Vilhelm Høyland²², Marcus Huntemann³, Jennifer K. Hutchings²³, Byongjun Hwang²⁴, Polona Itkin^{20,25}, Hans-Werner Jacobi²⁶, Matthias Jaggi²⁷, Arttu Jutila¹, Lars Kaleschke¹, Christian Katlein¹, Nikolai Kolabutin⁶, Daniela Krampe¹, Steen Savstrup Kristensen²⁸, Thomas Krumpen¹, Nathan Kurtz¹⁵, Astrid Lampert²⁹, Benjamin Allen Lange⁴, Ruibo Lei³⁰, Bonnie Light³¹, Felix Linhardt³², Glen E. Liston²⁵, Brice Loose³³, Amy R. Macfarlane²⁷, Mallik Mahmud³⁴, Ilkka O. Matero¹, Sönke Maus²², Anne Morgenstern¹, Reza Naderpour³⁵, Vishnu Nandan³⁶, Alexey Niubom⁶, Marc Oggier^{4,37}, Natascha Oppelt³², Falk Pätzold²⁹, Christophe Perron³⁸, Tomasz Petrovsky⁶, Roberta Pirazzini¹⁰, Chris Polashenski^{2,39}, Benjamin Rabe¹, Ian A. Raphael², Julia Regnery¹, Markus Rex⁵, Robert Ricker¹, Kathrin Riemann-Campe¹, Annette Rinke⁵, Jan Rohde¹, Evgenii Salganik²², Randall K. Scharien⁴⁰, Martin Schiller¹, Martin Schneebeli²⁷, Maximilian Semmling⁴¹, Egor Shimanchuk⁶, Matthew D. Shupe^{8,13}, Madison M. Smith³¹, Vasily Smolyanitsky⁶, Vladimir Sokolov⁶, Tim Stanton⁴², Julianne Stroeve³⁶, Linda Thielke³, Anna Timofeeva⁶, Rasmus Tage Tonboe⁴³, Aikaterini Tavri⁴⁰, Michel Tsamados⁴⁴, David N. Wagner^{27,45}, Daniel Watkins²³, Melinda Webster³⁷, Manfred Wendisch⁴⁶

25

¹ Alfred-Wegener-Institut Helmholtz-Zentrum für Polar- und Meeresforschung, Bremerhaven, Germany

² Thayer School of Engineering, Dartmouth College, Hanover, NH, USA

³ University of Bremen, Bremen, Germany

30

⁴ Norwegian Polar Institute, Fram Centre, Tromsø, Norway

⁵ Alfred-Wegener-Institut Helmholtz-Zentrum für Polar- und Meeresforschung, Potsdam, Germany

⁶ Arctic and Antarctic Research Institute, Saint Petersburg, Russia

⁷ German Aerospace Center (DLR), Institute of Optical Sensor Systems, Berlin, Germany

35

⁸ CIRES, University of Colorado Boulder, Boulder, CO, USA

⁹ Instituto de Ciencias del Espacio (ICE-CSIC/IEEC), Barcelona, Spain

¹⁰ Finnish Meteorological Institute, Helsinki, Finland

¹¹ Victoria University of Wellington, Antarctic Research Centre, Wellington, New Zealand

¹² Integrated Remote and In Situ Sampling, University of Colorado Boulder, Boulder, CO, USA

40

¹³ NOAA Physical Sciences Laboratory, Boulder, CO, USA

¹⁴ The Electro Science Laboratory, The Ohio State University, Columbus, OH, USA

¹⁵ NASA Goddard Space Flight Center, Greenbelt, MD, USA

¹⁶ University of Maryland, College Park, MD, USA

45

¹⁷ British Antarctic Survey, Natural Environment Research Council, Cambridge, United Kingdom

¹⁸ Center for Earth System Sustainability, Institute of Oceanography, Universität Hamburg, Hamburg, Germany

¹⁹ Barcelona Expert Center (BEC) and Institute of Marine Science (ICM-CSIC), Barcelona, Spain

20 ²⁰ UiT - The Arctic University of Norway, Tromsø, Norway
50 ²¹ Department of Earth Sciences, University of Gothenburg, Gothenburg, Sweden
²² Norwegian University of Science and Technology, Trondheim, Norway
²³ Oregon State University, Corvallis, OR, USA
²⁴ University of Huddersfield, Huddersfield, United Kingdom
²⁵ Cooperative Institute for Research in the Atmosphere, Colorado State University, Fort
55 Collins, CO, USA
²⁶ Institute for Geosciences and Environmental Research (IGE), CNRS/Univ. Grenoble
Alpes/IRD/G-INP, Grenoble, France
²⁷ WSL Institute for Snow and Avalanche Research SLF, Davos, Switzerland
²⁸ Technical University of Denmark (DTU), Kongens Lyngby, Denmark
60 ²⁹ Technische Universität Braunschweig, Institute of Flight Guidance, Braunschweig, Germany
³⁰ Key Laboratory for Polar Science of the MNR, Polar Research Institute of China, Shanghai,
China
³¹ Polar Science Center, Applied Physics Lab, University of Washington, Seattle, USA
³² Christian-Albrechts-Universität zu Kiel, Institut für Geographie, Kiel, Germany
65 ³³ The University of Rhode Island, Kingston, RI, USA
³⁴ University of Calgary, Calgary, Canada
³⁵ Eidg. Forschungsanstalt für Wald, Schnee und Landschaft, Birmensdorf, Switzerland
³⁶ University of Manitoba, Winnipeg, Canada
³⁷ University of Alaska Fairbanks, Fairbanks, AK, USA
70 ³⁸ Takuviq Joint International Laboratory, Laval University (Canada)-CNRS (France), Québec
City, Canada
³⁹ U.S. Army Cold Regions Research & Engineering Laboratory, Wainwright, AK, USA
⁴⁰ University of Victoria, Victoria, BC, Canada
⁴¹ German Aerospace Center DLR, Institute for Solar-Terrestrial Physics, Neustrelitz, Germany
75 ⁴² Naval Postgraduate School and Moss Landing Marine Laboratories, Moss Landing, CA, USA
⁴³ National Space Institute, Lyngby, Denmark
⁴⁴ University College London, London, United Kingdom
⁴⁵ École Polytechnique Fédérale de Lausanne, Lausanne, Switzerland
⁴⁶ Leipzig Institute for Meteorology, University of Leipzig, Leipzig, Germany
80

Abstract

Year-round observations of the physical snow and ice properties and processes that govern the ice pack evolution and its interaction with the atmosphere and the ocean were conducted 85 during the Multidisciplinary drifting Observatory for the Study of Arctic Climate (MOSAiC) expedition of the research vessel *Polarstern* in the Arctic Ocean from October 2019 to September 2020. This work was embedded into the interdisciplinary design of the five MOSAiC 90 teams, studying the atmosphere, the sea ice, the ocean, the ecosystem and biogeochemical processes. The overall aim of the snow and sea ice observations during MOSAiC was to characterize the physical properties of the snow and ice cover comprehensively in the central 95 Arctic over an entire annual cycle. This objective was achieved by detailed observations of physical properties, and of energy and mass balance of snow and ice. By studying snow and sea ice dynamics over nested spatial scales from centimeters to tens of kilometers, the variability across scales can be considered. On-ice observations of in-situ and remote sensing 100 properties of the different surface types over all seasons will help to improve numerical process and climate models, and to establish and validate novel satellite remote sensing methods; the linkages to accompanying airborne measurements, satellite observations, and results of numerical models are discussed. We found large spatial variabilities of snow metamorphism and thermal regimes impacting sea ice growth. We conclude that the highly variable snow cover needs to be considered in more detail (in observations, remote sensing and models) to better understand snow-related feedback processes. The ice pack revealed rapid transformations and motions along the drift in all seasons. The number of coupled ice-ocean interface processes observed in detail are expected to guide upcoming research with respect to the changing Arctic sea ice.

105 **1 Gaps of knowledge**

Sea ice and its snow cover make the Arctic Ocean distinct from most other oceans; they control energy transfer and important interactions between the atmosphere and the ocean. Therefore, they require a realistic representation in Arctic climate models, which are needed to improve our understanding of causes and consequences of the currently observed dramatic 110 changes of the Arctic climate system (Thoman et al., 2020). Although model projections are continuously improved and becoming more consistent in forecasting the further decline of the Arctic sea ice cover, they still differ considerably on the rate of the decline (AMAP, 2017).

115 After the pioneering drift of Fridtjof Nansen with his vessel *Fram* (1893–1896) (Nansen, 1897), numerous expeditions were performed to study the properties and interactions of Arctic sea ice and its snow cover with the atmosphere and the ocean. Most of these studies were internationally coordinated activities using icebreakers. Furthermore, 41 Russian North Pole drifting ice camps were established between 1937 and 2015 (Frolov et al., 2005). Only a few 120 studies were conducted observing the evolution of sea ice and snow cover during different seasons or over a full annual cycle. During the International Geophysical Year (1957–1958), sea ice heat and mass balance measurements were made at the Ice Station Alpha in the Beaufort Sea (Untersteiner, 1961). The Arctic Ice Dynamics Experiment (AIDJEX) focused on understanding ice mechanics and dynamics during the year-long drifting ice camp in the Beaufort Sea from 1975 to 1976 (Untersteiner et al., 2007). The international Surface Heat 125 Budget of the Arctic Ocean (SHEBA) field campaign was a year-long drift of the Canadian Coast Guard research icebreaker *Des Groseilliers* in the Beaufort and Chukchi Seas from 1997 to 1998. SHEBA focused on understanding the ice albedo and cloud radiation feedback mechanisms to improve climate models (Perovich et al., 1999). During the International Polar Year 2007/2008, snow and sea ice processes were studied along the drift of the schooner *Tara* (Gascard et al., 2008; Nicolaus et al., 2010; Haas et al., 2011). Between 2002 and 2008, 130 Canadian Arctic programs involved the overwintering of the Canadian Coast Guard research icebreaker *Amundsen* to study the role of sea ice (Fortier and Cochran, 2008; Barber et al., 2010). The multi-disciplinary Norwegian young ICE (N-ICE2015) expedition using the Norwegian research vessel *Lance* was carried out from January to June 2015. N-ICE2015 135 focused on the transition processes from multi-year to younger and thinner sea ice in the Arctic Ocean. It spent nearly 6 months studying atmosphere-ice-ocean-ecosystem interactions in an ice pack dominated by relatively thin (< 1.5 m) first year ice (FYI) and second year ice (SYI) (Granskog et al., 2018).

140 Beyond these crewed programs, autonomous drifting buoys, such as those coordinated by the International Arctic Buoy Programme (Rigor and Ortmeyer, 2003), observe annually the atmospheric, snow, sea ice, and ocean properties of the Arctic sea ice. Sea ice observations and data from airborne campaigns build another important source of Arctic snow and sea ice data (e.g., Haas et al., 2010; Kwok et al., 2017; Lawrence et al., 2018; MacGregor et al., 2021), 145 supplemented by sporadic measurements collected by adventurers (Gerland and Haas, 2011). Numerous satellite observations provide an Arctic-wide perspective of sea ice properties including extent, concentration, thickness, type, drift, snow cover, and others. Passive microwave satellites have provided a sea ice climatology over more than 40 years, but they lack details for many ice-related processes (Kern et al., 2019). To establish new satellite products, coordinated ground truth observations are required (Gerland et al., 2019; König et al., 2019).

As a result of past expeditions, the understanding of the role of snow and sea ice in the Arctic and its influence on global climate has improved in recent decades. However, there are still significant knowledge gaps (Webster et al., 2018; Gerland et al., 2019) in quantifying the interactions and feedback mechanisms between the physical, ecological, and biogeochemical processes. Furthermore, an accurate representation of sea ice effects on biology and biogeochemistry needs to be better understood. To contribute to solving these problems, the work of the Multidisciplinary drifting Observatory for the Study of Arctic Climate (MOSAiC) snow and sea ice team (in short ICE team) aims to achieve five overarching goals:

- Characterize the properties of snow and ice cover and understand the processes that govern these properties,
- Determine the snow and sea ice mass and freshwater balances,
- Quantify the partitioning of solar radiation between the snow, the sea ice, and the ocean,
- Describe the spatial variability and temporal evolution of the snow and ice cover, and
- Integrate snow and sea ice measurements with the atmosphere, ocean, and biosphere of the coupled Arctic system.

To achieve these main goals, a coordinated, integrated, and interdisciplinary approach was implemented as part of the MOSAiC expedition. Section 2 introduces the MOSAiC expedition and explains the concept of the snow and sea ice research program. The work program and a synopsis of the resulting data sets are presented in Section 3. In Section 4, the methodological and conceptual advances, and exemplary results from two case studies during one week of winter and one week of summer observations are shown. They result in a general description of the seasonal changes of the ice pack and the associated challenges of consistent and integrated observations of the coupled system components. Finally, linkages to the different Arctic sub-systems, numerical modelling, and satellite observations are discussed in Section 5. Section 6 provides the major conclusions of this paper.

180 **2 Methods and approach**

The MOSAiC field measurements started with the departure of the German research ice breaker *Polarstern* (Alfred-Wegener-Institut Helmholtz-Zentrum für Polar- und Meeresforschung, 2017) from Tromsø, Norway, on September 20, 2019, and ended with the arrival of the vessel on October 12, 2020, in Bremerhaven, Germany. Key dates are summarized in Table 1 and a map is shown in Figure 1. The observational year was divided into 5 legs: Leg 1 included the set-up of the first central observatory (CO1, ice camp plus installations on *Polarstern*) and was supported by the Russian research ice breaker *Akademik Fedorov*. *Akademik Fedorov* performed most of the deployment of the distributed network (DN). The DN consisted of an hierarchy of autonomous systems deployed on ice floes surrounding the CO at 3-40 km distance to measure atmospheric and oceanic lateral gradients and increase sampling the highly heterogeneous ice pack properties. The network consisted of more than 100 simple position nodes, 8 nodes of medium instrumentation (M-sites) and 3 nodes of large sensor suites (L-sites). A more detailed description of the DN is under development, led by B. Rabe. The winter Leg 2 and spring Leg 3 continued the work on CO1, before *Polarstern* had to end the (manned) Drift1 and leave the floe, for logistical reasons, on May 16, 2020. The autonomous stations on CO1 and in DN1 continued the (unmanned) drift and recorded data while the vessel performed logistical operations in Svalbard. Afterwards, *Polarstern* returned to the original ice floe, but at a different location some hundred meters away. Leg 4 continued the drift with the new CO2 over summer until the decay of the floe in Fram Strait (between Greenland and Svalbard; Figure 1) on 31 July 2020. This ended the Drift2 and only a few autonomous devices continued the drift of CO1, CO2, and DN1. After the final rotation of personnel, *Polarstern* travelled back into the ice and started Drift3 with the set-up of CO3 and DN2 on August 21, 2020, near the North Pole. Drift3 ended on September 20, 2020, when the vessel started the return voyage. A publication with details on the expedition in general and its logistics is under development led by M. Rex.

Figure 1: Drift tracks of the central observatories (CO) of MOSAiC in 2019–2020.

Table 1: Key dates of the MOSAiC expedition.

210 To achieve the main goals of MOSAiC, a coordinated, integrated, and interdisciplinary approach was implemented, as a collaboration of five scientific teams: the atmosphere (ATMOS) team, the snow and sea ice (ICE, this manuscript) team, the oceanography (OCEAN) team, the ecosystem (ECO) team, and the biogeochemistry (BGC) team. The work on physical snow and sea ice processes and properties was organized in 13 tasks, which are described in the sub-sections of this chapter (see also Text S1 with Figure S1). All tasks comprise elements of observations and numerical modelling, while the balance between these elements differs between the tasks. Additional details on some methods are given in Text S2, including a list of short names and acronyms in Table S2:

220

1. General snow and ice observations
2. Snow measurements and sampling
3. Ice coring
4. Mass balance observations
5. Terrestrial laser scanning
6. Optical measurements
7. Melt pond observations
8. Sea ice dynamics

9. Ridge observations
10. Transect measurements
230 11. Remotely operated vehicle (ROV) observations
12. Helicopter observations
13. On-ice remote sensing

235 The snow and sea ice measurements were distributed over the entire CO (Figure 2). A detailed description of all three COs with additional maps and details on installations is under preparation by the project team led by M. Nicolaus. While the set-up of the CO changed between legs due to ice dynamics and ship relocation, its general layout is exemplified in the map in Figure 2, which shows the CO1 ice camp shortly before the temporary departure of *Polarstern* at the end of Leg 3.

240 First results with a focus on snow and sea ice conditions have been published, e.g., on the history of the ice drift prior to the MOSAiC expedition (Krumpen et al., 2020), on the ice conditions from satellite observation along the drift track in previous years (Krumpen et al., 245 2021), on the representativeness of the selected ice floe (Belter et al., 2021), on the linkages to the general atmospheric circulation (Dethloff et al., 2021), on sea ice remote sensing methods (Munoz-Martin et al., 2020; Stroeve et al., 2020; Semmling et al., 2021), and on the platelet ice accumulation in winter (Katlein et al., 2020).

250 Figure 2: Main sites and installations in the central observatory at the end of Leg 3 (CO1).

2.1 General snow and ice observations

255 The general snow and ice observations and specific activities were performed during all legs to document the general snow and ice conditions and to support data interpretation afterwards. Mapping activities of discrete measurements, installations, and operations on the ice were also organized in this task. Its activities included:

- (1) Acquiring timelapse photos of the surroundings of the vessel with a 360-degree panorama (Panomax) camera mounted above the crow's nest. Each photo has a resolution of 15,680x2,048 pixels and photos were taken at 20-minute intervals (72 photos per day).
- (2) Recording standard sea ice observations daily (on transits hourly) from the bridge following the protocol of the Arctic Shipbourne Sea Ice Standardization Tool (Hutchings and Faber, 260 2018). The aim of these observations was to describe the surrounding conditions over a 10-minute period within a radius of 1.5 nautical miles around the vessel, including the polar night.
- (3) Documenting the on-ice work by establishing a local floe-based x, y coordinate system to provide the relative locations of the various sites (FloeNavi system), because measurements on sea ice have the particular challenge that the ice floes are in constant movement. In addition, geographic positions were recorded to allow reference to any other measurements, 265 in particular airborne and satellites, that are not referenced to the floe.
- (4) Acquiring visible and thermal photography from helicopters and drones to provide information about sea ice surface conditions, to support mapping of the main floe, and to generate digital elevation models of the surface. Visual floe maps and digital elevation models were created by stitching photographs from single flights. The final images were geo-referenced to the local x-y coordinate system.
- (5) Upgrading, before the start of the drift expedition, the Electronic Charting System on board *Polarstern*, for receiving and displaying various satellite and weather data in near real time.

275 The effort was focused on the charting of weather forecast products provided by the German

Weather Service. In addition, model-based ice drift forecasts were included, as well as a combination of various new satellite products.

(6) Documenting the on-ice work almost daily on board and synchronizing with land as the 'MOSAiC LogBook' to inform the project consortium on details of the ongoing work.

280

2.2 Snow measurements and sampling

285

The overarching goal of the snow measurements was to characterize the spatial and temporal variability of snow over different sea ice types (e.g., FYI, SYI and ridges) during an entire annual cycle. During the melt season, techniques used to investigate the snow were applied to the uppermost layer of the melting ice cover, the so-called "surface scattering layer" (SSL). The snow measurements during MOSAiC were conducted with the aim to improve snow models, and subsequently to improve climate models and remote sensing retrieval algorithms, and in support of all MOSAiC teams. Snow is one of the most insulative naturally occurring materials on Earth (Webster et al., 2018), and one of the most efficient reflectors of incident solar radiation (Warren et al., 1983). Snow on sea ice therefore acts as an effective barrier between the atmosphere and the ocean, preventing both heating of the upper ocean in summer and cooling of the ocean in winter. While the bulk physical properties of snow on sea ice (e.g., snow depth, snow density, snow thermal conductivity, snow reflectivity, albedo) and the resulting stratigraphy have been studied previously, data on the spatial heterogeneity of the optical and thermal properties of snow on sea ice and the relationship between these properties and their governing processes are limited. Snow measurements during MOSAiC ranged from microscale (micrometer) to local scale (approximately 1000 m) to address these properties across scales. The following novel instruments were used during MOSAiC to measure physical properties of snow:

300

- The Snow Micro Pen (SMP), a penetrometer (Proksch et al., 2015) for fast retrieval of the vertical profile of snow stratigraphy, snow density, and specific surface area, with a high vertical resolution (better than 1 mm). The SMP measures vertical profiles of snow layers at one location. By repeating samples over a large area, micro-, macro- and regional scale properties can be linked. SMP was used on snow profiles and transects. Overall, 6,959 SMP profiles were measured.
- An X-ray microtomograph (micro-CT, Scanco Medical micro-CT 9; Calonne et al., 2014), which was installed on board *Polarstern* and allowed measurements of snow microstructure on quasi in-situ samples. We used the micro-CT to measure the full snow profiles throughout the year, as well as on the SSL, lead and pond ice, and sea ice cores. Overall, 614 samples were analyzed with the micro-CT.
- Near Infrared (NIR) photography (Matzl and Schneebeli, 2006) to characterize the specific surface area of snow profiles as well as the snow and SSL surfaces. During MOSAiC, photographs at 850 nm and 940 nm were taken for each profile/surface scene. Overall, some 600 profile/surface scenes were photographed using NIR.
- Structure from motion photograph sets to derive elevation data. Based on these data, high spatial resolution digital elevation models were created at each snow pit location, and sometimes along transects, of the surface and of the snow–ice interface. These "mini digital elevation models" will be used to determine small scale (millimeter) surface roughness that is relevant for optical modelling and satellite retrievals, and link data to coarser-scale digital elevation models obtained by terrestrial and airborne laser scanning. Overall, some 300 structure from motion sets were taken during MOSAiC.

Snow observations were collected mainly in specific areas assigned to snow measurements. Those areas included the prevalent types of sea ice, namely FYI (e.g., Snow1), SYI (e.g., Snow2),

ridges and new ice in leads, as highlighted by yellow patches in Figure 2. Additional 325 measurements were performed across the COs to connect physical snow properties to relevant processes that were studied by other teams. The team members conducted about 600 snow pit measurements of different types:

- “Type C” snow pits characterized the vertical profile of the snowpack and consisted of SMP measurements only.
- “Type B” snow pits included density, snow water equivalent (SWE), temperature, and salinity measurements in addition to observations of Type C.
- “Type A” snow pits included the full suite of snow measurements, adding snow sampling (see below), micro-CT scans, SMP transect (to either side of pit), NIR photography, structure from motion pictures, and snow sampling for a wide range of 335 constituents, in addition to observations of Type B and C.

For practical reasons, this perfect scheme of snow pit types was not always followed in every pit. We performed a comprehensive snow sampling program, which was centrally organized and coordinated across all scientific teams. Snow samples co-located with the physical 340 measurements were taken for analysis of salinity, water and sulphur stable isotopes, major ions, halogens and halocarbons, beryllium, black carbon, marine sugars, organic acids, microplastics and ice-nucleating particles. Snow sampling was combined with snow pit measurements whereby the frequency and number depended on the purpose of the snow sample. This approach ensured that all samples from each sampling event were taken at the 345 same site(s) and in a consistent and reproducible manner facilitating the co-location with the physical properties of the snow. In addition, dielectric permittivity measurements were made at 50 MHz to invert snow wetness during melting conditions.

Figure 3 shows the temporal distribution of snow pits. Distributed observations of physical 350 snow properties on transects, and of snow depth (Section 2.10), and observations of snow surface position with terrestrial and airborne laser scanner (TLS Section 2.5 and ALS Section 2.12) will be used to upscale these point observations. Collectively, these measurements provide a comprehensive characterization of the snow cover, enabling synthesis studies on snow evolution, spatial variability, energy budget and heat fluxes, remote sensing algorithm development and towards improved parameterizations in climate models.

355 Figure 3: Snow and sea ice observations during the field phase of MOSAiC.

2.3 Ice coring

The primary aim of the ice coring work was to capture the seasonal evolution of sea ice 360 physical properties over a full year, for both level FYI and level SYI at 5-cm vertical resolution, and to document the differences between FYI and older ice. This work was performed at two main coring sites (Figure S2 with Tables S2 and S3), one on FYI and the other on SYI, which was the oldest ice at the start of MOSAiC. We used the approach recommended by Oggier et al. (2020) to section the ice cores, relative to both the ice surface and ice bottom (Section 4.2), 365 to better capture the processes at the surface and bottom interfaces. The physical properties affect energy and matter fluxes and ecosystem processes in sea ice, and are also important to the remote sensing of sea ice (Section 2.13). The ice coring work captures the seasonal evolution of level ice thickness, temperature, salinity and density. At each coring event, temperature profiles were measured using a thermistor probe into holes drilled at 5 or 10 cm 370 intervals within 2–3 minutes of core extraction. Two cores collected within 50 cm of the temperature core were cut in sections and stored in sealed containers for transport to the

ship, after noting total length and fractures. Onboard, bulk salinity was measured on melted ice samples, and density was measured using the hydrostatic density method (Pustogvar and Kulyakhtin, 2016). The brine volume fraction can be derived from these measurements. Two 375 additional cores were collected for textural and microstructure analysis: one for thin sections and a second for micro-CT scans (Section 2.2). Bottom and surface sections (in most cases the lower and uppermost 10 cm of ice cores) were imaged on board using the micro-CT on *Polarstern*. The remaining ice cores were archived for more detailed studies of texture and 380 microstructure at home laboratories after the expedition. In the sunlit period, ice cores were also collected to measure the optical properties at the home lab (Section 2.6). Coring was coordinated with the snow task, and often the coring was associated with a simple snow pit (which typically included temperature, density, salinity and sampling for oxygen isotopes; Section 2.2) supporting the interpretation of the ice core data. Coring was conducted in close 385 collaboration with the ECO and BGC teams.

390 In addition to the time series data from the main coring sites (Figure S2), the BGC team also observed the temporal evolution of both FYI and SYI at a number of additional sites (primarily salinity and temperature) coincidently with their own work. In addition, sediment laden ice cores were collected for analysis jointly with the BGC team and an occasional ice core was collected for analysis of microplastics. These ice cores complement the observations made by 395 the ICE team and provide more information on spatial variability. Coring was also done repeatedly in ridges (Section 2.9) and for ice mechanical properties (Section 2.8). Opportunistic sampling was done especially for thin young ice in leads and linked to remote sensing work during some events and occasionally in the DN. The collected data set captures the seasonal evolution of FYI, from early growth and new saline ice to mature FYI and the rapid 400 desalination in summer (Section 4). While the FYI that had survived the previous summer melt became SYI at the beginning of the campaign, the refreezing and new ice growth at the bottom of SYI could be observed until its summer decay. An overview of the ice coring activities by the ICE team is shown in Figure 3, and a list of existing ice cores is referenced in the data availability section.

2.4 Mass balance observations

The goal of the mass balance observations was to document the amount and spatial variability 405 of ice growth during winter and surface and bottom ice melt during summer. Mass balance observations provide insight on the relative contributions of the atmosphere and ocean to changes in the sea ice thickness and snow depth. Multiple sites sampling new ice, FYI, SYI, deformed ice, undeformed ice, and ponded ice were included to comprehensively address the spatial variability of sea ice mass balance. The in-situ mass balance measurements were made both autonomously and manually with 37 digital temperature chains, 4 sea ice mass balance 410 buoys (IMB) of different types (e.g., Polashenski et al., 2011; Jackson et al., 2013), 20 Snow Buoys (Nicolaus et al., 2021), and 120 manual ice thickness gauge/ablation stake pairs. The temperature chains and IMBs recorded vertical profiles of temperature of the air through the snow and ice into the upper ocean, as well as (for some IMBs) the positions of surface and bottom interfaces using acoustic rangefinders. Analysis of temperature chain data manually 415 and by algorithms are also used to determine the position of the air-snow or -ice and the ice-ocean interfaces (Hoppmann et al., 2015; Cheng et al., 2020). Manual measurements at the ablation stake sites also provided a time series of the sea ice surface and bottom position changes. Thicknesses measured from ice cores collection and laser scanning measurements contributed to the snow and sea ice mass balance measurements (Sections 2.3, 2.5 and 2.12).

420 Together, these multiple methods of observing ice surface and bottom position are used to calculate time series of snow depth and ice thickness, ice growth, surface melt, and bottom melt. In combination with transects (Section 2.10) this approach provides a comprehensive view of the sea ice mass balance (in space and time) and the best local (thermodynamic) and best spatial (dynamic) information. To complement the mass balance observations, systems
425 for atmosphere and ocean measurements were co-located on the same sites.

2.5 Terrestrial laser scanning

430 The goal of the terrestrial laser scanning (TLS) was to map the snow and ice surface topography and how it changed in time and space throughout the seasonal cycle. Using the eye-safe Riegl VZ1000 TLS during winter and the non-eye-safe Riegl VZ6000 TLS during summer allowed large aerial scans. Analysis of these data is being used to link these changes with other in-situ measurements of snow and ice properties and spatially extend point measurements of snow and ice properties. TLS measurements were used to map an area of approximately 0.5 km² every two weeks with a centimeter-scale vertical resolution and
435 decimeter-scale or better horizontal resolution. The same region was mapped with 42 scans during the drift with CO1 from October 18, 2019, to May 9, 2020, (Figure 3) and included most of the snow pit measurement sites, most of the mass balance observation sites as well as the southern loop of the transect, all of the albedo transects in spring, portions of the strain gauge installations, the area studied from beneath the ice at ROV sites (ROV 2.0 and 3.0 in Figure 2),
440 the on-ice remote sensing instruments, and the on-ice meteorological installations at Met City (Sections 2.2, 2.4, 2.6, 2.11, 2.13). This co-location of the various methods will allow linked data processing, while the impact of surface destruction on the TLS results through other activities is minor given the very small fraction (< 1%) of impacted surface area. Summertime TLS observations were more limited due to safety and logistics but included areas of snow
445 pits, albedo, ponds, and other surface property measurements. The TLS observations are used to generate a time series of ice dynamics, changes in atmospheric form drag, and snow accumulation, redistribution and melt. TLS measurements can be used to infer material properties throughout the mapped region by upscaling the vertical profile measurements of snow and ice physical properties made by other instruments.

450 2.6 Optical measurements

455 The objective of the “Optics” task was to quantify the partitioning of solar radiation within and beneath the ice cover during the sunlit season. The quantities measured included albedo, transmittance, and light extinction in snow, sea ice and the underlying water. A variety of sensors (measuring either broadband, spectral or photosynthetically active radiation) were used for measuring repeat-visit survey lines and grids in addition to fixed-point study sites. The albedo measurements included surface survey lines, multiple fixed site installations, unmanned aerial systems (e.g., the drones HELiX and Mavic and the Spectra Quadrocopter),
460 helicopter-borne instrument platforms and the tethered balloon. Transmittance measurements included repeat under-ice surveys using an ROV (Section 2.11) and site-specific measurements using an L-arm photosynthetically active radiation sensor. In-ice extinction and inherent optical property measurements were carried out at specific locations using profiling sensor arrays frozen into the ice (light chains and light harp) and a spatially resolved reflectance probe lowered into auger holes. Light extinction within the water column beneath the ice cover was estimated using sensors mounted on the ocean CTD, and the ROV was also equipped with a number of optical sensors.

470 Sensors were also deployed on radiation stations to autonomously collect albedo, transmittance and water column radiation at fixed locations throughout the season. In addition to these time series, specific experiments were carried out to assess the response of spectral albedo to specific events or processes: 1) snow during early summer melt, 2) diurnal variability during both melt and freeze-up, 3) the removal and formation of a surface scattering layer, and 4) rain on new snow. Additionally, ice was sampled for investigation of the linkages of optical and structural properties to be carried out in freezer laboratories at home institutions (Section 2.3).

475 Ongoing investigations of the spatial heterogeneity of the surface albedo at various horizontal scales will be aided by the drone-based spectral and broadband albedo measured along grids and horizontal transects at various heights above the ice surface. The vertical profiles of albedo recorded from drones will be crucial for determining the contributions of various 480 surface features (melt ponds, ridges, flat-ice, leads) to the areal-averaged albedo. These measurements enable scaling from ground-based observations (meter-to-tens-of-meters footprint), to satellite observations (tens-to-hundreds-of-meters footprint) and large-grid model outputs. Moreover, high spatial resolution hyperspectral albedo measurements 485 collected from drone-mounted cameras will help relate the scattering properties of each surface feature to the snow and ice microstructure properties observed at the surface.

2.7 Melt pond observations

Melt ponds play a key role in energy exchange between atmosphere and ocean in the Arctic summer because they substantially reduce surface albedo of sea ice. Compared to bare ice, 490 melt ponds reflect less solar energy to the atmosphere and transmit more solar energy into the ice underneath and the ocean, thus fostering further sea ice melt (Light et al., 2008; Nicolaus et al., 2012). At present, a synoptic view of pond evolution, distribution and depth using airborne and satellite data is still limited. The main objective of the Ponds task was to 495 provide field and airborne data (Section 2.12) of the physical pond characteristics (e.g., size and shape distributions) to improve the understanding of the spatio-temporal development during all stages of pond evolution. These characteristics include pond area fraction, size, shape, and number. To improve pre-processing of airborne and satellite data (i.e., atmospheric correction, correction of adjacency effects; König et al., 2019), the spectral 500 signature of the different surface types on the floe were measured using hand-held water color spectroradiometers, a hyperspectral camera, and a goniometer. Up- and downwelling broadband irradiance data as well as multi-spectral imagery are available from drone surveys, helicopter flights and satellite observations (Sections 2.6 and 2.12). To assist a proper 505 reflectance calibration of water surfaces we used a remotely controlled boat equipped with water color spectroradiometers. Above and below water spectral measurements were used to assess the optical properties of pond water (attenuation coefficient, inherent optical 510 properties; König and Oppelt, 2020). In addition to the radiometer measurements, the field measurements also included pond depth as well as chlorophyll content, salinity and temperature of pond water. To assess the absorption coefficient of the dissolved and particulate matter, water samples were taken and analyzed in the *Polarstern* lab using a point-source integrating-cavity absorption meter. Micro-CT samples were processed from frozen melt ponds to derive optical properties.

2.8 Sea ice dynamics

One of the key questions of MOSAiC is how sea ice moves and deforms. The dynamics and mechanics of the ice around the *Polarstern* and its interaction with the ship, ocean and atmosphere were monitored throughout the drift. We aimed to examine the spatial and temporal distribution of ice motion and ice stress, and to determine how they vary locally, regionally, and seasonally in relation to the physical properties of the ice. The CO observations were coordinated with satellite and airborne remote sensing (Section 2.12) monitoring ice drift, ice morphology and floe size. Drift and strain-rate (divergence, shear and vorticity) of the ice pack were measured over multiple nested scales, from hundreds of kilometers in a wide array of buoys coordinated with the International Arctic Buoy Program, to ocean synoptic and mesoscale scale in the DN measured with more than 100 ice-deployed GPS position sensors, to ship-mounted ice radar (Oikkonen et al., 2017) providing dense target tracking over 7 km around the ship every few minutes, to high frequency and centimeter-level position accuracy from GNSS helicopters inertial navigation system stations and robotic theodolite strain observations. Ice motion was also monitored at two locations with seismic stations, providing information on vertical motion, and ice-wave interaction (Marsan et al., 2011). Three seismic stations, located at three points of the ice floe, recorded ice oscillations in three directions (horizontal and vertical) and transmitted the records to the central station installed on the ship. The signal recording frequency was 100 Hz. The graphical format of the waveform records allows to see ice events such as new fractures, compression or ridging. Internal ice stress was recorded with vibrating wire strain gauges (Cox and Johnson, 1983) at 17 sites in the CO. Twelve of these gauges had 1-minute sampling, the others 10-minute sampling, allowing for specific breaking events to be aligned with the stress time series. To estimate the ice stress on the *Polarstern*, stress panels were placed in the ice about 20 m from the ship parallel to 'Void 92', a specific compartment in the hull of *Polarstern*, which was instrumented with strain gauges. Throughout the drift the mechanical properties of the ice (local strength, horizontal and vertical uniaxial strength tests) were measured at a level SYI site. For these measurements, an LGK hydro-complex with a probe-indenter and a press was used. The probe-indenter was used to measure the local strength of the ice cover at different levels, and the press was used to measure the ice strength for uniaxial compression (horizontal and vertical). Salinity, temperature, density and texture analysis of co-located ice cores allow characterization of the mechanical properties of ice (Section 2.3). A log of specific dynamic events (cracks, leads opening, ridging) was kept, Panomax camera and Ice Radar were used to identify the start time of each event to within 20-minute precision. The full data set allows for specific case studies that can correlate ice fractures and the response of ice to ocean and wind forcing on scales beyond tens of meters.

2.9 Ridge observations

Ridges are one of the least studied features in the Arctic ice pack, because of logistical challenges in making measurements in these sometimes-massive chaotic formations of ice that pile up when ice floes collide. The main aim of the ridge work was to study the development of the geometry and of the thermo-mechanical properties of ridges during the MOSAiC drift. The three main phases of ridge evolution, initial formation, winter consolidation and summer decay, were documented for the first time for selected ridges throughout a full seasonal cycle and compared to the evolution of level FYI and SYI. The main geometrical parameters characterizing the ridges were the thickness of the consolidated layer, the keel depth and the macro-porosity. These three parameters were determined by repeated manual drilling (Figure 3) and complemented by continuous temperature profiles obtained by IMBs

and thermistorstrings that were deployed vertically through specific ridges. Additionally, sea ice cores were taken from ridges to characterize the temporal and spatial evolution of sea ice temperature, salinity and density. In addition to this baseline work, additional specialized measurements were performed to determine bottom topography, ocean properties, currents and keel-associated turbulence, as well as surface characteristics by snow and ice thickness transects, snow surveys and laser scans of surface topography (Sections 2.2, 2.3, 2.5, 2.10 and 2.11). The characterization of the physical properties of ridges was of particular importance to coordinated ecological studies of sea ice ridges performed by the ECO team.

570 2.10 Transect measurements

Making systematic and representative observations of physical sea ice parameters, their spatial variability and temporal evolution in the CO throughout the full MOSAiC drift was the objective of the transect task. The sampling strategy consisted of repeat surveys of sea ice and snow thicknesses throughout all MOSAiC legs, similar to observations carried out from May 575 to December during the Tara expedition in 2007 (Haas et al., 2011). These baseline observations were complemented with seasonal activities, specifically measurements of surface albedo and melt pond properties during summer and autumn. In addition, cross-task 580 activities with joint measurements by mobile on-ice remote-sensing sensors (Section 2.13; L-band microwave radiometer and Ku/Ka-band radar) along the transect lines or transect observations at specific ridges (Section 2.9) were carried out to provide input data for algorithm development and temporal and spatial evolution at ridges.

The transect measurements were carried out by repeating dedicated loops typically 1 km or longer, except for Leg 5 which was shorter. The baseline observations included a broadband 585 electromagnetic induction sensor (Geophex GEM-2, Hunkeler et al., 2016) for the measurement of the total thickness of the sea ice and snow/SSL layers and an automated snow/SSL depth probe (Snow Hydro MagnaProbe; Sturm and Holmgren, 1999) which in combination yield point measurements of snow/SSL and sea ice thicknesses. To accommodate measurements of snow/SSL and melt pond depths when both were present, the snow disc of the MagnaProbe was outfitted with floatation on its upper side to also measure pond depth.

590 During winter, only limited FYI and mixed type transects were performed, as no observations on FYI were possible in early winter. These transects were not revisited on later legs as they became inaccessible due to deformation. During summer and autumn, additional transects were conducted parallel to albedo lines for relating the properties of snow, SSL, sea ice, and melt ponds to the spectral and broadband albedo measurements (Sections 2.6 and 2.7).

595 The two goals for the transect surveys were to achieve representative coverage of sea ice conditions in the CO and continuity of observations throughout the drift. However, due to the relocation of *Polarstern* after Legs 3 and 4 (Table 1), new transect loops were established in addition to the original transect loops. In the beginning of the MOSAiC expedition, the two 600 original loops were laid out, termed “northern” and “southern” loop. The rationale behind the two loops was to survey the two dominant ice types in the CO: the northern loop on the older, thicker, and more deformed part of the “MOSAiC floe”; and the southern loop on the younger and thinner part that had widespread refrozen melt ponds. While these two loops were traversed continuously from October 2019 to early May 2020, the southern loop was often 605 inaccessible after sea ice deformation events. The summer transect (CO2) was established in June 2020 on similar ice conditions as the prior transect loops and with small (approximately 300 m) overlap with the northern transect loop. The transect loop of Leg 5 (CO3) was fully independent of earlier transects due to the change in regional focus. A full overview of the dates, location, and acquisitions of all transect observations is referenced in the data

availability section. In addition, the dates of all total ice plus snow thickness observations
610 including data acquisitions outside the transect task are illustrated in Figure 3.

2.11 Remotely operated vehicle (ROV) observations

The main goal of the work with the ROV was to obtain a better understanding of the seasonal
615 cycle with respect to (1) ice draft and bottom topography, (2) the light field beneath the ice,
(3) the bio-physical properties of the ice and uppermost ocean, and (4) the organisms living in
and under the sea ice. All measurements focused on the spatial variability under sea ice and
620 across different surface features and ice types. To accomplish these objectives, the ROV was
operated one to three times per week amounting to a total of 83 dives. The ROV was equipped
with a comprehensive suite of bio-physical sensors, several cameras, and a mechanism to haul
sampling nets under the ice (Katlein et al., 2017; Wollenburg et al., 2020). During summer,
625 additional dives were performed with an underwater hyperspectral imager (UHI) to survey
the 2D and 3D radiance under sea ice. In addition to the direct data sets from the ROV, the
work was complemented by data sets from other ICE and ECO team tasks to allow the up-
scaling of point observations, observing links to ecosystem parameters, and estimating energy
630 budgets combined with other observations.

The ROV was operated within an approximate 300 m radius around the ROV sites (Figures 2
and S3). Over the year, the ROV site was moved several times due to the dynamic icescape.
Specific dive missions were defined and executed as part of the weekly schedule. Over most
630 of the year, weekly multi-beam sonar surveys and net hauls were carried out. Multi-beam
sonar surveys mapped the under-ice topography in a grid covering an area as large as possible
at a depth of about 20 m (Section 4.1). Net hauls were conducted along linear or triangular
transects at different depths for dive times of approximately 15 minutes. Once sufficient
635 sunlight returned (mid-March), comprehensive optical dives were carried out on the ROV days
(including downwelling radiation), in particular for grids and transects under FYI, SYI, leads
and ridges. This effort also included stable measurements at marker positions, vertical profiles
and measurements of upwelling radiation. Additionally, specific dive missions were added to
locate lost devices, to document under-ice installations and to deploy and recover sediment
traps.

640

2.12 Helicopter observations

The main objectives of the helicopter-borne sea ice surveys were, first, to document the
645 temporal evolution of snow and sea ice cover on the CO floe and within the DN, from sea ice
formation in autumn to sea ice melt in summer and, second, to document the spatial
distribution and spatial variability of snow and sea ice properties within the DN and beyond.
Key parameters were sea ice thickness distribution, surface topography, freeboard and floe
size distribution, surface temperature and surface albedo, areal fraction of different sea ice
650 types, and melt ponds as well as additional melt pond characteristics like pond-size
distribution and bathymetry (Section 2.7).

650 To reach these goals, three different sensor packages were operated independently on
different flights: (1) an airborne laser scanner (ALS, Riegl VQ-580), two RGB cameras (Canon
EOS 1D Mark III) with wide-angle and fisheye lens, in winter an IR camera (VarioCAM HD head
680, InfraTec) or in summer a VIS/NIR hyperspectral camera (Specim AisaEAGLE, 400 nm to
970 nm), a radiation thermometer (Heitronics KT19) and an upward and downward looking
655 pyranometer (Kipp&Zonen CMP22), (2) EM-Bird for measuring the combined thickness
distribution of sea ice and snow using airborne electromagnetic induction sounding (Haas et

al., 2009), and (3) the towed system HELiPOD, which was operated by the BGC team for measurements of trace gases, energy and momentum fluxes, aerosol and sea ice surface properties. The laser scanner and camera configuration was operated during all legs on a total of 68 flights, the EM-Bird was operated during all legs, except in the midwinter darkness, on 660 23 flights, and the HELiPOD was operated in spring and summer on five flights.

There were five main mission types to investigate the temporal evolution and spatial variability of snow and sea ice properties: (1) local floe grid survey covering the CO floe and surrounding floes, (2) regional survey consisting of lines between the three L-site buoys and 665 between these buoys and Polarstern, (3) butterfly survey consisting of triangles between Polarstern and four selected buoys of the DN to observe the relation between ice deformation and thickness change, and (4) mixed pattern of horizontal lines and vertical profiles mostly across the CO. Missions (1) and (4) were flown with the ALS and camera sensor package as well as with the EM-Bird and HELiPOD, mission (2) with the ALS and camera sensor package 670 only, and mission (3) with the EM-Bird only. The maximum airtime of individual flights was about 2 hours.

2.13 On-ice remote sensing

Almost all Arctic-wide sea ice climate time series are based on microwave satellite 675 observations (IPCC, 2013), which now span more than 40 years. However, the retrieved geophysical parameters like ice concentration, ice type, ice thickness, melt onset, or snow depth are not measured directly by the microwave radiometers and radars but inferred from the interaction of microwave radiation with sea ice and snow as well as seawater. Depending on frequency and physical properties (temperature, salinity, snow grain size and geometry, 680 porosity, etc.) of the snow and sea ice (including melt ponds), microwave radiation can penetrate into the ice, get scattered, absorbed and emitted. Information of the microwave radiative transfer in snow and sea ice is needed to derive the observational quantities from satellite measurements.

The main objective of the ice remote sensing (RS) task is to develop new methods to retrieve 685 improved sea ice and snow parameters from satellites. This goal relates both to reducing and quantifying the uncertainties of existing satellite retrievals (e.g., ice concentration, sea ice thickness and ice type) and to developing new methods for current and future satellite missions (e.g., snow depth for CRISTAL and CIMR, surface properties and ice types from 690 Radarsat Constellation Mission and TerraSAR-X, melt pond depth using hyperspectral airborne data and Sentinel-2). Most measurements described here were in the microwave domain from 0.5 to 89 GHz using passive microwave radiometers and active radars. Here, the most pressing issue is to better understand how the microwave emissivity and backscatter depend on physical snow and ice properties and environmental conditions. Thus, remote sensing 695 instruments were co-deployed with snow and ice measurements (Figures 2 and S4). In turn, radiative transfer modelling of snow and ice will be improved with the availability of the RS measurements. Further observations were carried out in the visual and IR domain to support the microwave measurements and to measure ice, snow and melt pond optical properties as well as surface temperature distribution and evolution. MOSAiC offered the unique 700 opportunity to observe a full seasonal cycle and co-locate measurements at different frequencies and polarizations. RS measurements were taken at a central remote sensing site on the ice floe during all five legs, from the ship, and along transects (Section 2.10). An overview of the remote sensing site is given in Figure S4. A detailed overview of satellite related work is under development led by G. Spreen. Sea ice conditions along the drift

705 trajectory based on satellite observations and comparison to previous years are described in Krumpen et al. (2021).

710 Table 2 provides a short overview of the 14 RS instruments that were operated during MOSAiC, with their basic instrument parameters. In addition, examples of corresponding satellites or sensors are given. The three main instrument categories were microwave radiometers, radars, and other sensors like GNSS-R, IR, and cameras. These remote sensing measurements on the ice correspond to a wide range of satellite sensors, which are also listed in the table. Due to ice dynamics and instrument problems not all instruments were operational all the time (see Figure 3b for observation periods). The primary measured 715 parameters are emitted infrared and microwave radiation (brightness temperature from radiometers), backscattered (radars) and reflected (GNSS-R, nadir Ku/Ka radar) microwave radiation, and spectral reflectances (hyperspectral camera).

Include Table 2 here

720

3 Synergy in the observational program and available data sets

The work on snow and sea ice processes and properties required an integrated approach to carry out the observational program along the tasks outlined in Section 2. Performing consistent measurements throughout a full year was a major challenge and one of the main 725 differences between MOSAiC and many previous snow and sea ice field studies. To guarantee consistent high-quality data collection between all legs, a particular preparation phase was performed (Text S1). This section describes the key processes, which were studied by the ICE team across the different tasks (Section 2). These processes are illustrated in Figure 4. While most processes were observed continuously over the full annual cycle, seasonal processes 730 were only studied during parts of the drift (e.g., solar short-wave radiation interactions). The work covered multiple ice types and the highly variable snow distribution: new ice, FYI, and SYI. We worked on level, deformed and ridged sea ice as well as in the marginal ice zone, leads and melt ponds. In addition, we describe the measured parameters and the resulting data 735 sets, which will be used to improve and develop parameterizations for a better understanding of the coupled Arctic sea ice system. The key parameters are summarized in Table 3 and their temporal coverage is shown in Figure 3. Methods and tasks are restricted to the work in the COs.

Figure 4: Schematics of the snow and sea ice processes studied during MOSAiC.

740
Include Table 3 here

Sea ice and snow mass balance

New ice formation in open water (mainly in leads) was observed through the entire autumn, 745 winter and spring, including observations of surface, bottom, lateral and internal freezing. In October 2019, most measurements were performed on SYI that had survived the previous summer. However, parts of the ice camp, e.g., the coring activities, were also established on younger sea ice that involved FYI. Thus, the evolution of both FYI and SYI during the initial freezing was observed and followed throughout the campaign. Furthermore, MOSAiC was 750 able to observe the initial accumulation of snow in autumn. Snow accumulation, distribution and re-distribution were observed through the entire year with a particular focus on comparisons of snow processes between level FYI, level SYI, and deformed (ridged) ice in the CO, and how these processes affect the growth of different ice types.

755 The novel observation of platelet ice under winter sea ice in the Arctic showed that platelet ice contributed to bottom ice growth during winter (Katlein et al., 2020). Over time, the ice pack became strongly deformed. After melt onset, the melt and decay of the snow and sea ice were observed, and contribution from surface, bottom, lateral and internal melt processes 760 were quantified. The decay of the original MOSAiC floe (CO1 and CO2) on July 31, 2020, showed strong linkages between dynamic and thermodynamic processes controlling the decay of the ice pack in the marginal ice zone.

In addition to the general time series of each ice type, the comparison of sea ice and snow 765 mass balance for level and deformed ice was an important element along the transects. The thickness, consolidation and decay of pressure ridges were examined by a combination of drilling, coring and analysis of IMB and thermistor string data. The macro-porosity of ridges was estimated from drillings while the keel depth was investigated by drilling, ROV multi-beam

mapping and IMB/thermistor data. Almost all tasks contributed in some way to the sea ice and snow mass balance work (Table 3).

770

Ice and snow physical properties

The physical properties of sea ice were studied based on ice cores and samples on the micro-scale, but also through surface and under-ice transects as well as larger scale airborne and dynamical studies (Table 3). The ice coring work of the ICE team focused on the time series of the main coring sites to capture the evolution of FYI, SYI and deformed ice. Additional information on the spatial variability is available through the work related to the mechanical properties, the remote sensing work and in particular through the BGC team, which surveyed additional sites across the COs and DN1. Optical properties were mostly studied in relation to energy budget studies (see below).

780

Snow on sea ice is the thermal and structural interface between sea ice and the atmosphere (Sturm and Massom, 2017). Thus, even though major parts of the snow work were performed by the ICE team, many linkages exist to the ATMOS team, and comprehensive parts of the snow work were carried out in strong collaboration with the ATMOS team. Snow precipitation, rain fall, and snow re-distribution were studied with common set-ups by both teams. Snow formation, snow metamorphism and changes in the snowpack were studied in detail from micrometer scales to floe scales. Snow cover is the most (temporally and spatially) variable layer dominating the thermal and optical properties of the sea ice system. Due to the highly metamorphic nature of snow, its microstructure changed at a fast pace. Snow processes during MOSAiC were highly sensitive to quickly changing air temperatures, which led to strong temperature gradients in the snow, particularly during Legs 3 (spring) and 5 (autumn), and resulted in a high degree of snow metamorphism. The strong temperature gradients affected the thermodynamics, growth rate and microstructure of the underlying sea ice, and consequently strongly affected the temperature, salinity and permeability of sea ice. Ultimately, the physical snow properties and processes build the link to light and nutrient availability in the sea ice and in the upper ocean, and significantly affect the polar marine ecosystem.

Energy budget, optical properties, and melt ponds

800

Incident solar shortwave radiation is partitioned into reflected, absorbed, and transmitted components during the sunlit season. This split determines the surface shortwave radiative budget, with effects on mass balance and physical properties of snow and sea ice, and contributes to ocean heat (Figure 4). The optical properties of the ice cover were investigated by a variety of methods. This variety was needed to constrain radiation budgets, provide some spatial and temporal overlap, achieve redundancy to help alleviate data gaps where instruments failed, and to provide insight into physics that are driven by or drive processes not well constrained by a single set of measurements. An example would be the utility of surveying both albedo and transmittance simultaneously to understand the full partitioning. While the work of the ICE team focused on studies of this partitioning within the snow and ice, the ATMOS team observed radiative transfer in the atmosphere as well as the full surface energy budget including radiative, turbulent, and conductive heat fluxes. The OCEAN team observed radiative heating and turbulent mixing in the ocean, using a combination of near-ice direct heat, salt and momentum ocean flux measurements and profiling CTD and microstructure dissipation profiles.

815

Conductive heat flux between atmosphere and ocean through the snow and sea ice pack was studied mostly based on thermistor chains (Section 2.4), but also as residuals from surface and basal mass balance calculations. These heat fluxes are crucial for quantifying melt and freeze processes at both interfaces and thus are key elements to close the atmospheric and oceanographic energy budgets. Heat fluxes through snow and sea ice strongly determine sea ice mass balance.

820 Fixed stations measured the temporal variability at single locations. Surveys measured both spatial and temporal variability. Fixed installations included automated radiation stations, the UHI, light chains hanging through the ice into the ocean below the ice, and a light harp, which is a novel in-ice light profile sensor that was co-located with a salt harp system. Optical property survey work included measurements of surface and drone-based albedo and through-ice light transmittance recorded on the ROV. Other measurements that did not use a repeat-survey sampling strategy, but also were not tied to a fixed field of view on the ice, 825 included helicopter and HELiPOD albedo, in-ice inherent optical property probe, and ice cores taken for dedicated laboratory assessment of inherent optical property profiles (Table 3).

830 The surfaces of snow and sea ice, which comprise the dominant properties for remote sensing and large-scale linkages, changed seasonally. While our work during winter was strongly related to changes in snow accumulation, ridging, and surface roughness, surface melt processes were examined in detail over summer. Starting with melt onset, the melt dynamics of the snowpack and the formation and evolution of melt ponds were studied. In addition, the physical properties of melt ponds were investigated, mostly in connection to ecological and biogeochemical properties. Surface properties and melt ponds were linked to process studies 835 on radiative and heat transfer, due to their large impact on the surface energy budget.

840 During summer and autumn, the flux of snow and ice meltwater into the ocean played a key role with immediate links to the ocean properties, the ecosystem and biogeochemical fluxes. The formation and evolution of the meltwater layer in leads and under the sea ice was studied in detail in a joint effort across the teams (Section 4.2).

845

Dynamics, mechanics, and ridges

Studies of sea ice dynamics and mechanics were carried out during all legs in the CO. They give insights into the connections of sea ice material properties at the millimeter scale to the visco-plastic behavior of sea ice at the floe scale. Sea ice deformation at the floe scale was 850 measured down to millimeters in the CO using the laser strain instrument. Ridge and lead formation were observed through the many dynamical events in the CO by e.g., airborne mapping by ALS, the EM-Bird, and aerial imagery. Over 120 position buoys in the DN contributed to a regional-scale data set of sea ice drift and displacement. The ice radar system onboard of *Polarstern* also mapped the dynamics within 5 nm around the vessel (Jäkel et al., 855 2021).

Ridges and leads had strong logistical implications for the work and fate in/of the ice camp. After ridge formation, the temporal development of the consolidated layer, the macro-porosity and the keel depth were studied in a number of ridges using the described mass 860 balance, ice coring, TLS, transect and ROV methods (Sections 2.3, 2.4, 2.5, 2.10, and 2.11). In-situ stresses were measured on the ice floe and will be correlated to atmospheric and oceanic forcing as well as the kinematics of ice drift at different scales.

865 The mechanical properties of the ice were studied through in-situ borehole jack testing with two different jacks and through sampling ice cores and testing uni-axial strength in the field. The full annual cycle of data gives a unique data set that can be correlated with small-scale physical properties (temperature, density, salinity) and ice texture allowing for a quantification of small-scale (0.01 m) ice mechanical properties and their seasonal variability.

870 **Microwave interaction with snow and sea ice**

875 Measurements in the microwave domain (radiometers, radars, reflected GNSS signals) at different frequencies and polarizations were conducted simultaneously with the extensive physical ice and snow measurement program during the whole MOSAiC drift. The combination of all measured frequencies and polarizations allows a better understanding of the processes, as well as the volume fraction of emitting and scattering constituents and their geometry, which define the seasonal development of microwave signals. Key processes influencing the microwave radiation are, e.g., snow metamorphism and ice lenses/layers in the snow, snow liquid water content, wicking of brine into snow and desalination of ice during summer, changes of ice thickness and the snow/ice temperature profiles (Ulaby and Long, 2014). These processes can cause major changes and fluctuations in the microwave signals and can add significant uncertainties in satellite sea ice retrieval algorithms. To develop new satellite retrievals and quantify uncertainties of existing retrievals, first, the processes that influence the microwave retrievals have to be understood better. Second, based on the improved process understanding, better microwave emission and scattering models (Tonboe, 2010; 880 Picard et al., 2018) can be developed. They require a number of poorly constrained input parameters (e.g., correlation length scales or salinity profiles) for which the MOSAiC snow/sea ice physics measurements in combination with the microwave measurements are essential. The same microwave radiative transfer models (sometimes called forward operators) are also needed to assimilate microwave satellite observations in climate and weather prediction 885 models.

890 The full seasonal cycle was captured by the multi-frequency remote sensing observations. Largest uncertainties in satellite retrievals occur when environmental conditions change, like during melt-refreeze cycles, warm air intrusions, or rain on snow events, which all were observed during MOSAiC and are of special importance.

895

4 First results, case studies and remaining challenges

900 This section presents first results from the MOSAiC drift. These results consist of methodological advances, which make use of technological developments (Section 4.1) as well as scientific results that contrast winter and summer snow and sea ice properties and conditions (Section 4.2). The last part (Section 4.3) discusses remaining challenges of the snow and sea ice observational program.

905 Figure 5 is called the “sea ice clock” and illustrates the sea ice and surface conditions in the three COs based on photographs taken by the panorama camera (Section 2.1). Each image represents the conditions of one month during the annual cycle: starting from thin and new ice in September/October, further ice growth with snow accumulation through the dark season until February, into the dense and cold spring ice pack until April, and then snow melt and melt pond formation, and the decay of the ice pack in summer. At the beginning of the 910 drift, CO1 consisted of SYI with a highly compressed core of the floe and refrozen melt ponds over large parts of the floe. Over time new ice formed and the icescape became strongly deformed (see below).

915 Figure 5: The ‘sea ice clock’.

4.1 Applying methodological and technological advances

920 Methodological and technological advances were implemented for the MOSAiC drift in all tasks, allowing a sharp improvement in observing sea ice and its snow cover for an entire year. The measurements benefited from development of sensor and instrument technology over 925 the last decades, advances in data handling and processing, and improved coordination across tasks and disciplines. Technological advances resulted in data sets with higher spatial and temporal resolution as well as with reduced uncertainties. It was possible to obtain long time series with instrumentation that was earlier only used for case studies or dedicated measurements. Covering most of the year, these advanced technologies often turned into a backbone of the MOSAiC data set. The technological (including data processing) advances 930 enabled the immediate use of measurements to plan additional measurements and aid decision making. Selected examples are:

935 (1) Combining an eye-safe TLS during winter and a non-eye-safe TLS during summer allowed the same regions to be scanned in the CO approximately every 2 weeks (Section 2.5). A custom heated enclosure enabled scans throughout the winter in temperatures below -30°C . During summer, the Riegl VZ6000 allowed for challenging measurements of wet surfaces. A first version of data was processed on board for immediate analysis in support of other measurements (e.g., precisely locating the ROV transponders). Figure 6 shows the results of 940 two TLS scans of the same piece of ice, containing level ice and a small SYI ridge, on January 19 and 25, 2020. In this way, the TLS data are used to quantify surface changes related to snow fall and re-distribution, as shown in this example. Figure 6d illustrates that the snow deposition is concentrated in a snowdrift off the ridge (left of the peak). Similar results on snow accumulation in ridged areas are expected from the transect data across the COs, while the TLS data provide two-dimensional accumulation details on the centimeter scale.

945 Figure 6: Snow redistribution observed via terrestrial laser scanning (TLS).

945 (2) The micro-CT system (Section 2.2) operation in a freezer-lab container allowed for almost in-situ imaging of samples, without the delays and likely changes in microstructure. Immediate scanning was of particular value for snow samples and the more delicate samples of the bottom of sea ice cores, because it ensured that the samples were as close to their original state as possible. Sea ice samples from ice cores were transported in insulated customized boxes that kept, through eutectic phase change cooling elements, temperatures close to the 950 in-situ seawater freezing temperature of approximately -2°C. On the ship the samples were centrifuged at this temperature (Weissenberger et al., 1992). This procedure ensured the conservation of in-situ microstructure as well as sufficient contrast to retrieve pore network details by a subsequent micro-CT imaging (Section 4.3). The immediate onboard visualization of the 3D structure of snow and ice gave insights into relevant processes and allowed for 955 targeted additional sampling, specifically with respect to the less studied snow-ice interface processes.

960 (3) The snow pit program was carried out by instrument-based measurements, which resulted in a consistent time series with minimal human bias. Main advances resulted from 965 standardizing the snow characterization using micro-CT, SMP, NIR and structure from motion photography (Section 2.2). These novel quantitative measurement techniques were combined with the concept of defining different types of snow pits (e.g., relatively quick snow pits with fewer measurements versus more elaborate snow pits using the complete suite of measurements; Section 2.2), and thereby ensuring that a standard set of measurements was performed for each snow pit type during all legs.

970 (4) Studies of dynamical and mechanical properties benefitted from the advance in autonomous platforms. In the CO, the laser strain array was operated to investigate sea ice deformation and mechanics on the millimeter scale. These data will give new insights into 975 mechanical properties, in particular in combination with the measurements of stress and strain rates and high precision position monitoring (Section 2.8).

980 (5) Optimizing and winterizing the ROV (Figure S3) and surface unit allowed us to operate the vehicle in all conditions and without interruptions related to sensors or technology during the 985 full annual cycle. Advances in sensor technology allowed for more precise under-ice navigation and synchronous recording of all data streams. Specialized additional sensors, e.g., the UHI or suction sampling systems, were integrated into the vehicle in the field. In addition, the reliable operation of the ROV allowed site selection and instrument maintenance under the sea ice. Particularly the sensitive manipulation skills of the ROV system allowed the deployment and recovery of sediment traps, inspection and maintenance of under-ice 990 sensors, as well as sampling without the need for human divers. Figure 7 shows the light transmittance distribution under sea ice in July 2020. Compiling 6 dive days with focus on optical measurements makes it possible to quantify the increasing amount of radiation penetrating the sea ice as melt progresses, allowing for detailed analysis of the increasing spatial variability and the evolution of individual patches with high or low transmittance. The overall evolution shows that the initially uni-modal distribution with a modal transmittance of 0.03 develops into a bi-modal distribution with modes at 0.15 and 0.26. This shift in modes represents the evolution from wide-spread wet and melting snow and surface scattering layer to a white ice and melt pond pattern. For illustration, see the surface images of June to August in Figure 5.

Figure 7: Light transmittance through sea ice measured with the ROV.

(6) The MOSAiC ICE field program strongly benefitted from advances in drone technology.

995 Operation of (small) drones for systematic aerial photography and optical measurements (see below) advanced the study of surface processes. Advances in and miniaturization of both drone and sensors systems allowed for successful operation of these platforms at high latitudes, and accurate measurements of broadband and spectral irradiance. The latter was achieved in part through the stabilization of sensors using miniaturized gimbal systems that could be readily carried by the drones. Additionally, continued advancement of battery systems allowed for extended flight times for these platforms, increasing capabilities with respect to sampling area and achievable altitude. The drones supported the alignment of various measurements at the surface, e.g., the optical measurements along the albedo lines (see Figure 9), as well as mapping of the surface at high spatial resolution to provide enhanced information over limited spatial coverage within the CO (Section 4.3).

(7) Data from the ALS and the real-time navigation solution of the inertial navigation system of selected flights covering the CO were processed with a short delay of 1 or 2 days after the surveys. The processing steps included the estimation of ellipsoidal elevations of the ALS range

1000 measurements, the transformation of the geographical coordinates into a local cartesian coordinate system using position and true heading data from *Polarstern* as well as the merging of all ALS swaths into a single digital elevations model with a spatial resolution of 0.5 m. Visualizations of these models served as valuable science planning information in the absence of large-scale aerial photography during the winter season (Figures 2 and 8). More than 20

1005 ALS surveys provided floe maps throughout MOSAiC, with the largest survey consisting of three coordinated flights in late December 2019 and covering approximately 70 km².

(8) A newly developed sensor suite (Section 2.12) allowed to observe different important surface properties at the same time. The topography/roughness of the sea ice cover can be

1020 directly related to areal properties like ice thickness, melt pond coverage and surface albedo. With a lateral resolution of 0.5 m and an elevation uncertainty between 2.5 cm (center) and 10 cm (edges), the laser scanner data allow digital elevation models to be derived with a precision never reached before on airborne operations from *Polarstern*. The TIR camera has a precision of 0.2 K and an accuracy of 1 K and allows detailed mapping of thin ice thickness

1025 distributions and lead coverage. The digital single lens reflex and hyperspectral cameras operated during daylight time allow retrieval of albedo and detailed snow and melt pond optical properties. Sea ice thickness surveys (EM-bird) in close temporal vicinity to the camera/ALS flights resulted in synergistic measurements that allow a novel areal view of sea ice properties. The drones were also used for floe mapping to document and plan the work

1030 under daylight conditions, thus supplementing the ALS maps.

(9) The deployment of novel and advanced buoy systems in the CO and DN strengthened the acquired time series particularly during the time when *Polarstern* had to leave the MOSAiC

1035 floe. In addition to more classical IMBs and Snow Buoys, emerging technologies such as the continuous measurements of the vertical profile of sea ice salinity (so called salt harp), in-ice and water column light and characterization (optics probe) of under-ice biological activity by the means of fluorometry and autonomous acoustic profiling were key contributions of the ICE team to the interdisciplinary efforts in the DN.

1040 (10) Novel on-ice remote sensing instruments were developed for MOSAiC (Ku/Ka-radar, GNSS-R, HUTRAD and L-band microwave radiometers) to evaluate measurements of existing and upcoming satellite missions (Section 2.13). For the first time, a large set of 14 remote sensing instruments, covering both active and passive measurements as well as a wide range of frequencies and polarizations, was operated on the same sea ice floe. Several high-
1045 resolution optical and synthetic aperture radar (SAR) satellite sensors performed specific acquisitions for the MOSAiC region. In particular for SAR, a unique dataset from newly launched sensors (e.g., Radarsat Constellation Mission, SAOCOM) and wide range of frequencies (ALOS-2, TerraSAR-X, PAZ, COSMO-SkyMed, KOMPSAT-5) were acquired, which will allow novel multi-frequency and full polarimetric sea ice analysis at unprecedented
1050 temporal resolution. These acquisitions required placing an order of the satellite scenes about two days in advance on a daily basis. This process was facilitated by the availability of a dedicated near-real-time drift forecast product for the MOSAiC floe, to have *Polarstern* as central as possible in the satellite scenes. The product was provided by the Year of Polar Prediction (YOPP; Jung et al., 2016) Sea Ice Drift Forecast Experiment (SIDFEx). For MOSAiC a
1055 consensus ensemble forecast product, based on the different forecast systems, was used. The consensus forecasts were provided onboard *Polarstern* to support decision making. Figure S5 exemplifies the consensus forecasts product, showing the forecast issued on February 24, 2020, and revealing that, while the drift over the subsequent 4 months toward Fram Strait was on average considerably faster than anticipated, the trajectory remained within the
1060 ensemble uncertainty margins.

4.2 Advances through co-location and synchronization

1065 Coordinating measurements and sampling strategies within the ICE team (across tasks) and with other teams allowed the required systematic and representative observations of multiple components of the coupled system to be obtained. Here we present examples of such activities.

1070 Probably the most striking and obvious advantage of MOSAiC was the interdisciplinary coordination across the scientific teams. Although most field measurements benefitted from this advantage, the most prominent example is the coordination of sea ice coring across disciplines. Traditionally physical scientists are interested in the ice-snow or ice-atmosphere interface and reference their work from the ice surface (i.e., the zero-reference level is set at the ice surface). However, most (sea ice) ecological studies are primarily interested in the
1075 highly porous underside (i.e., bottom) of the ice, where the majority of the biomass is found (Manes and Gradinger, 2009). Thus, they tend to reference their work from the ice bottom upwards. This difference often makes direct comparisons of data collected with the two approaches difficult. During MOSAiC the sectioning of ice cores for physical and biological sampling was optimized such that sectioning was initiated both from the top and bottom, and
1080 the middlemost part of an ice core was left with the “odd” length section. Co-location of coring with the ECO and BGC teams captures the seasonal evolution of both physical and biological properties for FYI and SYI. Approximately 1500 ice cores were collected during approximately 30 visits at FYI sites and 25 visits at SYI sites. This coordination effort will allow better direct comparison of ice core data across teams.

1085 Snow sampling was coordinated with other teams, usually collected by the team making snow pit measurements, independently of the purpose and later analysis of the snow samples. This

strategy ensured that samples from each sampling event were taken at the same site(s) and same time and in a consistent and reproducible manner throughout the campaign. Special 1090 emphasis was given to sampling co-located with other measurements, e.g. at the remote sensing site. For interpretation of the remote sensing measurements the snow and ice physics measurements are critically needed.

The observations of low-salinity meltwater layers under the sea ice and in leads during 1095 summer resulted in a dedicated interdisciplinary program across all teams. Drill lines spanning in total 900 m were completed covering different ice types with the specific aim to measure the ice thickness and ocean temperature and salinity profiles directly beneath the ice and to map the presence of 'false bottoms' formed at the meltwater-seawater interface. These 130 ice thickness observations, of which 30 have associated ocean temperature and salinity 1100 profiles, overlapped with existing long-term mass balance observations (stakes and thickness surveys). Additional melt pond, ice core and under-ice and lead water samples were collected by the ICE, ECO and BGC teams to better understand the meltwater sources, and the role of these meltwater layers in physical, chemical and biological processes in summer.

1105 MOSAiC offered the opportunity to co-locate measurements of sea ice surface and bottom topography, the internal structure of pressure ridges and the biology associated with ridges. This approach allows a complete 3-dimensional view of ridges. Figure 8 shows the surface and bottom topography as well as a visual photograph of the pressure ridge called 'Jaridge'. This ridge was located between the SYI closer to *Polarstern* and the FYI where the ROV and the FYI 1110 coring site were located (Figure S3). Jaridge was formed during deformation events primarily during winter (Leg 2) and included parts of the floe adjacent to the former dark site coring site. The Jaridge ridge consisted mostly of 20–40 cm thick ice blocks. This site was used for a large suite of coordinated measurements and installations: an IMB was deployed, several 1115 transects with drilling for ice thickness and consolidated layer thickness were undertaken, sea ice cores were collected (ICE and ECO), sediment traps were deployed with the ROV, ROV multibeam and the UHI was used to map ridged and level ice, biological samples were taken in the ridge, and airborne mapping was conducted with ALS and cameras. This will provide a comprehensive and unique view on the evolution of sea ice ridges in the Arctic summer.

1120 Figure 8: The Jaridge ridge and adjacent lead in summer 2020.

The evolution of the sea ice surface during the summer is a culmination of changes in the 1125 radiative energy and mass budget due to variation in snow cover, melt ponds and bare ice. Capturing the heterogeneity in surface conditions, in both space and time, is key to understanding the seasonal evolution of surface albedo and thus surface energy balance. Surface measurements of snow and melt pond properties, and albedo (both spectral and broadband), were coordinated with aerial measurements of both surface topography and 1130 albedo. These observations also overlapped with TLS scans (Section 2.5). Micro-CT observations of the ice and snow provide novel insights into the evolution of the surface microstructure in relation to the observed radiation budget. In addition to the surface-based 1135 observations of ice and snow, surface albedo measurements and imagery of the surface were collected using drones. These activities included flights over the surface albedo lines to compare observations from surface pyranometers and spectral radiometers with those on the drones. To align measured albedos along the measurement survey line, drone GPS coordinates were corrected to account for ice drift, and the albedo was averaged every 2 m

from 4 individual flight passes along the line. Mean drone-based albedo values and standard deviation measured along the “lemon drop” albedo line on July 06 are shown in Figure 9 (red line). The drone operating along this albedo line carried a modified Kipp and Zonen PR1-V broadband pyranometer, measuring wavelengths between 310 and 2700 nm. Surface and

1140 drone-based measurements show good agreement, with differences primarily resulting from the difference in sampling altitude (1 m for surface-based measurements and 15 m for drone-based observations), with the higher sensor aggregating the influence of surface type variability. This influence of sensor altitude on observed surface albedo is being investigated in a separate study.

1145 Figure 9: Surface albedo during summer.

Figure 10 shows winter and summer time-series measurements of several co-located remote sensing instruments (Table 2 and Figure S4). During a storm event in November 2019

1150 measurements by both radars and radiometers show changes in backscatter and brightness temperature, respectively. Due to the fact that air and surface temperatures reach a maximum of -5°C , melting plays no role in these changes, but snow metamorphism already can happen. Also, strong winds of up to 20 m s^{-1} caused snow compaction and redistribution.

1155 The radars and radiometers show stronger changes for higher frequencies and partly opposite behavior depending on frequency. The 35 GHz radar backscatter decreases by close to 2 dB

1160 while at 15 GHz it increases by about 1 dB during the event. At the lowest frequency of 1.3 GHz no changed radar response is observed during the event, which is in correspondence with the minimal changes in GNSS-R reflectivity operating at a similar frequency. During the storm event the increase in magnitude of microwave brightness temperatures (TB) is increasing with frequency: e.g., at 89 GHz TB is increasing by about 50 K, which corresponds to a strong emissivity change, while at 1.4 GHz almost no TB increase is observed. The peak of the storm on November 16, 2019, could not be captured by most of the remote sensing instruments because a crack opening, due to strong ice dynamics, at the site caused a power outage.

1165 In summer, on September 13, 2020, even stronger fluctuations in both backscatter and brightness temperatures occurred when the air temperature became positive and melting increased.

1170 Rain on snow additionally changed surface properties. GNSS-R reflectivity, both at the remote sensing site and on *Polarstern*, increased during the event. On September 15, after the temperature dropped below zero again, measurements also stabilized. Similar to the winter event, the changes in magnitude and variability increased for higher frequencies both for the radars as well as the radiometers, with the exception of the 1.4 GHz radiometer. However, changes were much stronger in summer compared to winter (note the different y-scales in Figure 10).

1175 Ice thickness influences the signal at very low microwave frequencies. Measurements by the 1.4 GHz L-band show lower brightness temperatures at a partly refrozen lead (light blue line)

1180 than for the thicker ice at the remote sensing site (dark blue line; Figure 10). This effect is used to retrieve thin ice thickness from L-band satellite measurements from SMOS and SMAP (Kaleschke et al., 2016; Pailea et al., 2019) and in future CIMR. The higher measurement variability at the lead likely is due to the changing ice conditions caused by ice dynamics.

Variability in brightness temperature and backscatter induced by environmental changes like those shown in these two case studies are not accounted for in current satellite sea ice retrievals for ice concentration, thickness, or snow depth and are causing uncertainties in the satellite data sets. In conclusion, during both events lower frequencies were less affected by the environmental changes and thus should result in more stable satellite retrievals. By

1185 combining the on-ice remote sensing measurements with the detailed snow and ice physics measurements, we can better understand and model the interactions of microwaves with snow and ice. Future work will improve satellite remote sensing methods to obtain better sea ice satellite climate records.

1190 Figure 10: Remote sensing signatures during winter and summer.

1195 4.3 Case studies in winter and summer

To demonstrate the comprehensiveness of the snow and sea ice measurements during MOSAiC, two weeks of measurements are selected as case studies. The week starting January 20, 2020, (Leg 2) represents the work during winter darkness in the polar night and the week starting on July 06, 2020, (Leg 4) represents the work during summer. Figure S1 shows how the work from the different tasks was distributed over the respective week. Additional optical measurements were carried out under daylight conditions.

1200 Sea ice, snow and weather conditions differed significantly for both case study weeks. As expected for high Arctic conditions, the mean air temperature was -29.0°C during the week in January and 0.3°C during the week in July. Wind speed at Met City (Figure 2) was 4.6 m s^{-1} and 6.4 m s^{-1} for the weeks, respectively. In general, the winter period was characterized by a transition from weak winds with periodic thin, ice-dominated clouds to a couple of passing snow storms later in the week with increased winds. The summer week was similar in some 1205 regards, but with much higher temperatures, characterized by persistent low-level, liquid-dominated cloud and fog, with two short storms that produced light drizzle near the surface. A detailed description of the meteorological conditions at the CO is in preparation led by M. Shupe.

1210 To contrast the different snow and sea ice conditions, Figure 11 illustrates various aspects of the surface and ice conditions. The figure shows the CO and its surrounding on composites from hundreds of aerial photographs taken from the *Polarstern* helicopters. During polar night, TIR photos were used to map the surface temperature, which indicates sea ice types based on differences in surface temperature. The map shows a dense ice pack with few 1215 deformation zones and elongated structures of thinner ice (higher temperatures) resulting from leads with new thin sea ice. During summer, visible photos were taken and give a view of the surface conditions. Towards the end of June and in July, the sea ice surface consisted of many distinct floes, widely covered with melt ponds. The observation over the year of the same ice pack and area will allow consideration of how much of the wintertime surface and 1220 structural features determine summer features, such as the melt pond distribution. In general, the observational concept of TIR and ALS flights during the dark season proved most useful (Figure 2). Both methods were used to map surface conditions and guide the on-ice measurement program as well as to support logistics through results on snow and sea ice surface properties, immediately processed on board *Polarstern*.

1225 Figure 11: Aerial photo mosaics of the central observatory and its surroundings.

The drift and deformation of the ice pack was one of the most remarkable features of the MOSAiC field experiment, and more extensive than expected. In total, the ice camps covered 1230 distances of 2,354 km (Drift1 with CO1), 622 km (Drift2 with CO2) and 345 km (Drift3 with CO3) based on hourly position data during the manned observations. These tracks are shown

in Figure 1, which also shows the continued drift of the COs after *Polarstern* has departed (Table 1). Satellite data indicate that the MOSAiC drift was about 25% faster than the climatological mean drift, and was caused by large-scale low-pressure anomalies that prevailed around the Barents-Kara-Laptev Sea region between January and March (Krumpen et al., 2021). Ice drift and deformation was tracked in the DN as well as in the CO. Figure 12 compares the ice drift speed with the wind speed for January and July and discriminates whether the floe was in free drift or moved with the closed ice pack. It reveals much higher drift speeds with a mean of 0.19 m s^{-1} in July, when the floe was in free drift, while drift speeds with a mean of 0.10 m s^{-1} were only about half that value in January, when the floe was embedded in the interior ice pack with other floes. In addition, the variability of drift speed was 1.5 times higher during free drift in July than in January. Additional analyses of this data set for the entire year will reveal details of the seasonality of different drift modes as well as dominating processes, as the start of inertial motions became more important around mid-June (Dethloff et al., 2021). Seasonal contrasts in drift and deformation patterns can also be seen in the ice radar animations over the entire CO1 (see reference to video animation in data section) Future work will analyze the interaction between ice fractures and wind forcing also on larger scales by combining the wind stress information across the DN.

Figure 12: Sea ice drift speed as a function of mean wind speed.

Figure 13 shows the rate of deformation ($\sqrt{\text{divergence}^2 + \text{shear}^2}$) derived from two consecutive Sentinel-1 SAR images in a $200 \times 200 \text{ km}$ distance centered around the MOSAiC CO for winter (December 2019) and summer (June 2020) conditions (for method see Albedyll et al., 2021). Intersecting lines of strong deformation (linear kinematic features) are present both in winter and summer ice pack. Differences in winter and summer deformation, e.g., in the degree of localization of the deformation visualized in the width of the linear kinematic features (Figure 13), are caused by changes in the ice pack strength. The seasonally varying deformation provides additional insights to the different sea ice conditions previously presented in Figure 11, and adds the larger scale to the airborne observational data. Additional analyses of spaceborne remote sensing are described in Krumpen et al. (2021). The SAR-based ice deformation can, in future, be combined with the buoy observations from the DN and the ship-radar-based deformation to obtain data products of high spatial and temporal resolution. Thus, these observations may be used towards an improved understanding of ice dynamics on different spatial scales.

Figure 13: Total deformation derived from two consecutive Sentinel-1 SAR images.

On the floe scale, Figure 14 describes the distribution of sea ice and snow thickness for January and July, and melt pond depth (for July only). The transect data (Section 2.10) shows a winter ice mode of 1.3 m and a thicker summer mode of 1.8 m (mean 2.7 m). The winter and summer modes of snow and sea ice thickness distributions demonstrate the effects of thermodynamic ice growth/decay and deformation throughout the seasonal cycle. The winter distribution features two distinct total (snow plus ice) thickness modes associated with a thinner young ice and a thicker mix of level/defomed FYI and SYI. In summer, in turn, the distribution exhibits two modes of level FYI and SYI accompanied by a broad tail of thicker ice formed by deformation processes during the preceding winter. The transect lines between winter and summer had only partial overlap. As one would expect, snow thickness was much reduced in summer compared to winter/spring, which is obvious from the reduction in modal snow

1280 thickness from 0.06 to 0.03 m. In July the modal melt pond depth was 0.1 m, with maximum depth of 0.5 m. The large coverage of melt ponds in summer is shown in Figure 11b. Results from a helicopter electromagnetic ice thickness survey on July 01, 2020, (data not shown) revealed a thicker summer modal total thickness of 2.1 m, but a thinner mean total sea ice thickness of 2.5 m over the CO and the surrounding ice within a radius of 50 km.

1285

Figure 14: Sea ice thickness and snow depth distributions.

1290 The characteristics and evolution of FYI is exemplified in Figure 15 and data are given in Tables S2 and S3. In winter (December) the upper 15 cm from the ice surface consisted of granular ice (Figure 15a), while most of the core (19–65 cm) was composed of columnar ice. A 6-cm thick skeletal layer was apparent at the core bottom (65–71 cm) of the growing FYI. While the ice in December (Figure 15b) had the typical C-shape salinity profile and was cold due to the low atmospheric temperatures, the rapid warming and desalination of FYI in summer is shown with the data from early July (Figure 15c).

1295

Figure 15: Sea ice physical properties.

1300 The surface properties of the topmost layer of sea ice showed large temporal and spatial variations throughout the MOSAiC observation period. The typical winter snowpack consisted of an often wind-packed new snow layer at the surface, with low density, large specific surface area and relatively small optical equivalent diameter (0.00–0.15 mm; Figure 16a). Due to the large temperature difference between the air and the ocean, the snowpack experienced large temperature gradients during most of the winter, which caused strong recrystallization and faceting into columnar snow structures with a strong geometric anisotropy (depth hoar). We 1305 observed the formation of euhedral crystals in the low-density regions (0.40–0.65 mm; Figure 16a), in contrast to subhedral crystals in the layers with higher densities (0.25–0.40 mm; Figure 16a). Our data show that the strong temperature gradients in the Arctic snowpack during winter cause a highly anisotropic microstructure that has significant effects on the thermal conductivity of snow and sea ice growth. In addition, they affect microwave 1310 properties for remote sensing (Figure 10). The sea ice surface in summer (Figure 16b) is generally free from snow and consists of the SSL that is formed by melting and draining processes in the sea ice. In the field visually distinguishing between snow and the SSL is hard; however, data from the micro-CT highlight the microstructural differences between the SSL 1315 and snow (Figure 16b). The density and the optical equivalent diameter increased with depth, reflecting the transition from the drained and melted sea ice at the surface to values typical of frozen sea ice (approximately 700 kg m^{-3}) toward the bottom of our sample. The specific surface area was relatively consistent, showing an increase at the surface due to preferential melting of columnar ice. The strong anisotropy of the SSL reflects the pre-existing structure of the original columnar sea ice crystals and brine channels and influences optical properties of 1320 the sea ice surface as well as remote sensing retrievals.

1325 Figure 16: Exemplary vertical profiles of the sea ice surface and snow during winter and summer.

4.4 Remaining challenges of the snow and sea ice program

The observational program of MOSAiC had to compromise in various aspects. The largest impact on the observations of the full annual cycle was that *Polarstern* had to leave the main floe (CO1) temporarily to exchange personnel and to supply the vessel. This absence resulted

1330 in a gap in manned observations between May 16 and June 19, 2020, (Table 1), a key phase of the annual cycle: the spring–summer transition and the early melt onset. The formation and decay of sea ice during the shoulder seasons is of increasing importance in the increasingly seasonal ice cover of the Arctic. Studying these processes will need dedicated expeditions to observe sea ice and snow processes of thin and very fragile ice covers in very close connection
1335 to oceanographic and atmospheric conditions. During MOSAiC, only autonomous measurements in the DN were able to bridge this gap to some extent and to obtain some key parameters continuously across this gap. Nevertheless, further studies of similar interdisciplinary complexity are needed to add more coordinated in-situ observations of this phase, where small changes in timing have large impacts on the total energy budget and the
1340 seasonality of ecological processes (Nicolaus et al., 2012).

All observations are limited to one specific drift trajectory along the Transpolar Drift from 2019 to 2020. This leaves the challenge of upscaling and generalization, which will mostly rely on merging the in-situ observations with numerical models (Section 5.2) and remote sensing
1345 (Section 5.3). Although many relevant sea ice processes were very well covered, individual parts are likely missing or lacking details. The work on the snow and sea ice properties in the DN was, in the end, quite limited both in space and time. The need for a permanent ice camp and fully manned research icebreaker for most aspects of the field program excluded most observations of marginal ice zone processes.

1350

5 Linkages within the coupled Arctic system

MOSAiC demonstrated the benefit of improved coordination across disciplines, which allowed us to study linkages and to realize ambitious plans in integrating methods and disciplines. Section 5.1 describes linkages to the individual sub-systems (including the work of the other four teams) and points to the comprehensive data sets, which will build the legacy of MOSAiC. The sampling strategy was guided by the needs of sea ice and climate models as well as for satellite remote sensing. These linkages are discussed in Sections 5.2 and 5.3, also in connection to the DN, because they allow upscaling of observations relevant for climate models and remote sensing.

5.1 Linking the individual sub-systems

Combined analyses of key parameters across all sub-systems will allow unprecedented studies of the coupled Arctic system. The physical properties of snow and sea ice are crucial for interpreting biogeochemical and biological observations as well as for understanding atmospheric composition and aerosols (Figure 4). For example, the evolution of snow and sea ice microstructure (Figures 14 and 15), porosity and permeability, is known to affect the transfer of trace gases (e.g., Nomura et al., 2018) and aerosol particles across the atmosphere-ice-ocean boundary (Frey et al., 2020). The snow on sea ice and the sea ice both act as a chemical reservoir and reactor releasing a range of chemical trace gases, aerosol particles and their precursors with significant impacts on tropospheric composition and oxidizing capacity, and potentially on climate via influencing clouds (Grannas et al., 2007). Observations of gas and particle fluxes across the atmosphere-snow-ice-ocean boundary were carried out at different scales by the BGC team and ATMOS team. Here both snow and sea ice properties from different ice types as well as ice dynamics (especially formation of leads, e.g., Figure 13) are likely crucial factors for the observed fluxes. The close coupling of the snow and sea ice cover with atmospheric forcing (especially wind forcing) became obvious (Graham et al., 2017). The dynamics of the ice pack challenged the field program, but dynamics are critical for a better understanding of energy and mass exchanges between atmosphere, sea ice, and ocean. Here we gave examples of dynamical processes with respect to the fast drift (Figure 12), the formation of leads and ridges (Figures 8 and 13), and their effects on the sea ice thickness distribution (Figure 14). While the sampling activity (coring, snow sampling) captures the seasonality, more rapid or transient changes (e.g., due to warm air advection) are more reliably covered by continuous measurements of autonomous systems; their combination provides new insights into the coupling between snow and sea ice physical properties and atmosphere–ocean exchanges.

The role of melt ponds and open water fraction was investigated intensively with respect to formation processes (Figure 5), energy budgets (Figures 7 and 9) and the impacts of their large-scale distribution (Figure 11) on the sea ice mass balance (Figure 14). Findings from these investigations will also link to concurrent ecological and biogeochemical studies. The small-scale surface heterogeneity and, in particular, the contrasts of surface temperature, trigger exchange processes between the Arctic system components. During low ice surface temperatures, the warmer open water areas or partly refrozen leads act as a source of latent and sensible heat, which modifies the atmospheric boundary layer and triggers atmospheric convection (e.g., Lüpkes et al., 2008; Schmale et al., 2021). The strong release of water vapor into the atmosphere in summer results in enhanced formation of low-level clouds and fog (Tjernström et al., 2012). While the leads represent a conduit for strong heat loss (Figure 11) and new ice formation during winter (Itkin et al., 2018), they are windows in the sunlit

1400 summer (Figure 7) period that allow more solar heating of the upper ocean (Taskjelle et al.,
2017) and intensified pelagic primary production before melt ponds appear (Assmy et al.,
2017).

1405 The observations of sea ice mass balance provide an integrated measure of the energy
balance, which is a result of the interactions and energy exchange with the atmosphere and
the ocean. Here both thermodynamic and dynamic forcing are relevant. The first observations
1410 of platelet ice in the central Arctic during winter (Katlein et al., 2020) suggest that this
mechanism can also contribute to the mass balance of Arctic sea ice. The detailed
observations of ocean heat and freshwater content and fluxes by the OCEAN team, provide
data sets to examine the interaction between upper ocean properties and sea ice under
different ice regimes.

1415 The detailed work on ridges and leads (Figure 8), in close coordination and collaboration with
oceanographic and ecological aspects, represents a leap forward from simply investigating the
level and modal snow and sea ice properties towards a much more comprehensive
understanding of the whole ice pack. These measurements allow specific analyses of
1420 deformed and ridged ice (Gradinger et al., 2010; Fernández-Méndez et al., 2018; Shestov et
al., 2018), e.g., through comparisons of sea ice habitats, energy and mass fluxes and
contrasting processes of level ice with deformed ice, thin ice, and leads.

1420 5.2 Relation to modelling

1425 A synthesis of sea ice field measurements with results from numerical models involved in
MOSAiC is expected to demonstrate how process models with different levels of complexity
and coupling can help to advance our understanding and prediction of Arctic climate change
and contribute to improved numerical weather and sea ice prediction. Some of the expected
progress is related to:

- 1430 • the assessment of unresolved, missing or overly simplified or under-represented
processes in the sea ice component of the fully coupled Arctic system;
- the exploration of inadequacies and possible improvements along the model
atmosphere-sea ice and ocean-sea ice coupling channels;
- the analysis of model sensitivities to the scale-aware sea ice parameter space;
- the placement of the MOSAiC sea ice measurements within a broader spatial (i.e., pan-
Arctic) and temporal (i.e., interannual to multi-decadal) context.

1435 Major challenges remain in how to optimally utilize observational data in different models,
including those related to

- 1440 • using Lagrangian point-observations for evaluation of gridded, space- and time-
discrete model output;
- post-processing heterogeneous, erroneous and inconsistent data sets into data
products that may be useful for model initialization, forcing and evaluation;
- bridging different scales of in-situ observations (e.g., from the CO) and remotely
sensed measurements in order to up- or down-scale such data to a model grid cell or
mesh; and
- homogenizing the heterogenous data sets of individual parameters into a common
data product, e.g., by interpolating to common time stamps or by classifying data
according to the snow and sea ice states.

On the model side, future work will be needed to:

- evaluate sea ice models and their existing parameterizations in a process-oriented manner that benefits from an improved process understanding;
- use process models, large eddy simulations or direct numerical simulations to derive, test and make available advanced parameterizations of processes impacting snow and sea ice states and variability;
- assimilate sea ice data to produce a better state estimation and forecast initial conditions for near-term forecasts; and
- derive improved sea ice forecasts and projections across timescales, including the consideration of internal and forced variability.

During the field phase of MOSAiC, different observations were realized to enable a process-oriented model evaluation and thus to assess and improve systematic model biases through improved process understanding and related parameterizations (e.g., Figure S5).

From the sea ice perspective, the most immediate connections, and thus model developments are currently expected from:

(1) Improvements to the representation of snow on sea ice (Figures 6, 14 and 16). The evolution of the snow cover (fraction, depth, distribution, thermal properties) is often overly simplistic in various types of models, e.g., in global coupled climate models (Chen et al., 2021; Webster et al., 2021) and models to reproduce re-analyses (Sato and Inoue, 2018; Batrak and Müller, 2019; Wang et al., 2019). Model sensitivity studies also indicate that the simulated climate is very sensitive to the snow representation (Urrego-Blanco et al., 2016). The new field observations cover all relevant processes (Figure 4) from freeze-up to melt, including remote sensing observations on large scales. Particular improvements are expected for estimates of snow accumulation and re-distribution over deformed ice (Liston et al., 2018), surface topography (Figures 6 and 8), thermal properties and heat transfer between atmosphere and ocean, as well as internal snow processes (Wever et al., 2020).

(2) Improvements in surface albedo and optical properties (Figures 7 and 9). The evolution of optical properties, along with other energy transfer terms, has huge implications for the total energy budget and is still one of the most critical aspects of sea ice modelling and tuning (e.g., (Holland et al., 2012; Jäkel et al., 2019). Model studies indicate that the treatment of the albedo, including factors like melt ponds, modify the transient climate evolution (e.g., Holland et al., 2012). They also show the need for inclusion of specific surface albedo for different surface types and the factors that drive the evolution of those surface types over time. Based on the MOSAiC observational data sets, better implementation of albedo schemes and melt pond thermodynamics is expected, leading to improved heat fluxes over the heterogeneous pack ice and more realistic surface energy budgets. These improvements will also have important implications for atmospheric processes and how they are represented in models, due to the strong coupling between surface fluxes and boundary layer processes.

(3) Improvements in sea ice dynamics (Figures 12 and 13). An improved inclusion of dynamical processes, including deformation and sea ice surface/bottom roughness (Figure 8) is critical for an accurate description of momentum fluxes across the atmosphere-ice-ocean interfaces and internal stress (Hutchings et al., 2011). Here, the formation and decay of ice pressure ridges and the sea ice floe size distribution are of particular importance to describe the atmosphere-ice and ice-ocean drag and internal ice stress. Both thermodynamical and dynamical processes are important for sea ice change (Dethloff et al., 2021). The main benefit of the MOSAiC observations is expected from the dedicated program on pressure ridges and

1495 leads in the CO (local scale) and the unique DN, which allows deriving dynamic parameters on a broad range of scales (e.g., ice radar, helicopter surveys, satellite remote sensing).

1500 To enable model evaluation and development of improved parameterizations, a main goal is to merge the existing observations into an explicit “MOSAiC standard forcing and 1505 benchmarking data set” for thermodynamic/dynamic sea ice models. A second goal is to advance coupling with ecological and biogeochemical processes, where the co-located measurements will be most important. They bridge across geophysical and biological aspects 1510 of snow and sea ice and allow for benchmarking simulations of causal relationships between environmental conditions and responses of different components of the Arctic sea ice ecosystem.

1515 Over the last decades, assimilation of sea ice and snow data became an important tool to study sea ice and its role in the coupled climate system and to initialize forecasts. The field data will be used to improve the assimilation of sea ice concentration, sea ice thickness and 1520 snow depth in coupled ocean–sea ice models (Fritzner et al., 2019), in particular by calibrating and validating satellite-derived products and thus reducing uncertainties in the large-scale assimilation data sets (Figure 10). The impact of assimilating sub-grid scale sea ice thickness distribution derived from Cryosat-2 and ICESat-2 observations will be assessed and support simulations with a stand-alone sea ice model.

1515 The field phase of MOSAiC also demonstrated how model applications can support and guide the field experiment. Sea ice simulations and in particular ice drift forecasts were provided to *Polarstern* in near real time through the SIDFEx initiative (Figure S5). Supplementing the atmospheric forecasts, this supported the on-ice measurement program, e.g., in planning 1520 intensified observation periods. These data sets were mainly used for near-real-time verification of the model performance and for real time educational applications.

5.3 Relation to remote sensing by aircraft and satellites

1525 As part of the MOSAiC expedition, several airborne surveys were conducted with the AWI research aircraft Polar-5 and Polar-6 from Longyearbyen (Spitsbergen) between August 17 and September 17, 2020. The aircrafts are of type Basler BT-67 and were operated by the Canadian Company Kenn Borek Air Ltd. Calgary. The main goal of these survey flights was to extend the spatially limited observations of the atmosphere and sea ice in the vicinity of CO to a larger 1530 area. While the airborne remote sensing from the *Polarstern* helicopter cover scales up to 100 km with a high, weekly temporal sampling, the aircrafts cover several hundreds of kilometers and can carry more instrumentation. When the airborne surveys began in August 2020, *Polarstern* was already on its way to the central Arctic to relocate to CO3 (Figure 1), and thus out of aircraft range. However, various DN buoys, positioned between 79°N and 81°N in 1535 early September, were still active and within range. These buoys allowed the sea ice conditions over the DN area to be recorded after *Polarstern* had departed. The surveys also complement earlier sea ice surveys made in Fram Strait between 2001 and 2018 (Belter et al., 2021). For this purpose, the aircraft Polar 6 was equipped with a number of sensors, including the EM-Bird, a laser scanner and optical instruments. Together with the laser scanner, the 1540 optical camera recorded melt pond distribution, surface elevation, floe size distribution, and other surface properties. An insight into the different sensor systems and their specifications is given in Herber et al. (2021). The track of a flight over the DN made on September 02, 2020,

is shown in Figure 1. Average ice thickness in the vicinity of the DN was 1.44 m, while the modal ice thickness was 0.93 m. Note that in parallel to the MOSAiC airborne campaign, sea 1545 ice and oceanographic surveys were carried out by the Norwegian research vessel *Kronprins Haakon* in Fram Strait, and a sea ice floe next to the vessel was overflowed while in-situ observations were taken. The second aircraft Polar 5 was equipped with in-situ, remote sensing, and basic meteorological instrumentation. The observations focused on characterizing the Arctic atmospheric boundary layer in conjunction with ocean-atmosphere 1550 interactions, clouds, solar and terrestrial radiation, and aerosols. More details about the airborne atmospheric survey program may be found in Herber et al. (2021).

Satellite observations can extend the local MOSAiC observations to regional and hemispheric scales. Long-term satellite time series and climate data records can put the MOSAiC 1555 observations into a temporal context and answer questions about how representative or unusual was the MOSAiC year (Dethloff et al., 2021; Krumpen et al., 2021). Routinely taken satellite acquisitions already provide a large collection of daily sea ice related properties from space, which will help and extend the MOSAiC data analysis: sea ice area, thickness, ice type, drift, albedo, snow depth, melt pond coverage and more. However, in addition a large 1560 collection of satellite data was acquired specifically for MOSAiC, especially high-resolution SAR and optical data. During sunlight, observations of various optical sensors with different footprints are available. WorldView-2 (meter footprint), Sentinel-2 (tens of meter footprint), Sentinel-3 and MODIS (hundreds of meter footprints) allow the scaling of in-situ to satellite observations at these scales. Several space agencies helped to acquire a unique dataset of 1565 radar backscatter images at different spatial resolution, frequencies, and polarizations from several different SAR sensors (ALOS-2, COSMO-SkyMed, KOMPSAT-5, PAZ, Radarsat Constellation Mission, SAOCOM, Sentinel-1, TerraSAR-X). This help allowed monitoring the CO and DN and an unprecedented temporal resolution of several acquisitions per day. However, MOSAiC was drifting through the “pole hole” of many satellite sensors (Figure 1) for a 1570 significant amount of time and thus not all observations are available year-around. Retrieved quantities from these higher resolution satellites acquisitions will be, e.g., floe size distributions, lead and ridge locations, ice types, ice deformation, melt pond and albedo distributions. On the other hand, the MOSAiC in-situ observations will help to improve and develop new satellite retrievals (descriptions in Sections 2 and 3 and examples in Section 4).

6 Conclusions

The snow and sea ice field program was designed to monitor all key parameters of the snow and ice system over one full annual cycle, while the intensity of observations over the year 1580 were adapted with respect to (1) deciphering sea ice evolution from autumn freeze-up to summer melt, (2) capturing key events and seasonal changes, and (3) accommodating targeted research on emerging science questions. The resulting data set will allow to better quantify the causes and consequences of the evolving and diminishing Arctic sea ice cover, as one of the central elements of the Arctic climate system. The first results show the active 1585 dynamics of the entire Arctic ice pack. MOSAiC experienced and observed rapid ice transformations and motions, and strong deformations along the drift in all seasons. These observations demonstrate the importance of dynamic processes in comparison to thermodynamic processes, as well as the role of ridges (deformed sea ice) and leads in comparison to level sea ice. Leads, in particular, link the ice pack to atmosphere-ocean exchange. The program also captured the evolution of the snow cover, across different ice 1590

types, including leads and deformed (ridged) ice. Strong temperature gradients during winter cause a highly anisotropic microstructure with significant effects on the thermal conductivity of snow. The large spatial and temporal variabilities of the snow pack impact sea ice growth and have to be considered in more detail, both in observations and in simulations. These details will allow better understanding of feedback processes between the ice and the atmosphere, including gas and particle exchange. The snow and ice measurements combined with the remote sensing observations will lead to a better understanding of sea ice microwave emission and scattering, including their temporal variability which is needed to improve satellite datasets. In particular, the role of events like the passage of low-pressure systems (storms), warm air intrusions, rain and snow fall, lead and ridge formations can be studied using integrated data sets from all key parameters. Ice-ocean interface processes, such as the formation of platelet ice, the summer freshwater layer or the roughness of the ice-ocean interface, were observed in great detail and will likely guide upcoming research with respect to the changing Arctic sea ice cover.

Even though the MOSAiC snow and sea ice work was extremely comprehensive, some aspects could only be studied in a very limited way. For example, MOSAiC was only marginally able to study the transitions of sea ice from/into open water. Dedicated studies in the marginal ice zone may be able to shed more light on this topic in the future. Furthermore, the temporary departure of *Polarstern* from the ice due to logistical reasons resulted in a gap in many of the in-situ observations during melt onset and transition into summer. Despite these limitations, we expect that the overall work will lead to a better process understanding of snow and sea ice and their linkages to atmosphere and ocean as well as improved forecast capabilities. Our expectation is that this work will strengthen research on the global coupled climate system, in particular with respect to the seasonally frozen Arctic Ocean.

Data accessibility statement

All data in this manuscript are publicly available from online repositories. Note that most data sets contain raw or preliminary data, while advanced versions will become available in future. The data may be found under the following references: drift track data (Figure 1, Nicolaus et al., doi:10.1594/PANGAEA.937204), panorama photographs (Figure 5, Nicolaus et al., doi:10.1594/PANGAEA.938534), TLS data (Figure 6, Clemens-Sewall et al., doi:10.18739/A27S7HT3B), ROV radiation data (Figure 7, Nicolaus et al., doi:10.1594/PANGAEA.935688), surface albedo data on ground (Figure 9, Smith et al., broadband data under doi:10.18739/A2KK94D36 and spectral data under doi:10.18739/A2FT8DK8Z) and from the HELiX drone (Figure 9, Calmer et al., doi:10.18739/A2GH9BB0Q), on-ice remote sensing data (Figure 10, Spreen et al., doi:10.5281/zenodo.5725870), surface images from thermal infrared and true color (Figure 11, Thielke et al., doi:10.1594/PANGAEA.934666), drift speed data from *Polarstern* (Figure 12, Nicolaus et al., doi:10.1594/PANGAEA.937204), deformation data from SAR (Figure 13, von Albedyll et al., doi:10.5281/zenodo.5195366), sea ice thickness and snow depth distribution (Figure 14, Hendricks et al., doi:10.5281/zenodo.5155244), sea ice physical properties (Figure 15, in Tables S2 and S3) with a sea ice core overview (Granskog et al., doi:10.5281/zenodo.4719905), snow pack properties (Figure 16, Macfarlane et al., doi:10.1594/PANGAEA.935934) and ship radar video sequence (Jäkel et al., doi:10.5446/52953).

Acknowledgements

1640 This work was carried out, and data used in this manuscript was produced, as part of the international Multidisciplinary drifting Observatory for the Study of the Arctic Climate (MOSAiC) with the tag MOSAiC20192020. We thank all persons involved in the expedition of the research vessel *Polarstern* during MOSAiC in 2019–2020 (AWI_PS122_00) as listed in Nixdorf et al. (2021).

1645 We highly acknowledge the contribution by Tânia Casal, Claude Duguay, Hajo Eicken, Joel Johnson, Ron Kwok, Michael Lehning, Robert Remer, Mike Schwank, and John Yackel as principal investigators on different projects that contributed to financing and enabling this work. We are grateful to Anja Nicolaus, Annekathrin Jäkel, Dirk Notz, Frederike Fohlmeister, 1650 Jeremy Wilkinson, Lovro Valic, and Pedro de la Torre for supporting the field work by the provision of instrumentation, data handling and expertise in setting up the snow and sea ice observations. We thank Marika Holland and Wieslaw Maslowski for providing comments and fruitful discussions in preparing this manuscript. The comments of Stephen Ackley and Jody Deming as editors as well as Pat Langhorne and an anonymous reviewer are highly 1655 appreciated, as they helped improve this long and complex manuscript significantly.

Funding statement

This work was funded by

- the German Federal Ministry of Education and Research (BMBF) through financing the Alfred-Wegener-Institut Helmholtz-Zentrum für Polar- und Meeresforschung (AWI) and the *Polarstern* expedition PS122 under the grant N-2014-H-060_Dethloff,
- The AWI through its projects: AWI_ROV, AWI_ICE, AWI_SNOW, AWI_ECO. The AWI buoy program and ROV work were funded by the Helmholtz strategic investment Frontiers in Arctic Marine Monitoring (FRAM)
- the Deutsche Forschungsgemeinschaft (DFG, German Research Foundation) through the Transregional Collaborative Research Centre TRR-172 “ArctiC Amplification: Climate Relevant Atmospheric and SurfaCe Processes, and Feedback Mechanisms (AC)³” (grant 268020496), the International Research Training Group 1904 ArcTrain (grant 221211316), the MOSAiCmicrowaveRS project (grant 420499875), the HELiPOD grant (LA 2907/11-1), and the SCASI (NI 1096/5-1 and KA 2694/7-1) and SnowCast (AR1236/1) projects.
- the BMBF through the projects Diatom-ARCTIC (03F0810A), IceSense (BMBF 03F0866A and 03F0866B), MOSAiC3-IceScan (BMBF 03F0916A), NiceLABpro (BMBF 03F0867A), SSIP (01LN1701A) and SIDFExplore (03F0868A),
- the German Federal Ministry for Economic Affairs and Energy through the project ArcticSense (BMWf 50EE1917A),
- the US National Science Foundation (NSF) through the project PROMIS (OPP-1724467, OPP-1724540, and OPP-1724748), the buoy work (OPP-1723400), the MiSNOW (OPP-1820927), the snow transect work (OPP-1820927), the sea ice coring work (OPP-1735862), the HELiX drone operations (OPP-1805569), surface energy fluxes (OPP-1724551), Climate Active Trace Gases (OPP-1807496), and Reactive Gas Chemistry (OPP-1914781). The last four of these were also supported by the NOAA Physical Sciences Laboratory.
- by the European Union’s Horizon 2020 research and innovation program projects ARICE (grant 730965) for berth fees associated with the participation of the DEARice team and INTAROS (grant 727890) supporting the drone and albedo measurements,

- the US Department of Energy Atmospheric Radiation Measurement (ARM) and Atmospheric System Research (ASR) programs (DE-SC0019251, DE-SC0021341)
- the National Aeronautics and Space Administration (NASA) project 80NSSC20K0658,
- 1690 - the European Space Agency (ESA) MOSAiC microwave radiometer (EMIRAD2, ELBARA, HUTRAD), (EMIRAD2, ELBARA, HUTRAD), CIMRex (contract 4000125503/18/NL/FF/gp) and GNSS-R (P.O. 5001025474, C.N. 4000128320/19/NL/FF/ab) GNSS-R (contracts P.O. 5001025474 and C.N. 4000128320/19/NL/FF/ab) projects,
- the Canadian Space Agency FAST project (grant no. 19FACALB08),
- 1695 - EUMETSAT support for microwave scatterometer measurements,
- the Research Council of Norway through the projects HAVOC (grant no. 280292), SIDRIFT (grant no. 287871), and CAATEX (grant no. 280531),
- the Fram Centre (Tromsø, Norway), from its flagship program on Arctic Ocean through the PHOTA project
- 1700 - the UKRI Natural Environment Research Council (NERC) and BMBF, who jointly funded the Changing Arctic Ocean program (project Diatom Arctic, NE/R012849/1 and 03F0810A),
- the UK Natural Environment Research Council (project SSAASI-CLIM grant NE/S00257X/1),
- 1705 - the Agencia Estatal de Investigación AEI of Spain (grant no. PCI2019-111844-2, RTI2018-099008-B-C22),
- the Swedish Research Council (VR, grant no. 2018-03859),
- the Swedish Polar Research Secretariat for berth fees for MOSAiC,
- the Swiss Polar Institute project SnowMOSAiC,
- 1710 - the Werner-Petersen-Foundation for the development of a remotely operated floating platform (grant no. FKZ 2019/610).

Contributions

Contributed to conception and design:

1715 AAF, AH, BR, BoL, BrL, CG, CH, CP, DKP, EC, ED, GB, GdB, GS, JKH, JS, JuR, KVH, LK, MAG, MDS, MN, MR, MSchn, MS, NO, RG, RKS, SG, SH, SSK, TK

Contributed to acquisition of data:

1720 AAF, AJ, AM, AN, AR, ARM, AT, AnT, BAL, BC, BH, BR, CH, CK, DC, DVD, DK, DKP, DNW, DW, ED, ES, FL, FP, GB, GS, HJB, H-RH, IAR, IO M, JB, JKH, JS, JaH, JaR, JoH, JuR, KVH, LK, LT, LvA, MA, MAG, MDS, MF, MH, MJ, MM, MMS, MN, MO, MR, Mschi, MSchn, MT, MeW, NF, NK, OD, PA, PI, RC, RD, RL, RN, RP, RR, RTT, SA, SF, SH, TK, TP, TPS, VB, VN, VaS, VIS

Contributed to analysis and interpretation of data:

1725 AJ, ARM, BoL, CG, CH, CK, DC, DVD, DKP, EC, FL, GB, GdB, GEL, GS, HFG, IO M, JH, JaH, JuR, KR, LT, LvA, MAG, MMS, MN, MO, MS, MSchn, MeW, NF, PA, PI, RC, RD, RKS, RP, RN, SH, SM, TK

Drafted and/or revised the article:

All authors

1730

Approved the submitted version for publication:

All authors

Competing interest

1735 All authors declare that they have no competing interests.

References

Albedyll, Lv, Haas, C, Dierking, W. 2021. Linking sea ice deformation to ice thickness redistribution using high-resolution satellite and airborne observations. *The Cryosphere* **15**(5): 2167–2186. doi:10.5194/tc-15-2167-2021.

1740 Alfred-Wegener-Institut Helmholtz-Zentrum für Polar- und Meeresforschung. 2017. Polar Research and Supply Vessel POLARSTERN Operated by the Alfred-Wegener-Institute. *Journal of large-scale research facilities* **3**(A119). doi:10.17815/jlsrf-3-163.

AMAP. 2017. Snow, Water, Ice and Permafrost in the Arctic (SWIPA) 2017. Oslo, Norway: Arctic Monitoring and Assessment Programme (AMAP). ISBN 978-82-7971-101-8.

1745 Assmy, P, Fernandez-Mendez, M, Duarte, P, Meyer, A, Randelhoff, A, Mundy, CJ, Olsen, LM, Kauko, HM, Bailey, A, Chierici, M, Cohen, L, Doulgeris, AP, Ehn, JK, Fransson, A, Gerland, S, Hop, H, Hudson, SR, Hughes, N, Itkin, P, Johnsen, G, King, JA, Koch, BP, Koenig, Z, Kwasniewski, S, Laney, SR, Nicolaus, M, Pavlov, AK, Polashenski, CM, Provost, C, Rosel, A, Sandbu, M, Spreen, G, Smedsrud, LH, Sundfjord, A, Taskjelle, T, Tatarek, A, Wiktor, J, Wagner, PM, Wold, A, Steen, H, Granskog, MA. 2017. Leads in Arctic pack ice enable early phytoplankton blooms below snow-covered sea ice. *Scientific Reports* **7**. doi:10.1038/srep40850.

1750 Barber, DG, Aspin, MG, Gratton, Y, Lukovich, JV, Galley, RJ, Raddatz, RL, Leitch, D. 2010. The International polar year (IPY) circumpolar flaw lead (CFL) system study: Overview and the physical system. *Atmosphere-Ocean* **48**(4): 225–243. doi:10.3137/OC317.2010.

Batrak, Y, Müller, M. 2019. On the warm bias in atmospheric reanalyses induced by the missing snow over Arctic sea-ice. *Nature Communications* **10**(1): 4170. doi:10.1038/s41467-019-11975-3.

1760 Belter, HJ, Krumpen, T, von Albedyll, L, Alekseeva, TA, Birnbaum, G, Frolov, SV, Hendricks, S, Herber, A, Polyakov, I, Raphael, I, Ricker, R, Serovetnikov, SS, Webster, M, Haas, C. 2021. Interannual variability in Transpolar Drift summer sea ice thickness and potential impact of Atlantification. *The Cryosphere* **15**(6): 2575–2591. doi:10.5194/tc-15-2575-2021.

1765 Calonne, N, Flin, F, Geindreau, C, Lesaffre, B, Rolland du Roscoat, S. 2014. Study of a temperature gradient metamorphism of snow from 3-D images: time evolution of microstructures, physical properties and their associated anisotropy. *The Cryosphere* **8**(6): 2255–2274. doi:10.5194/tc-8-2255-2014.

1770 Chen, S, Liu, J, Ding, Y, Zhang, Y, Cheng, X, Hu, Y. 2021. Assessment of snow depth over Arctic sea ice in CMIP6 models using satellite data. *Advances in Atmospheric Sciences* **38**(2): 168–186. doi:10.1007/s00376-020-0213-5.

Cheng, Y, Cheng, B, Zheng, F, Vihma, T, Kontu, A, Yang, Q, Liao, Z. 2020. Air/snow, snow/ice and ice/water interfaces detection from high-resolution vertical temperature profiles measured by ice mass-balance buoys on an Arctic lake. *Annals of Glaciology*: 1–11. doi:10.1017/aog.2020.51.

1775 Cox, GFN, Johnson, JB. 1983. *Stress measurements in ice*. Hanover, N.H.: US Army Corps of Engineers, Cold Regions Research & Engineering Laboratory. (Cold Regions, Research Engineering, Laboratory Reports).

Dethloff, K, Maslowski, W, Hendricks, S, Lee, Y, Goessling, HF, Krumpen, T, Haas, C, Handorf, D, Ricker, R, Bessonov, V, Cassano, JJ, Kinney, JC, Osinski, R, Rex, M, Rinke, A, Sokolova,

1780

J, Sommerfeld, A. 2021. Arctic sea ice anomalies during the MOSAiC winter 2019/20. *The Cryosphere Discussions* **2021**: 1–33. doi:10.5194/tc-2020-375.

1785 Fernández-Méndez, M, Olsen, LM, Kauko, HM, Meyer, A, Rösel, A, Merkouriadi, I, Mundy, CJ, Ehn, JK, Johansson, AM, Wagner, PM, Ervik, Å, Sorrell, BK, Duarte, P, Wold, A, Hop, H, Assmy, P. 2018. Algal Hot Spots in a Changing Arctic Ocean: Sea-Ice Ridges and the Snow-Ice Interface. *Frontiers in Marine Science* **5**(75). doi:10.3389/fmars.2018.00075.

Fortier, L, Cochran, JK. 2008. Introduction to special section on Annual Cycles on the Arctic Ocean Shelf. *Journal of Geophysical Research: Oceans* **113**(C3). doi:10.1029/2007JC004457.

1790 Frey, MM, Norris, SJ, Brooks, IM, Anderson, PS, Nishimura, K, Yang, X, Jones, AE, Nerentorp Mastromonaco, MG, Jones, DH, Wolff, EW. 2020. First direct observation of sea salt aerosol production from blowing snow above sea ice. *Atmospheric Chemistry and Physics* **20**(4): 2549–2578. doi:10.5194/acp-20-2549-2020.

1795 Fritzner, S, Graversen, R, Christensen, KH, Rostosky, P, Wang, K. 2019. Impact of assimilating sea ice concentration, sea ice thickness and snow depth in a coupled ocean–sea ice modelling system. *The Cryosphere* **13**(2): 491–509. doi:10.5194/tc-13-491-2019.

Frolov, IE, Gudkovich, ZM, Radionov, VF, Shirochkov, AV, Timokhov, LA. 2005. *The Arctic Basin - Results from the Russian Drifting Stations*. Berlin: Springer.

1800 Gascard, J-C, Bruemmer, B, Offermann, M, Doble, M, Wadhams, P, Forsberg, R, Hanson, S, Skourup, H, Gerland, S, Nicolaus, M, Metaxian, J-P, Grangeon, J, Haapala, J, Rinne, E, Haas, C, Heygster, G, Jakobson, E, Palo, T, Wilkinson, J, Kaleschke, L, Claffey, K, Elder, B, Bottenheim, J. 2008. Exploring Arctic Transpolar Drift During Dramatic Sea Ice Retreat. *Eos Transactions* **89**(3): 21–28.

1805 Gerland, S, Barber, D, Meier, W, Mundy, CJ, Holland, M, Kern, S, Li, Z, Michel, C, Perovich, DK, Tamura, T. 2019. Essential gaps and uncertainties in the understanding of the roles and functions of Arctic sea ice. *Environmental Research Letters* **14**(4): 043002. doi:10.1088/1748-9326/ab09b3.

Gerland, S, Haas, C. 2011. Snow-depth observations by adventurers traveling on Arctic sea ice. *Annals of Glaciology* **52**(57): 369–376.

1810 Gradinger, R, Bluhm, B, Iken, K. 2010. Arctic sea-ice ridges—Safe heavens for sea-ice fauna during periods of extreme ice melt? *Deep Sea Research Part II: Topical Studies in Oceanography* **57**(1): 86–95. doi:10.1016/j.dsr2.2009.08.008.

Graham, RM, Cohen, L, Petty, AA, Boisvert, LN, Rinke, A, Hudson, SR, Nicolaus, M, Granskog, MA. 2017. Increasing frequency and duration of Arctic winter warming events. *Geophysical Research Letters* **44**(13): 6974–6983. doi:10.1002/2017gl073395.

1815 Grannas, AM, Jones, AE, Dibb, J, Ammann, M, Anastasio, C, Beine, HJ, Bergin, M, Bottenheim, J, Boxe, CS, Carver, G, Chen, G, Crawford, JH, Dominé, F, Frey, MM, Guzmán, MI, Heard, DE, Helmig, D, Hoffmann, MR, Honrath, RE, Huey, LG, Hutterli, M, Jacobi, HW, Klán, P, Lefer, B, McConnell, J, Plane, J, Sander, R, Savarino, J, Shepson, PB, Simpson, WR, Sodeau, JR, von Glasow, R, Weller, R, Wolff, EW, Zhu, T. 2007. An overview of snow photochemistry: evidence, mechanisms and impacts. *Atmospheric Chemistry and Physics* **7**(16): 4329–4373. doi:10.5194/acp-7-4329-2007.

1820 Granskog, MA, Fer, I, Rinke, A, Steen, H. 2018. Atmosphere-Ice-Ocean-Ecosystem Processes in a Thinner Arctic Sea Ice Regime: The Norwegian Young Sea ICE (N-ICE2015) Expedition. *Journal of Geophysical Research: Oceans* **123**(3): 1586–1594. doi:10.1002/2017JC013328.

Haas, C, Hendricks, S, Eicken, H, Herber, A. 2010. Synoptic airborne thickness surveys reveal state of Arctic sea ice cover. *Geophysical Research Letters* **37**. doi:10.1029/2010gl042652.

1830 Haas, C, Le Goff, H, Audrain, S, Perovich, D, Haapala, J. 2011. Comparison of seasonal sea-ice thickness change in the Transpolar Drift observed by local ice mass-balance observations and floe-scale EM surveys. *Annals of Glaciology* **52**(57): 97–102.

Haas, C, Lobach, J, Hendricks, S, Rabenstein, L, Pfaffling, A. 2009. Helicopter-borne measurements of sea ice thickness, using a small and lightweight, digital EM system. *Journal of Applied Geophysics* **67**: 234–241.

1835 Herber, A, Becker, S, Belter, HJ, Brauchle, J, Ehrlich, A, Klingebiel, M, Krumpen, T, Lüpkes, C, Mech, M, Moser, M, Wendisch, M. 2021. MOSAiC Expedition: Airborne surveys with Research Aircraft POLAR 5 and POLAR 6 in 2020. Bremerhaven, Germany: Alfred Wegener Institute Helmholtz Centre for Polar and Marine Research: 99.

1840 Holland, MM, Bailey, DA, Briegleb, BP, Light, B, Hunke, E. 2012. Improved Sea Ice Shortwave Radiation Physics in CCSM4: The Impact of Melt Ponds and Aerosols on Arctic Sea Ice. *Journal of Climate* **25**(5): 1413–1430. doi:10.1175/Jcli-D-11-00078.1.

Hoppmann, M, Nicolaus, M, Hunkeler, PA, Heil, P, Behrens, LK, Konig-Langlo, G, Gerdes, R. 2015. Seasonal evolution of an ice-shelf influenced fast-ice regime, derived from an autonomous thermistor chain. *Journal of Geophysical Research-Oceans* **120**(3): 1703–1724. doi:10.1002/2014JC010327.

1845 Hunkeler, PA, Hoppmann, M, Hendricks, S, Kalscheuer, T, Gerdes, R. 2016. A glimpse beneath Antarctic sea ice: Platelet layer volume from multifrequency electromagnetic induction sounding. *Geophysical Research Letters* **43**(1): 222–231. doi:10.1002/2015gl065074.

Hutchings, JK, Faber, MK. 2018. Sea-Ice Morphology Change in the Canada Basin Summer: 2006–2015 Ship Observations Compared to Observations From the 1960s to the Early 1990s. *Frontiers in Earth Science* **6**(123). doi:10.3389/feart.2018.00123.

1850 Hutchings, JK, Roberts, A, Geiger, CA, Richter-Menge, J. 2011. Spatial and temporal characterization of sea-ice deformation. *Annals of Glaciology* **52**(57): 360–368. doi:10.3189/172756411795931769.

IPCC. 2013. *Climate Change 2013: The Physical Science Basis. Contribution of Working Group I to the Fifth Assessment Report of the Intergovernmental Panel on Climate Change*. Cambridge, United Kingdom and New York, NY, USA: Cambridge University Press.

1860 Itkin, P, Spreen, G, Hvidegaard, SM, Skourup, H, Wilkinson, J, Gerland, S, Granskog, MA. 2018. Contribution of Deformation to Sea Ice Mass Balance: A Case Study From an N-ICE2015 Storm. *Geophysical Research Letters* **45**(2): 789–796. doi:10.1002/2017GL076056.

Jackson, K, Wilkinson, J, Maksym, T, Meldrum, D, Beckers, J, Haas, C, Mackenzie, D. 2013. A Novel and Low-Cost Sea Ice Mass Balance Buoy. *Journal of Atmospheric and Oceanic Technology* **30**(11): 2676–2688. doi:10.1175/JTECH-D-13-00058.1.

1865 Jäkel, A, Krumpen, T, Shams, F, Albedyll, Lv, Haapala, J, Hutchings, JK, Itkin, P, Krocke, R, Spreen, G. 2021. Polarstern Ship Radar Video Sequence [dataset]. Alfred-Wegener-Institut Helmholtz-Zentrum für Polar- und Meeresforschung (AWI).

Jäkel, E, Stapf, J, Wendisch, M, Nicolaus, M, Dorn, W, Rinke, A. 2019. Validation of the sea ice surface albedo scheme of the regional climate model HIRHAM–NAOSIM using aircraft measurements during the ACLOUD/PASCAL campaigns. *The Cryosphere* **13**(6): 1695–1708. doi:10.5194/tc-13-1695-2019.

Jung, T, Gordon, ND, Bauer, P, Bromwich, DH, Chevallier, M, Day, JJ, Dawson, J, Doblas-Reyes, F, Fairall, C, Goessling, HF, Holland, M, Inoue, J, Iversen, T, Klebe, S, Lemke, P, Losch,

1875 M, Makshtas, A, Mills, B, Nurmi, P, Perovich, D, Reid, P, Renfrew, IA, Smith, G, Svensson, G, Tolstykh, M, Yang, Q. 2016. Advancing Polar Prediction Capabilities on Daily to Seasonal Time Scales. *Bulletin of the American Meteorological Society* **97**(9): 1631–1647. doi:10.1175/bams-d-14-00246.1.

1880 Kaleschke, L, Tian-Kunze, X, Maaß, N, Beitsch, A, Wernecke, A, Miernecki, M, Müller, G, Fock, BH, Gierisch, AMU, Schlünzen, KH, Pohlmann, T, Dobrynin, M, Hendricks, S, Asseng, J, Gerdes, R, Jochmann, P, Reimer, N, Holfort, J, Melsheimer, C, Heygster, G, Spreen, G, Gerland, S, King, J, Skou, N, Søbjærg, SS, Haas, C, Richter, F, Casal, T. 2016. SMOS sea ice product: Operational application and validation in the Barents Sea marginal ice zone. *Remote Sensing of Environment* **180**: 264–273. doi:10.1016/j.rse.2016.03.009.

1885 Katlein, C, Mohrholz, V, Sheikin, I, Itkin, P, Divine, DV, Stroeve, J, Jutila, A, Krampe, D, Shimanchuk, E, Raphael, I, Rabe, B, Kuznetov, I, Mallet, M, Liu, H, Hoppmann, M, Fang, Y-C, Dumitrascu, A, Arndt, S, Anhaus, P, Nicolaus, M, Matero, I, Oggier, M, Eicken, H, Haas, C. 2020. Platelet Ice Under Arctic Pack Ice in Winter. *Geophysical Research Letters* **47**(16). doi:10.1029/2020gl088898.

1890 Katlein, C, Schiller, M, Belter, HJ, Coppolaro, V, Wenslandt, D, Nicolaus, M. 2017. A New Remotely Operated Sensor Platform for Interdisciplinary Observations under Sea Ice. *Frontiers in Marine Science* **4**(281). doi:10.3389/fmars.2017.00281.

1895 Kern, S, Lavergne, T, Notz, D, Pedersen, LT, Tonboe, RT, Saldo, R, Sørensen, AM. 2019. Satellite passive microwave sea-ice concentration data set intercomparison: closed ice and ship-based observations. *The Cryosphere* **13**(12): 3261–3307. doi:10.5194/tc-13-3261-2019.

König, M, Hieronymi, M, Oppelt, N. 2019. Application of Sentinel-2 MSI in Arctic Research: Evaluating the Performance of Atmospheric Correction Approaches Over Arctic Sea Ice. *Frontiers in Earth Science* **7**(22). doi:10.3389/feart.2019.00022.

1900 König, M, Oppelt, N. 2020. A linear model to derive melt pond depth on Arctic sea ice from hyperspectral data. *The Cryosphere* **14**(8): 2567–2579. doi:10.5194/tc-14-2567-2020.

Krumpen, T, Birrien, F, Kauker, F, Rackow, T, von Albedyll, L, Angelopoulos, M, Belter, HJ, Bessonov, V, Damm, E, Dethloff, K, Haapala, J, Haas, C, Harris, C, Hendricks, S, Hoelemann, J, Hoppmann, M, Kaleschke, L, Karcher, M, Kolabutin, N, Lei, R, Lenz, J, Morgenstern, A, Nicolaus, M, Nixdorf, U, Petrovsky, T, Rabe, B, Rabenstein, L, Rex, M, Ricker, R, Rohde, J, Shimanchuk, E, Singha, S, Smolyanitsky, V, Sokolov, V, Stanton, T, Timofeeva, A, Tsamados, M, Watkins, D. 2020. The MOSAiC ice floe: sediment-laden survivor from the Siberian shelf. *The Cryosphere* **14**(7): 2173–2187. doi:10.5194/tc-14-2173-2020.

1910 Krumpen, T, von Albedyll, L, Goessling, HF, Hendricks, S, Juhls, B, Spreen, G, Willmes, S, Belter, HJ, Dethloff, K, Haas, C, Kaleschke, L, Katlein, C, Tian-Kunze, X, Ricker, R, Rostosky, P, Rückert, J, Singha, S, Sokolova, J. 2021. MOSAiC drift expedition from October 2019 to July 2020: sea ice conditions from space and comparison with previous years. *The Cryosphere* **15**(8): 3897–3920. doi:10.5194/tc-15-3897-2021.

1915 Kwok, R, Kurtz, NT, Brucker, L, Ivanoff, A, Newman, T, Farrell, SL, King, J, Howell, S, Webster, MA, Paden, J, Leuschen, C, MacGregor, JA, Richter-Menge, J, Harbeck, J, Tschudi, M. 2017. Intercomparison of snow depth retrievals over Arctic sea ice from radar data acquired by Operation IceBridge. *The Cryosphere* **11**(6): 2571–2593. doi:10.5194/tc-11-2571-2017.

1920 Lawrence, IR, Tsamados, MC, Stroeve, JC, Armitage, TWK, Ridout, AL. 2018. Estimating snow depth over Arctic sea ice from calibrated dual-frequency radar freeboards. *Cryosphere* **12**(11): 3551–3564. doi:10.5194/tc-12-3551-2018.

1925 Light, B, Grenfell, TC, Perovich, DK. 2008. Transmission and absorption of solar radiation by Arctic sea ice during the melt season. *Journal of Geophysical Research* **113**(C03023). doi:10.1029/2006JC003977.

1930 Liston, GE, Polashenski, C, Rösel, A, Itkin, P, King, J, Merkouriadi, I, Haapala, J. 2018. A Distributed Snow-Evolution Model for Sea-Ice Applications (SnowModel). *Journal of Geophysical Research: Oceans* **123**(5): 3786–3810. doi:10.1002/2017JC013706.

Lüpkes, C, Vihma, T, Birnbaum, G, Wacker, U. 2008. Influence of leads in sea ice on the temperature of the atmospheric boundary layer during polar night. *Geophysical Research Letters* **35**(3). doi:10.1029/2007GL032461.

1935 MacGregor, JA, Boisvert, LN, Medley, B, Petty, AA, Harbeck, JP, Bell, RE, Blair, JB, Blanchard-Wrigglesworth, E, Buckley, EM, Christoffersen, MS, Cochran, JR, Csathó, BM, De Marco, EL, Dominguez, RT, Fahnestock, MA, Farrell, SL, Gogineni, SP, Greenbaum, JS, Hansen, CM, Hofton, MA, Holt, JW, Jezek, KC, Koenig, LS, Kurtz, NT, Kwok, R, Larsen, CF, Leuschen, CJ, Locke, CD, Manizade, SS, Martin, S, Neumann, TA, Nowicki, SMJ, Paden, JD, Richter-Menge, JA, Rignot, EJ, Rodríguez-Morales, F, Siegfried, MR, Smith, BE, Sonntag, JG, Studinger, M, Tinto, KJ, Truffer, M, Wagner, TP, Woods, JE, Young, DA, Yungel, JK. 2021. The scientific legacy of NASA's Operation IceBridge. *Reviews of Geophysics* **59**(2). doi:10.1029/2020RG000712.

1940 Manes, SS, Gradinger, R. 2009. Small scale vertical gradients of Arctic ice algal photophysiological properties. *Photosynthesis Research* **102**(1): 53–66. doi:10.1007/s11120-009-9489-0.

1945 Marsan, D, Weiss, J, Métaxian, J-P, Grangeon, J, Roux, P-F, Haapala, J. 2011. Low-frequency bursts of horizontally polarized waves in the Arctic sea-ice cover. *Journal of Glaciology* **57**(202): 231–237. doi:10.3189/002214311796405834.

1950 Matzl, M, Schneebeli, M. 2006. Measuring specific surface area of snow by near-infrared photography. *Journal of Glaciology* **52**(179): 558–564. doi:10.3189/172756506781828412.

Munoz-Martin, JF, Perez, A, Camps, A, Ribó, S, Cardellach, E, Stroeve, J, Nandan, V, Itkin, P, Tonboe, R, Hendricks, S, Huntemann, M, Spreen, G, Pastena, M. 2020. Snow and Ice Thickness Retrievals Using GNSS-R: Preliminary Results of the MOSAiC Experiment. *Remote Sensing* **12**(24): 4038. doi:10.3390/rs12244038.

Nansen, F. 1897. *Den Norske Polarfaerd 1893-1896*. Kristiania: Aschehoug.

1955 Nicolaus, M, Gerland, S, Hudson, SR, Hanson, S, Haapala, J, Perovich, DK. 2010. Seasonality of spectral albedo and transmittance as observed in the Arctic Transpolar Drift in 2007. *Journal of Geophysical Research-Oceans* **115**. doi:10.1029/2009jc006074.

1960 Nicolaus, M, Hoppmann, M, Arndt, S, Hendricks, S, Katlein, C, Nicolaus, A, Rossmann, L, Schiller, M, Schwegmann, S. 2021. Snow Depth and Air Temperature Seasonality on Sea Ice Derived From Snow Buoy Measurements. *Frontiers in Marine Science* **8**(377). doi:10.3389/fmars.2021.655446.

Nicolaus, M, Katlein, C, Maslanik, J, Hendricks, S. 2012. Changes in Arctic sea ice result in increasing light transmittance and absorption. *Geophysical Research Letters* **39**(24): L24501. doi:10.1029/2012GL053738.

1965 Nixdorf, U, Dethloff, K, Rex, M, Shupe, M, Sommerfeld, A, Perovich, D, Nicolaus, M, Heuzé, C, Rabe, B, Loose, B, Damm, E, Gradinger, R, Fong, A, Maslowski, W, Rinke, A, Kwok, R, Spreen, G, Wendisch, M, Herber, A, Hirsekorn, M, Mohaupt, V, Frickenhaus, S, Immerz, A, Weiss-Tuider, K, König, B, Mengedoht, D, Regnery, J, Gerchow, P, Ransby, D, Krumpen, T, Morgenstern, A, Haas, C, Kanzow, T, Rack, FR, Saitzev, V, Sokolov, V,

1970 Makarov, A, Schwarze, S, Wunderlich, T, Wurr, K, Boetius, A. 2021. MOSAiC extended acknowledgement *Zenodo*. doi:10.5281/zenodo.5179739.

1975 Nomura, D, Granskog, MA, Fransson, A, Chierici, M, Silyakova, A, Ohshima, KI, Cohen, L, Delille, B, Hudson, SR, Dieckmann, GS. 2018. CO₂ flux over young and snow-covered Arctic pack ice in winter and spring. *Biogeosciences* **15**(11): 3331–3343. doi:10.5194/bg-15-3331-2018.

Oggier, M, Eicken, H, Jin, M, Høyland, K. 2020. Seasonal and interannual variability of sea-ice state variables: Observations and predictions for landfast ice in northern Alaska and Svalbard. *The Cryosphere Discuss* **2020**: 1–28. doi:10.5194/tc-2020-52.

1980 Oikkonen, A, Haapala, J, Lensu, M, Karvonen, J, Itkin, P. 2017. Small-scale sea ice deformation during N-ICE2015: From compact pack ice to marginal ice zone. *Journal of Geophysical Research: Oceans* **122**(6): 5105–5120. doi:10.1002/2016JC012387.

1985 Pațilea, C, Heygster, G, Huntemann, M, Spreen, G. 2019. Combined SMAP–SMOS thin sea ice thickness retrieval. *The Cryosphere* **13**(2): 675–691. doi:10.5194/tc-13-675-2019.

Perovich, DK, Andreas, WL, Curry, JA, Eicken, H, Fairall, CW, Grenfell, TC, Guest, PS, Intrieri, J, Kadko, D, Lindsay, RW, McPhee, MG, Morison, J, Moritz, RE, Paulson, CA, Pegau, WS, Persson, POG, Pinkel, R, Richter-Menge, J, Stanton, T, Stern, H, Sturm, M, Tucker III, WB, Uttal, T. 1999. Year on ice gives climate insights. *Eos Transactions* **80**(41): 485–486.

1990 Picard, G, Sandells, M, Löwe, H. 2018. SMRT: an active–passive microwave radiative transfer model for snow with multiple microstructure and scattering formulations (v1.0). *Geosci Model Dev* **11**(7): 2763–2788. doi:10.5194/gmd-11-2763-2018.

Polashenski, C, Perovich, DK, Richter-Menge, J, Elder, B. 2011. Seasonal ice mass-balance buoys: adapting tools to the changing Arctic. *Annals of Glaciology* **52**(57): 18–26.

1995 Proksch, M, Löwe, H, Schneebeli, M. 2015. Density, specific surface area, and correlation length of snow measured by high-resolution penetrometry. *Journal of Geophysical Research: Earth Surface* **120**(2): 346–362. doi:10.1002/2014JF003266.

Pustogvar, A, Kulyakhtin, A. 2016. Sea ice density measurements. Methods and uncertainties. *Cold Regions Science and Technology* **131**: 46–52. doi:10.1016/j.coldregions.2016.09.001.

2000 Rigor, I, Ortmeyer, M. 2003. The International Arctic Buoy Programme (IABP). *AGU Fall Meeting Abstracts*.

Sato, K, Inoue, J. 2018. Comparison of Arctic sea ice thickness and snow depth estimates from CFSR with in situ observations. *Climate Dynamics* **50**(1): 289–301. doi:10.1007/s00382-017-3607-z.

2005 Schmale, J, Zieger, P, Ekman, AML. 2021. Aerosols in current and future Arctic climate. *Nature Climate Change* **11**(2): 95–105. doi:10.1038/s41558-020-00969-5.

2010 Semmling, AM, Wickert, J, Kress, F, Hoque, MM, Divine, DV, Gerland, S, Spreen, G. 2021. Sea-ice permittivity derived from GNSS reflection profiles: Results of the MOSAiC expedition. *Ieee Transactions on Geoscience and Remote Sensing*. doi:10.1109/TGRS.2021.3121993.

Shestov, A, Høyland, K, Ervik, Å. 2018. Decay phase thermodynamics of ice ridges in the Arctic Ocean. *Cold Regions Science and Technology* **152**: 23–34. doi:10.1016/j.coldregions.2018.04.005.

2015 Stroeve, J, Nandan, V, Willatt, R, Tonboe, R, Hendricks, S, Ricker, R, Mead, J, Mallett, R, Huntemann, M, Itkin, P, Schneebeli, M, Krampe, D, Spreen, G, Wilkinson, J, Matero, I, Hoppmann, M, Tsamados, M. 2020. Surface-based Ku- and Ka-band polarimetric radar for sea ice studies. *The Cryosphere* **14**(12): 4405–4426. doi:10.5194/tc-14-4405-2020.

Sturm, M, Holmgren, JA. 1999. Self-recording snow depth probe.

Sturm, M, Massom, RA. 2017. Snow in the sea ice system: friend or foe? *Sea Ice*. 65–109.

2020 Taskjelle, T, Granskog, MA, Pavlov, AK, Hudson, SR, Hamre, B. 2017. Effects of an Arctic under-ice bloom on solar radiant heating of the water column. *Journal of Geophysical Research: Oceans* **122**(1): 126–138. doi:10.1002/2016JC012187.

Thoman, RL, Richter-Menge, J, Druckenmiller, ML. 2020. NOAA Arctic Report Card 2020 Executive Summary. doi:10.25923/mn5p-t549.

2025 Tjernström, M, Birch, CE, Brooks, IM, Shupe, MD, Persson, POG, Sedlar, J, Mauritsen, T, Leck, C, Paatero, J, Szczerba, M, Wheeler, CR. 2012. Meteorological conditions in the central Arctic summer during the Arctic Summer Cloud Ocean Study (ASCOS). *Atmos Chem Phys* **12**(15): 6863–6889. doi:10.5194/acp-12-6863-2012.

Tonboe, RT. 2010. The simulated sea ice thermal microwave emission at window and sounding frequencies. *Tellus Series A* **62**: 333. doi:10.1111/j.1600-0870.2009.00434.x.

2030 Ulaby, FT, Long, DG. 2014. Microwave Radar and Radiometric Remote Sensing.

Untersteiner, N. 1961. On the mass and heat budget of Arctic sea ice. *Arch Meteorol Geophys Bioklimatol Ser. A*, **12**: 151–182.

Untersteiner, N, Thorndike, AS, Rothrock, DA, Hunkins, KL. 2007. AIDJEX Revisited: A Look Back at the U.S.-Canadian Arctic Ice Dynamics Joint Experiment 1970-78. *Arctic* **60**(3): 327–336.

2035 Urrego-Blanco, JR, Urban, NM, Hunke, EC, Turner, AK, Jeffery, N. 2016. Uncertainty quantification and global sensitivity analysis of the Los Alamos sea ice model. *Journal of Geophysical Research: Oceans* **121**(4): 2709–2732. doi:10.1002/2015JC011558.

2040 Wang, C, Graham, RM, Wang, K, Gerland, S, Granskog, MA. 2019. Comparison of ERA5 and ERA-Interim near-surface air temperature, snowfall and precipitation over Arctic sea ice: effects on sea ice thermodynamics and evolution. *The Cryosphere* **13**(6): 1661–1679. doi:10.5194/tc-13-1661-2019.

Webster, M, Gerland, S, Holland, M, Hunke, E, Kwok, R, Lecomte, O, Massom, R, Perovich, D, 2045 Sturm, M. 2018. Snow in the changing sea-ice systems. *Nature Climate Change* **8**(11): 946–953. doi:10.1038/s41558-018-0286-7.

Webster, MA, DuVivier, AK, Holland, MM, Bailey, DA. 2021. Snow on Arctic Sea Ice in a Warming Climate as Simulated in CESM. *Journal of Geophysical Research: Oceans* **126**(1). doi:10.1029/2020JC016308.

2050 Weissenberger, J, Dieckmann, G, Gradinger, R, Spindler, M. 1992. Sea ice: A cast technique to examine and analyze brine pockets and channel structure. *Limnology and Oceanography* **37**(1): 179–183.

Wever, N, Rossmann, L, Maaß, N, Leonard, KC, Kaleschke, L, Nicolaus, M, Lehning, M. 2020. Version 1 of a sea ice module for the physics-based, detailed, multi-layer SNOWPACK model. *Geosci Model Dev* **13**(1): 99–119. doi:10.5194/gmd-13-99-2020.

2055 Wollenburg, JE, Iversen, M, Katlein, C, Krumpen, T, Nicolaus, M, Castellani, G, Peeken, I, Flores, H. 2020. New observations of the distribution, morphology and dissolution dynamics of cryogenic gypsum in the Arctic Ocean. *The Cryosphere* **14**(6): 1795–1808. doi:10.5194/tc-14-1795-2020.

2060

Figure legends

2065 Figure 1. Drift tracks of the central observatories (CO) of MOSAiC in 2019–2020. Colored segments illustrate the month of the drift of the COs (Table 1) with thick parts indicating the manned drifts, and thin parts the unmanned drift. The black lines show the tracks of *Polarstern*. The grey line shows the drift track of the floe prior to the MOSAiC drift and the dashed black line, the flight track of the MOSAiC aircraft campaign on September 02, 2070 2020. Circles indicate the pole holes of different satellites: 89°N, e.g., AMSR2; 88°N, e.g., CryoSat2, IceSat-2, SMOS; 87.5°N, e.g., Sentinel-1. The background shows the sea ice extent for the March 2020 maximum and the September minima for 2019 and 2020. Labels denote the start of the legs and COs.

2075 Figure 2. Main sites and installations in the central observatory at the end of Leg 3 (CO1). Note that panel B extends the map in A to the left (join the arrows). The background shows the airborne laser scanner image from April 23, 2020 with grey areas indicating “no data”. Due to active ice dynamics, the positions of some sites were approximated, and some sites were outside of the map range or were destroyed. The term “old” refers to sites that were active 2080 earlier during the expedition but were no longer maintained at the end of Leg 3.

2085 Figure 3. Snow and sea ice observations during the field phase of MOSAiC. Each row shows dates when continuous (lines) or discrete (points) measurements were performed. Dark grey and white areas indicate the legs, light blue areas indicate the time 2090 when *Polarstern* drifted with the COs, light grey columns (during Legs 2 and 4) indicate the times of the case studies described in Section 4.3. (A) On-ice and airborne measurements, (B) remote sensing instruments on the ice and on *Polarstern*. Abbreviations: Hyperspectral camera, IR/video camera. Acronyms are listed in Table S1. Color description for rows with multiple colors from top to bottom (red: r, green: g, blue: b, magenta: m, yellow: y):

2095 Drone flights: (r) HELiX, (g) Mavic and Spectra Quadrocopter;
Ice mechanics: (r) Hydrocomplex, (g) bore hole jack, (b) both;
Albedo lines: (r) spectral + broadband, (g) spectral only, (b) broadband only;
Ponds: (r) remotely controlled water color spectroradiometers, (g) hand-held water color spectroradiometers, (b) water sample, (m) pond depth;

2100 Coring: (r) FYI, (g) SYI, (b) FYI+SYI, (m) Ridge, (y) other sites;
ROV: (r) Sensor data only, (g) Additional net on ROV;
Helicopter: (r) Laserscanner + cameras, (g) HEM bird, (b) Helipod;
Bridge observations: (r) at station, (b) during transit;
Panomax: (r) daylight conditions, (b) darkness;

2105 Radiation station: (r) daylight conditions, (b) darkness;
C-SCAT: (r) regular measurements, (b) recorded data with problems;
HUTRAD: (r) regular measurements, (b) recorded data with problems.
ARIEL: (r) regular measurements, (b) recorded data with problems.

2110 Figure 4. Schematics of the snow and sea ice processes studied during MOSAiC. The close-up illustrations focus on the snow-ice (left) and ice-ocean (right) interfaces.

Figure 5: The ‘sea ice clock’. Photographs from the MOSAiC floe arranged clockwise with one picture per month (January to December). Photographs were recorded by the panorama camera on the crow’s nest of

Polarstern and show the view ahead of the vessel. Photos were selected to be representative for the month while providing best available image quality.

Figure 6. Snow redistribution observed via terrestrial laser scanning (TLS).

2115 (A) Complete TLS scan from January 25, 2020, colored by topographic relief, (B) 40 x 40 m close up of that scan, (C) perspective view from the viewpoint (eyeball and yellow triangle in (B) towards the ridge, and (D) comparison of the topographic relief along the transect line for both scans, with 95% confidence intervals for the surface reconstruction in each profile shown in shading.

2120 Figure 7. Light transmittance through sea ice measured with the remotely operated vehicle. (Top row) transmittance (integrated 350–920 nm) along the dive track at 2 m depth for 6 dives in July 2020. (Bottom row) histogram of light transmittance derived from the above dive.

2125 Figure 8. The Jaridge ridge and adjacent lead in summer 2020.

(A) Approximate surface elevation of the sea ice or snow surface from airborne laser scanning on June 30, 2020, (B) Bottom topography from the multi-beam sonar on the remotely operated vehicle (ROV) Beast on June 25, 2020, (C) Surface photography on July 04, 2020, and (D) Surface photography with surface installations and *Polarstern* in the background on July 21, 2020. In B) the location of the ROV hut, sediment trap deployment, IMB (2020M26) deployment and the approximate views of C and D are indicated. The dashed lines indicate the locations of consecutive drilling transects across the ridge.

Figure 9. Surface albedo during summer (Leg 4).

2135 (A) Broadband surface albedo and (B) spectral surface albedo along the 200-m-long Lemon Drop line on July 06, 2020, (Leg 4). Broadband measurements in blue and spectral measurements were completed on the ground (1 m height), and broadband measurements in red were taken from the drone (HELiX) with a flight altitude of 15 m. Shading represents the standard deviation of 2-m spatially averaged measurements (recorded at 1 Hz). (C) Photomosaic taken from the drone with the red line showing location of the drone measured albedo line in (A).

Figure 10. Remote sensing signatures during winter and summer.

2145 Results from co-located active and passive remote sensing instruments (Table 2) viewing similar ice and snow conditions (Figure S4). Left panels: measurements during a warming and storm event in November 2019; and right panels: during a melting event in September 2020. (A) Air temperature and wind speed from the *Polarstern* weather station and snow surface temperature from the IR camera at the remote sensing site (dashed blue line shows time periods with potential icing on the lens). (B) Radar backscatter at VV polarization from microwave scatterometers L-SCAT at 1.3 GHz and Ku/Ka-radar at 15 and 35 GHz (note the different y-scales). (C) Brightness temperature at V polarization from microwave radiometers: ELBARA at 1.4 GHz, ARIEL at 1.4 GHz looking at thin ice on a lead, HUTRAD at 7 and 11 GHz, Special Sensor Microwave Imager at 19, 37, 89 GHz (not all available data shown). (D) Reflected GNSS data, i.e., reflectivity at the remote sensing site (blue) and for sea ice next to *Polarstern* (red). The panel titles give the incidence angles used. Vertical dashed lines mark the start of warming and/or storm events. (E) Example photographs of the remote sensing site during winter and summer.

Figure 11. Aerial photo mosaics of the central observatory and its surroundings.

2160 (A) Thermal infrared image on January 21, 2020, (B) Visual (RGB) image on June 30, 2020. The red line shows the perimeter of the central observatory during summer (Leg 4) and its approximate position in the winter pack ice during Leg 2 (dashed line), thus allowing the alignment of both images. The position of *Polarstern* at the floe is indicated with the arrow, also showing that most parts of the central observatory were at a different location during 2165 Leg 2 than during Leg 4. The rotation against geographic north resulted mainly from the drift of the ice pack past the North Pole, less from rotation.

Figure 12. Sea ice drift speed as a function of mean wind speed.

2170 Data were measured onboard *Polarstern* for one week in January and July 2020, respectively. Point clouds show all measurements, large dots and bars give the mean and one standard deviation. The free drift estimate (solid line) is based on "Nansen-Ekman ice drift law", which assumes that ice drift speed equals to 2% of the wind speed.

Figure 13. Total deformation derived from two consecutive Sentinel-1 SAR images.

2175 Data cover 200 x 200 km distance of the MOSAiC central observatory in (A) winter acquired on December 30–31, 2019, and (B) summer acquired on June 20–21, 2020. White arrows display sea ice motion.

Figure 14. Sea ice thickness and snow depth distributions.

2180 Probability density functions (PDF, histogram areas normalized to 1) of (A) total (sea ice plus snow) and (B) snow thickness along the transect loops (Figure 2) on January 23 and July 07, 2020. (C) Melt pond depth on July 07, 2020, as derived from the snow probe modified for melt pond measurements.

2185 Figure 15. Sea ice physical properties from ice cores.

(A) Stratigraphy of an ice core collected at the first-year ice site on December 02, 2019. Vertical (rectangular) and horizontal (circular) thin sections photographed between crossed polarizers. (B) Temperature and salinity of first-year sea ice from the ice cores on December 02, 2019 (solid lines; sample 1_10-FYI, core length 0.71 m), and July 06, 2020, (dashed lines; sample 2190 4_46-FYI, core length 1.60 m). Photos of coring sites are shown in Figure S2. The snow/ice surface is on top, freeboard at 0 m.

Figure 16: Example vertical profiles of the snow pack during winter and summer.

(A) The snowpack on January 10, 2020 and (B) the sea ice surface with the surface scattering 2195 layer on July 06, 2020. The depth profiles on the left show density, specific surface area and grain size (optically equivalent diameter, OED) analyzed from the micro-CT. In addition, the 3-dimensional reconstruction of the microstructure from the same dataset can be seen on the right. The y-axis gives the depth with the snow surface at 0 m (top) and the ice surface at the bottom of the profile.

Tables for
Overview of the MOSAiC expedition – Snow and Sea Ice

Table 1. Key dates of the MOSAiC expedition.

Date	Comment	Expedition Leg	Observatory ^a
Sep 20, 2019	Departure from Tromsø	Start Leg 1	-
Oct 04, 2019	Start Drift 1	-	Start CO1
Oct 07, 2019	First buoys deployed in DN1	-	Start DN1
Dec 13, 2019	Resupply and personnel exchange, on site	Leg 1 => Leg 2	-
Feb 24, 2020	Resupply and personnel exchange, on site	Leg 2 => Leg 3	-
May 16, 2020	End Drift 1	-	-
Jun 04, 2020	Resupply and personnel exchange, Svalbard	Leg 3 => Leg4	-
Jun 19, 2020	Start Drift 2	-	Start CO2
Jul 31, 2020	End Drift 2	-	-
Aug 12, 2020	Resupply and personnel exchange, Fram Strait	Leg 4 => Leg 5	-
Aug 21, 2020	Start Drift 3	-	Start CO3 + DN2
Sep 20, 2020	End Drift 3	-	-
Oct 12, 2020	Arrival in Bremerhaven	End Leg 5	-

^a CO1 to CO3 denote the three different central observatories and DN1 and DN2 denote the two distributed networks. The term “drift” refers to the manned drift, when *Polarstern* was drifting with the corresponding CO. Note that no end dates are given for the COs and DNs, because autonomous stations continued reporting beyond the manned drift.

Table 2. Overview of sea ice remote sensing (RS) instruments operated during MOSAiC.

Frequency band	Name	Location	Channels	Polarization	Corresponding satellites/sensors
Microwave radiometers					
UHF to L-band	UWBRAD	RS site	0.54, 0.9, 1.38, 1.74 GHz	single (right-hand-circular)	proposed future mission
L-band	ELBARA	RS site	1.4 GHz	dual-polarization (H, V)	SMOS, SMAP, CIMR
L-band	EMIRAD2	<i>Polarstern</i>	1.4 GHz	full polarimetric	SMOS, SMAP, CIMR
L-band	ARIEL	Transects	1.413 GHz	dual-polarization (H, V)	SMOS, SMAP, CIMR
C- to K-band	HUTRAD	RS site	6.85, 10.65, 18.70 GHz	dual-polarization (H, V)	AMSR-E/2/3, CIMR
K- to W-band	SSMI	RS site	19, 37, 89 GHz	dual-polarization (H, V)	SSM/I, SSMIS, FY-3, AMSR-E/2/3, CIMR
Radars					
L-band	L-SCAT	RS site	1.26 GHz	full polarimetric (HH, VV, HV, VH)	ALOS/PALSAR 1, -2, and -3; SAOCOM; NISAR; ROSE-L
C-band	C-SCAT	RS site	5.55 GHz	full polarimetric (HH, VV, HV, VH)	Sentinel-1, Radarsat-1/2, Radarsat Constellation Mission; ASCAT
X-band	X-SCAT	RS site	9.65 GHz	full polarimetric (HH, VV, HV, VH)	TerraSAR-X, PAZ, COSMO-Skymed, KOMPSAT-5
Ku-, Ka-band	Ku/Ka-Radar	RS site and transects	12-18 GHz, 30-40 GHz; nadir (altimeter) and scatterometer operation	dual-polarization (H, V)	CryoSat-2, Sentinel-3, AltiKa, ERS-1/2, Envisat, CRYSTAL altimeters; QuikSCAT, OSCAT, CFOSAT scatterometers
Others					
L-band	GNSS-R on ice	RS site	Reflected GNSS signals at L1 (1.6 GHz) and L2 (1.2 GHz)	right-handed (RHCP) and left-handed circular polarization (LHCP)	ESA FSSCat, UK TDS-1, ESA PRETTY, China FY-3E and Taiwan FS-7R
L-band	GNSS-R on <i>Polarstern</i>	<i>Polarstern</i>	Reflected GNSS signals at L1 (1.6 GHz) and L2 (1.2 GHz)	right-handed (RHCP) and left-handed circular polarization (LHCP)	ESA FSSCat, UK TDS-1, ESA PRETTY, China FY-3E and Taiwan FS-7R
Infrared and visual	IR/video camera	RS site	7.5–14 μ m, visual	Not applicable	MODIS, VIIRS, Envisat, Sentinel-3
Visual to NIR	Hyperspectral camera	RS site	400–1000 nm in 204 spectral bands	Not applicable	MODIS, VIIRS, Sentinel-3, Sentinel-2, ICESat-2

Table 3. Table of key parameters of the MOSAiC snow and sea ice program.

Parameter by Category	1 General ^{a,b}	2 Snow	3 Ice coring	4 Mass balance	5 Terres. laser scan	6 Optics	7 Ponds	8 Dynamics	9 Ridges	10 Transects	11 ROV	12 Helicopter	13 Remote sensing	Methods or Instruments
Sea ice and snow mass balance														
Thickness, sea ice														
Thickness, sea ice	-	-	X	X	-	-	-	-	-	X	X	X	-	Electromagnetic induction, drilling, coring, sonar, thermal properties
Thickness, snow	-	-	-	X	X	-	-	-	-	X	-	X	-	Magna probe, laser scanning, drilling, coring, sonar, stake readings
Snow water equivalent	-	X	-	-	-	-	-	-	-	-	-	-	-	Snow pit
Bottom topography	-	-	-	-	-	-	-	-	-	X	X	-	-	Electro magnetics, sonar
Surface roughness	-	-	-	-	X	-	-	-	-	-	-	X	-	Laser scanning
Freeboard	-	-	X	X	-	-	-	-	-	-	-	X	-	Coring, laser scanning
Floe size (distribution)	X	-	-	-	-	-	-	X	-	-	-	X	-	Cameras, bridge obs.
Lateral melt rate	-	-	-	-	-	-	-	-	-	-	-	X	-	Cameras
Sea ice and snow physical properties														
Salinity, snow and sea ice														
Salinity, snow and sea ice	-	X	X	X	-	-	-	-	-	-	-	-	-	Snow pit, coring, conductivity sensor, salt harp
Temperature, sea ice	-	-	X	X	-	-	-	-	-	-	-	-	-	Temperature probe, thermistor strings
Density, sea ice	-	-	X	-	-	-	-	-	-	-	-	-	-	Hydrostatic density kit
Texture / microstructure, snow and sea ice	-	-	X	-	-	-	-	X	-	-	-	-	-	Visual inspection, cameras, Micro-CT
Porosity, sea ice and ridges	-	-	X	-	-	-	-	-	-	X	X	X	-	Sonar, Electromagnetic induction, coring
Sea ice microstructure / stratigraphy	-	X	X	-	-	-	-	X	-	-	-	-	-	Coring, Micro-CT
Snow density, stratigraphy, hardness	-	X	-	-	-	-	-	-	-	-	-	-	-	Snow pit, SMP
Snow grain size, specific surface area	-	X	-	-	-	-	-	-	-	-	-	-	-	Snow pit, Micro-CT, SMP, NIR
Temperature, snow	-	X	-	X	-	-	-	-	-	-	-	-	-	Snow pit, thermistor strings
Stable oxygen isotope ratio (O18), snow and sea ice	-	X	X	-	-	-	-	-	-	-	-	-	-	Snow pit, coring
Snow surface roughness (small-scale)	-	X	-	-	-	-	-	-	-	-	-	-	-	Snow pit
Energy budget, optical properties and melt ponds														
Irradiance, spectral and broadband														
Irradiance, spectral and broadband	X	-	-	-	-	X	-	-	-	-	X	X	-	Radiometers (manual, stations, drones, helicopter, ROV)
Albedo, spectral and broadband	-	-	-	-	-	X	-	-	-	-	-	X	-	Radiometers (manual, stations, drones, helicopter)
Transmittance, spectral and broadband	-	-	-	-	-	X	-	-	-	-	X	-	-	Radiometers (manual, stations, ROV), hyperspectral imager
IOP, spectral, snow and ice and ponds	-	-	-	-	-	X	X	-	-	-	-	-	-	Optical probe, propelled platform
Impurities	-	X	X	-	-	-	X	-	-	-	-	-	-	Snow pit, coring, water samples
Depth, melt ponds	-	-	-	-	-	-	X	-	-	X	-	X	-	Magna probe water samples, propelled platform, cameras
Geometry and coverage, melt ponds	X	-	-	-	-	X	-	-	-	-	-	X	-	Cameras

Temperature, melt ponds	-	-	-	-	-	-	X	-	-	-	-	-	-	Water samples
Salinity, melt ponds	-	-	-	-	-	-	X	-	-	-	-	-	-	Water samples
Bottom imagery, melt ponds	-	-	-	-	-	-	-	-	-	-	X	-	-	Cameras
Surface properties	X	-	-	-	-	-	-	-	-	-	X	X	-	Cameras, bridge observations
Dynamical and mechanical properties														
Location	-	-	-	-	-	-	-	X	-	-	-	-	-	Position buoys, GNSS
Deformation	X	-	X	-	-	-	-	X	-	-	-	X	-	Ship Radar, laser scanning, cameras, position buoys
Stress	-	-	-	-	-	-	-	X	-	-	-	-	-	Stress buoys
Strength	-	-	-	-	-	-	-	X	-	-	-	-	-	Uniaxial tests, borehole jack
Seismics	-	-	-	-	-	-	-	X	-	-	-	-	-	Seismometers
Microwave properties														
Emission	-	-	-	-	-	-	-	-	-	-	-	X	-	Radiometers ARIEL, ELBARA, EMIRAD2 HUTRAD, SSMII, UWBRAD
Backscatter	-	-	-	-	-	-	-	-	-	-	-	X	-	Radars L-, C-, X-SCAT, Ku/Ka-Radar
Reflectivity	-	-	-	-	-	-	-	-	-	-	-	X	-	GNSS-R on ice and <i>Polarstern</i> , Ku/Ka-Radar
Dielectric Permittivity	-	-	-	-	-	-	-	-	-	-	-	X	-	Vector Network Analyzer and open-end microwave resonator sensor, HydraProbe, GNSS-R
Supplemental observations														
Temperature, ocean	-	-	X	X	-	-	-	-	-	-	X	-	-	Temperature sensors, thermistor strings
Salinity, ocean	-	-	X	-	-	-	-	-	-	-	X	-	-	Conductivity sensor
Conductive heat fluxes	-	-	-	X	-	-	-	-	-	-	-	-	-	IMB
Air temperature	-	-	-	X	-	-	-	-	-	-	-	-	-	Temperature sensors
Photo documentation	X	X	-	-	-	X	X	-	-	-	X	X	X	Cameras
Infrared images	-	-	-	-	-	-	-	-	-	-	X	X	-	IR cameras
General snow and ice conditions	X	-	-	-	-	-	-	-	-	-	X	X	-	Bridge observations, cameras

^a Task and method terms are explained in Section 2 with the sub-section given through the number of the task (e.g., “1 General” > “2.1 General snow and ice observations”).

^b Entries are sorted by topics according to Section 3 of this manuscript.

Figures for Overview of the MOSAiC expedition – Snow and Sea Ice

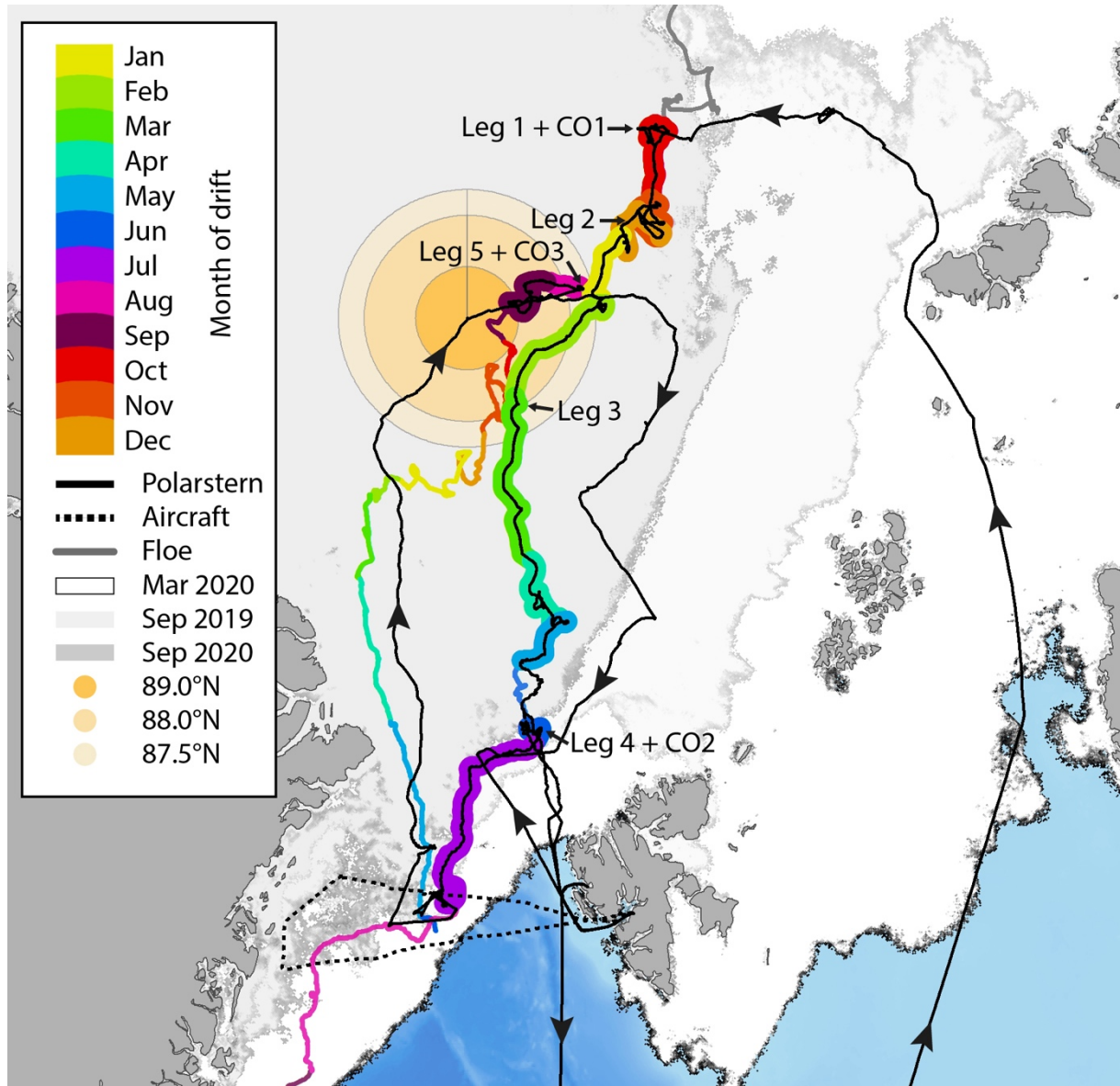


Figure 1. Drift tracks of the central observatories (CO) of MOSAiC in 2019–2020.

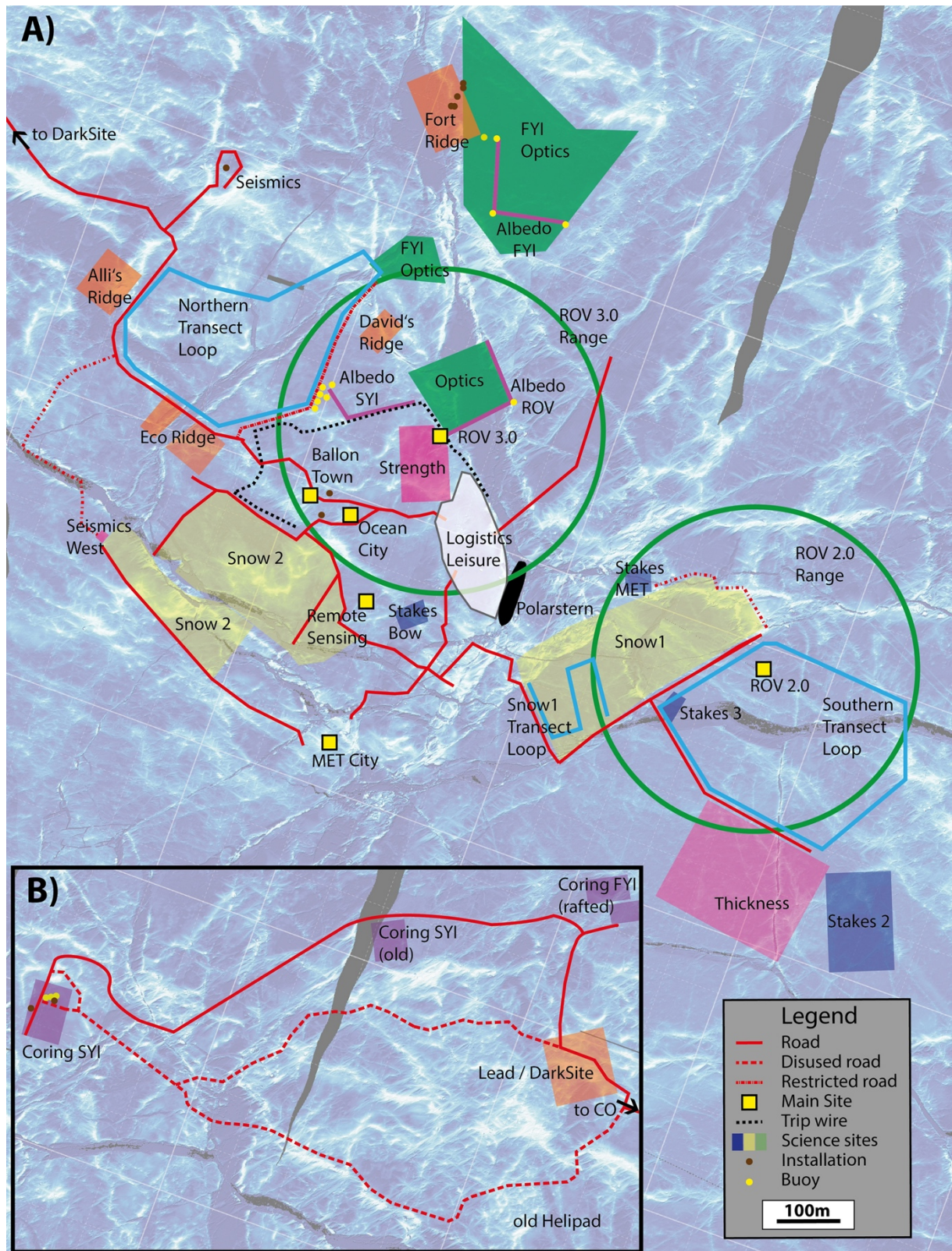


Figure 2. Main sites and installations in the central observatory at the end of Leg 3 (CO1).

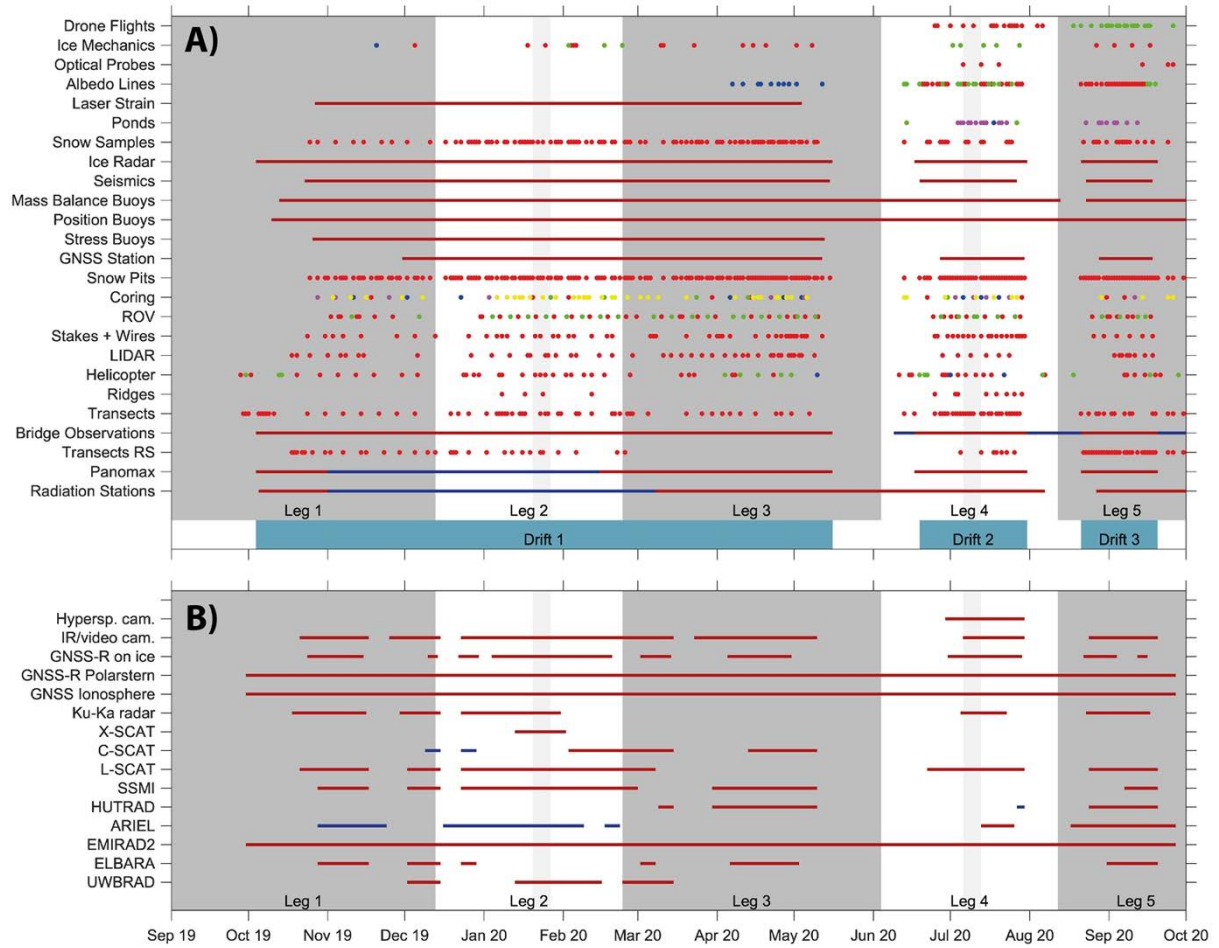


Figure 3. Snow and sea ice observations during the field phase of MOSAiC.

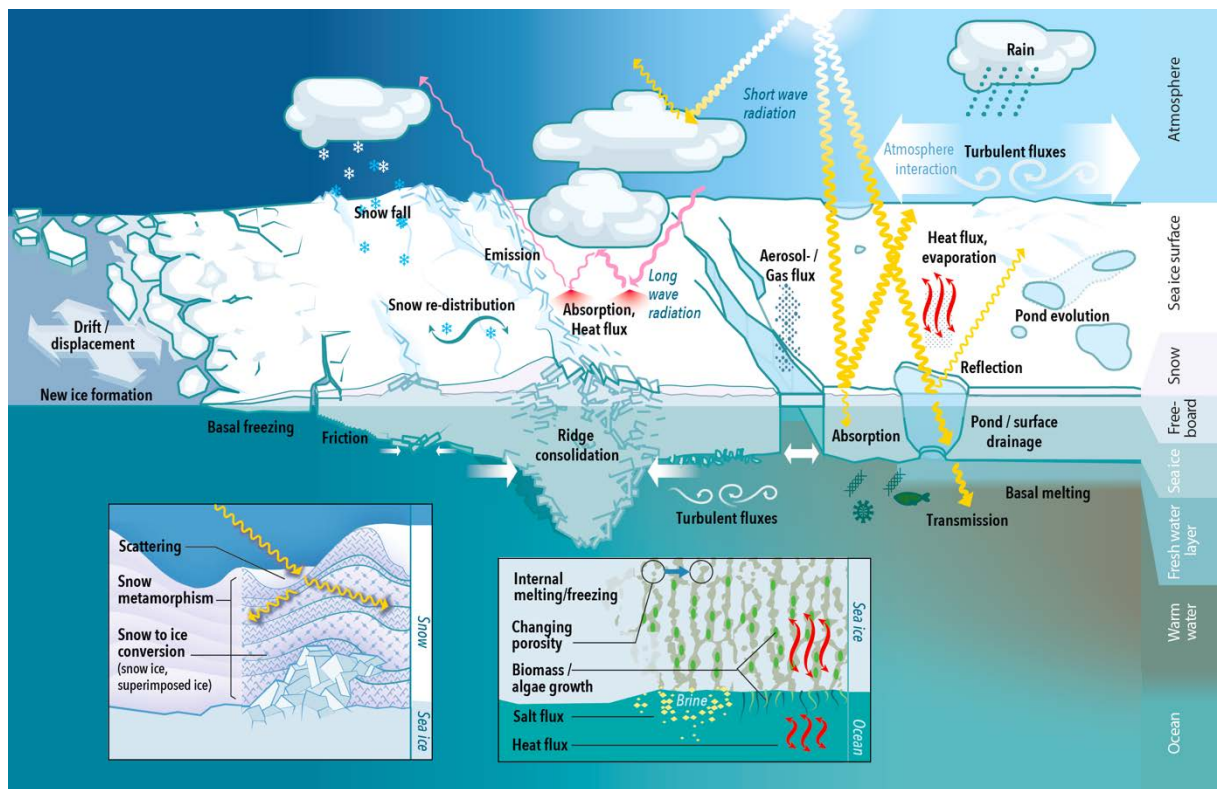


Figure 4. Schematics of the snow and sea ice processes studied during MOSAiC.

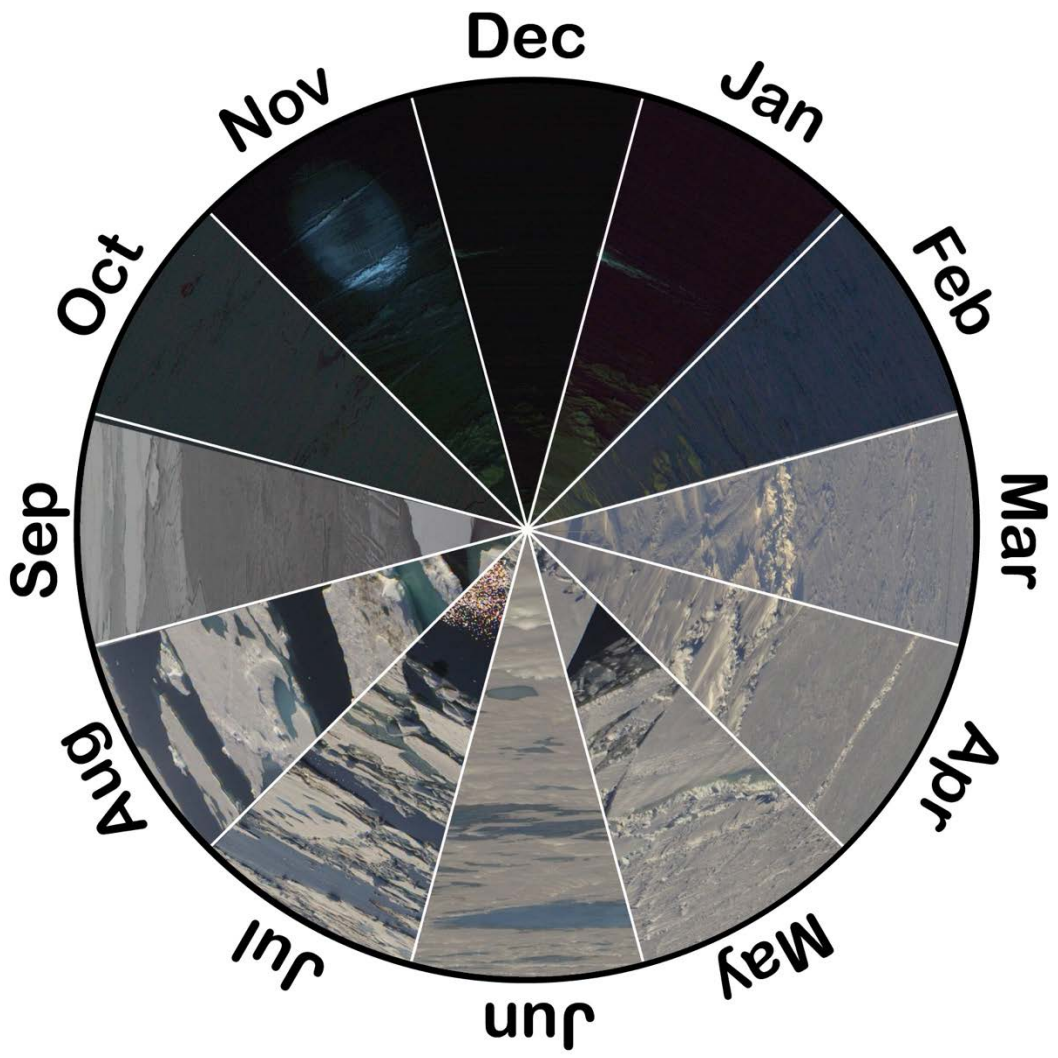


Figure 5. The 'sea ice clock'.

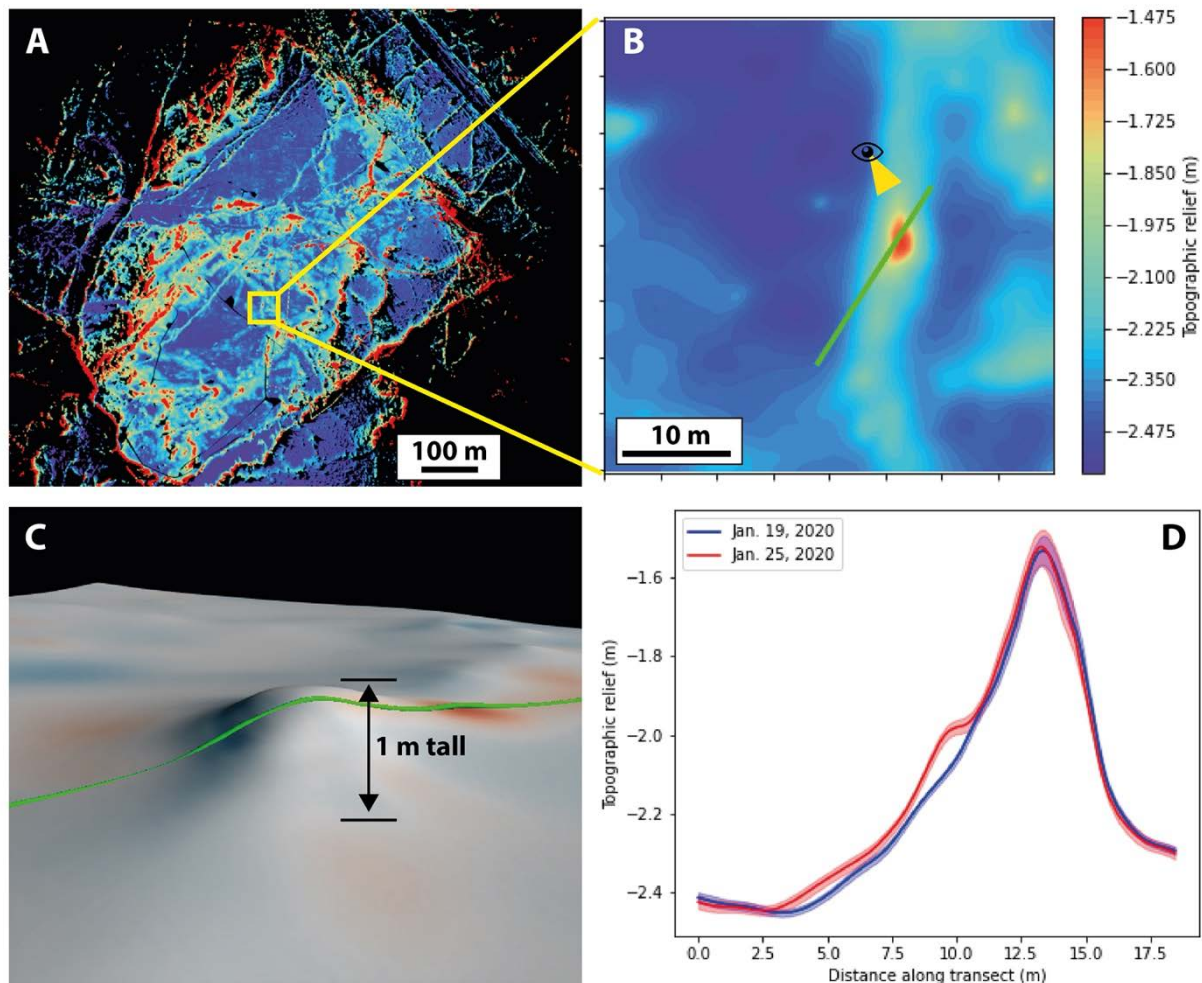


Figure 6. Snow redistribution observed via terrestrial laser scanning (TLS).

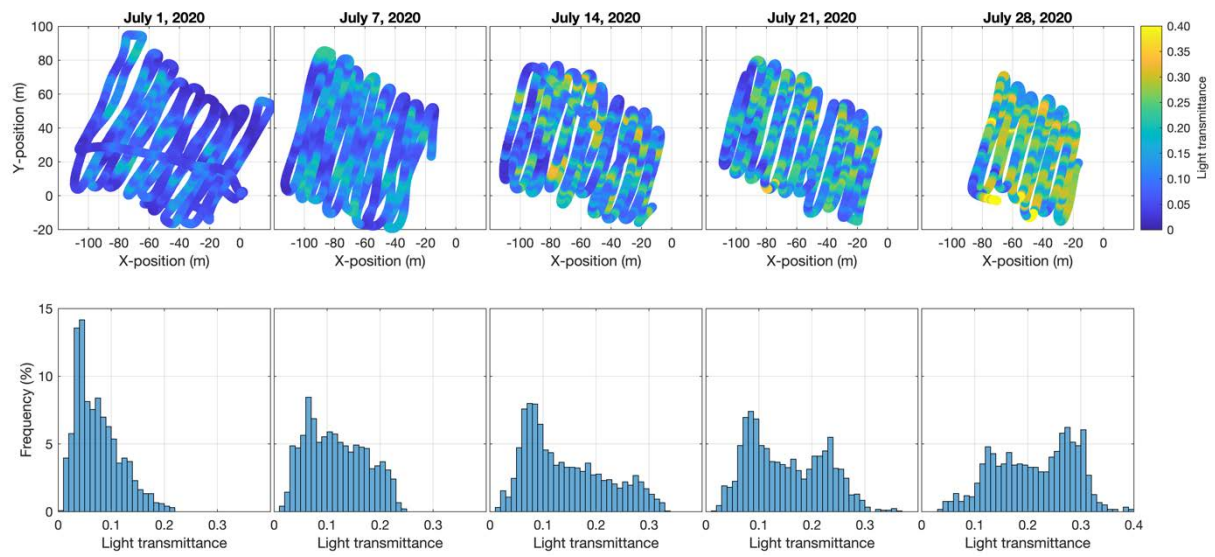


Figure 7. Light transmittance through sea ice measured with the remotely operated vehicle.

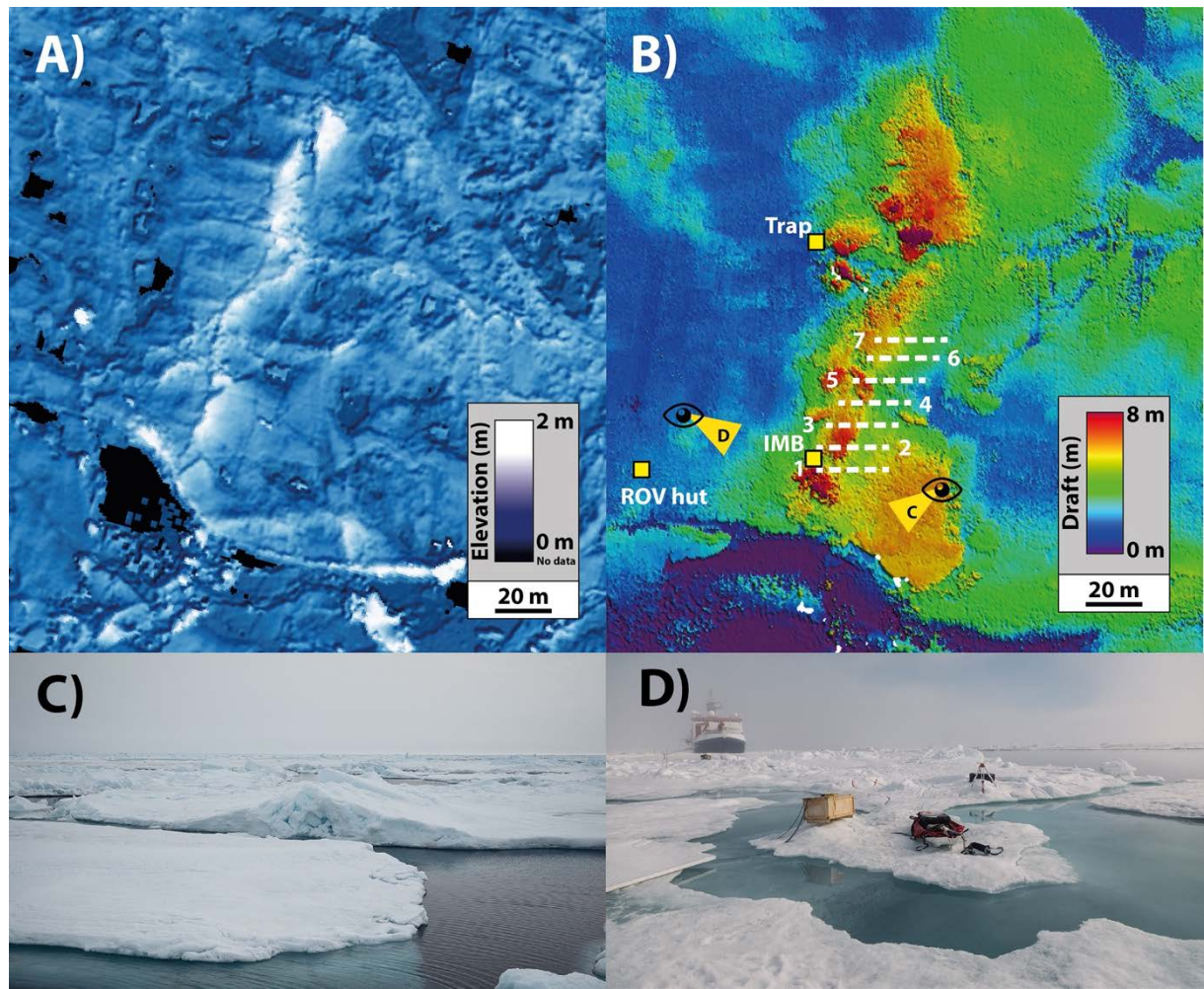


Figure 8. The Jaridge ridge and adjacent lead in summer 2020 (Leg 4).

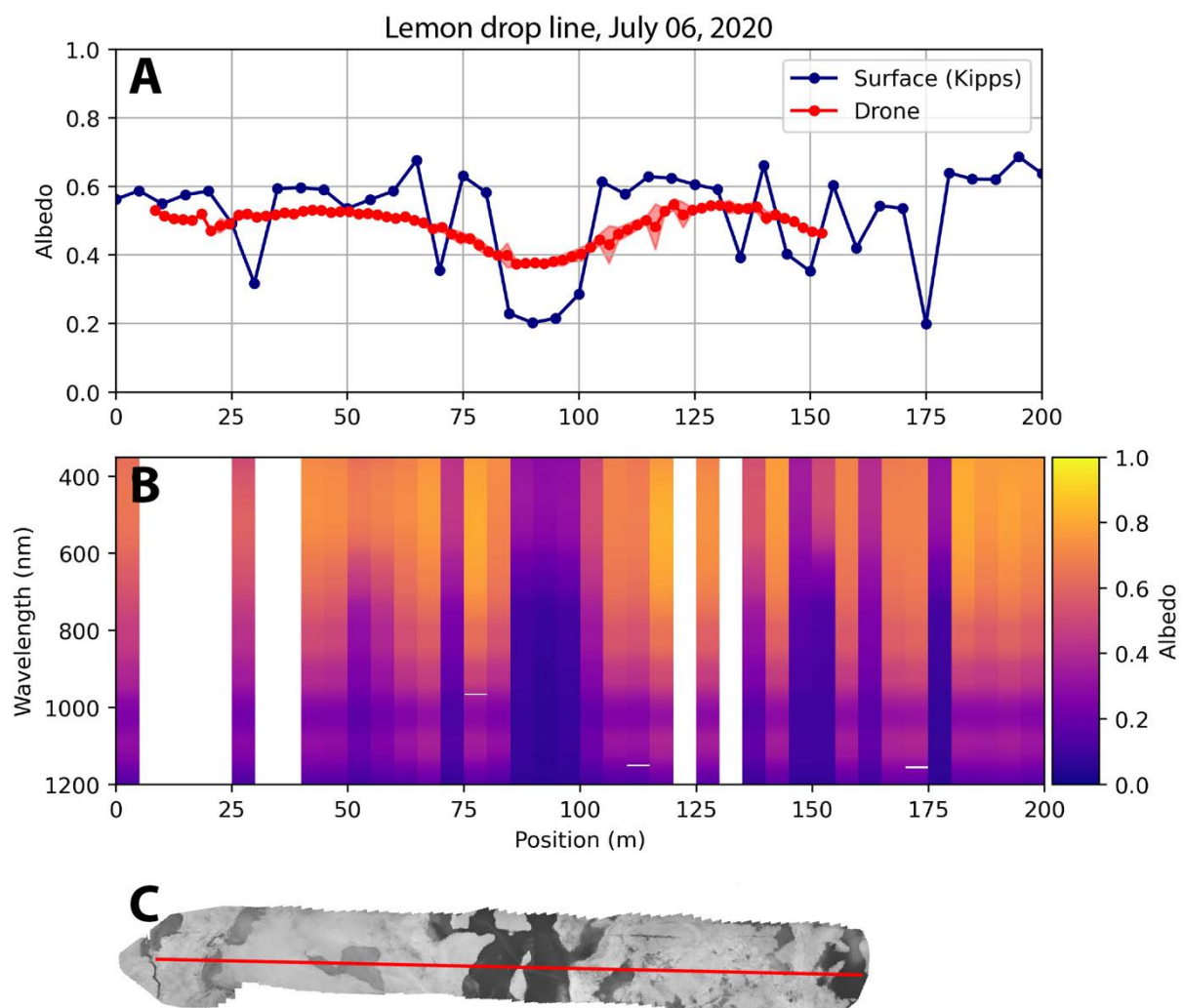


Figure 9. Surface albedo during summer (Leg 4).

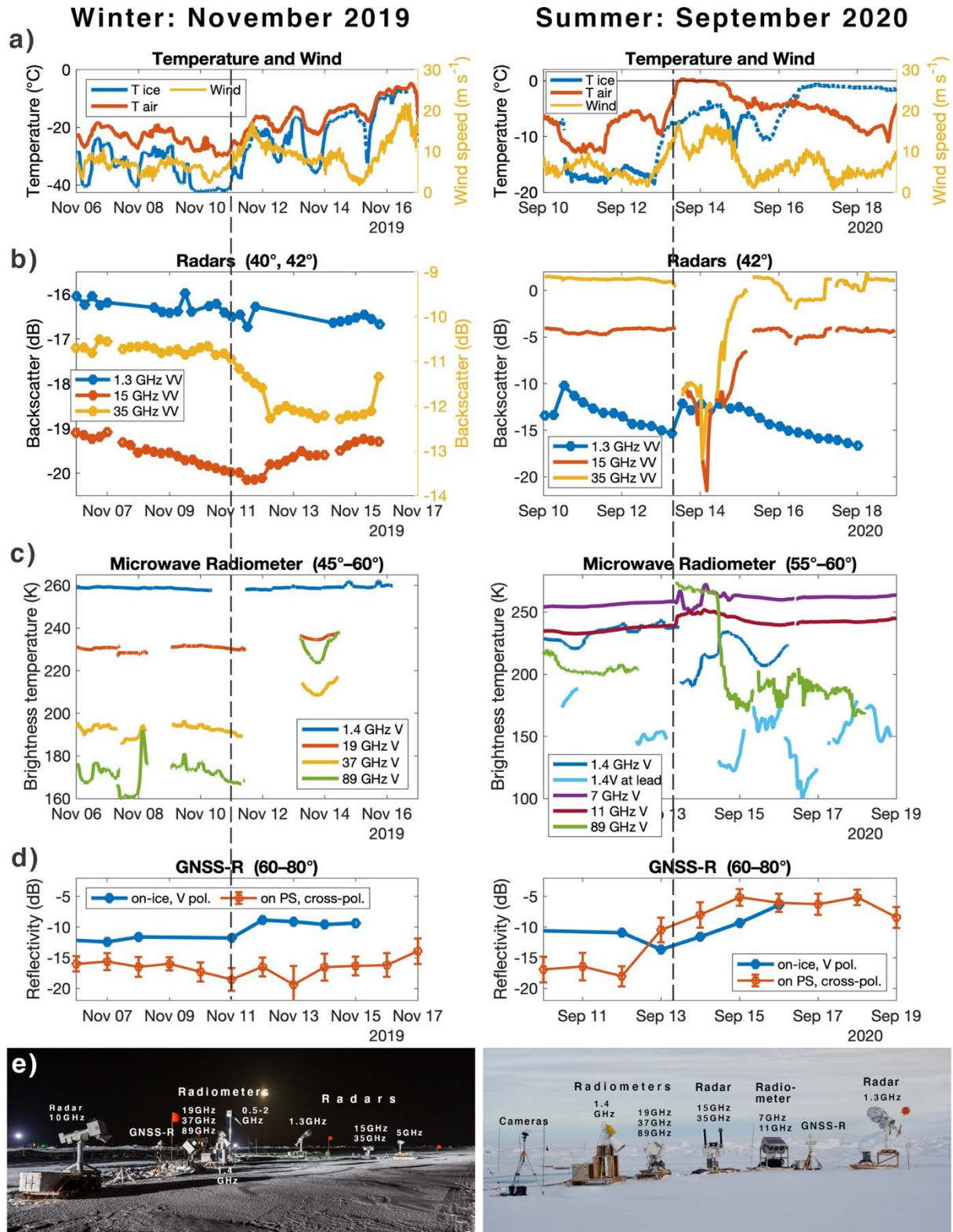
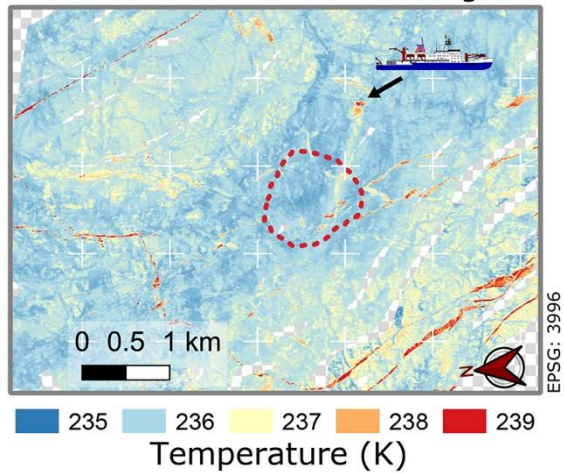


Figure 10. Remote sensing signatures during winter and summer.

A) Jan 21, 2020
Winter: Thermal infrared image



B) June 30, 2020
Summer: True-color image

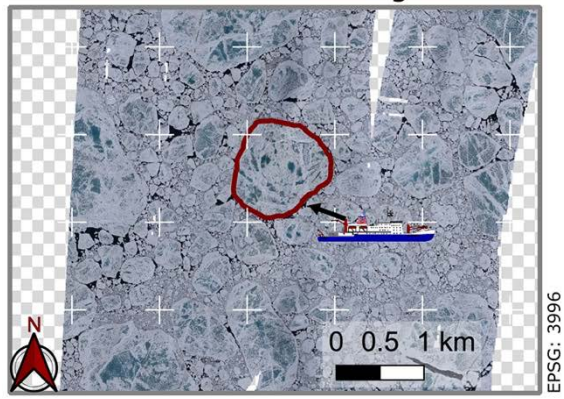


Figure 11. Aerial photo mosaics of the central observatory and its surroundings.

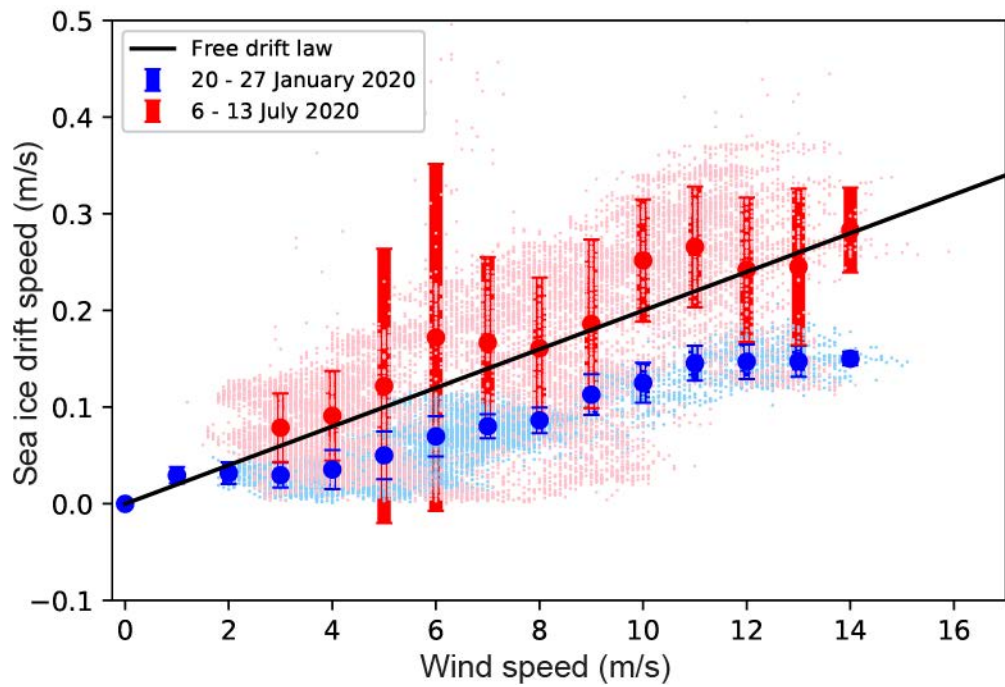


Figure 12. Sea ice drift speed as a function of mean wind speed.

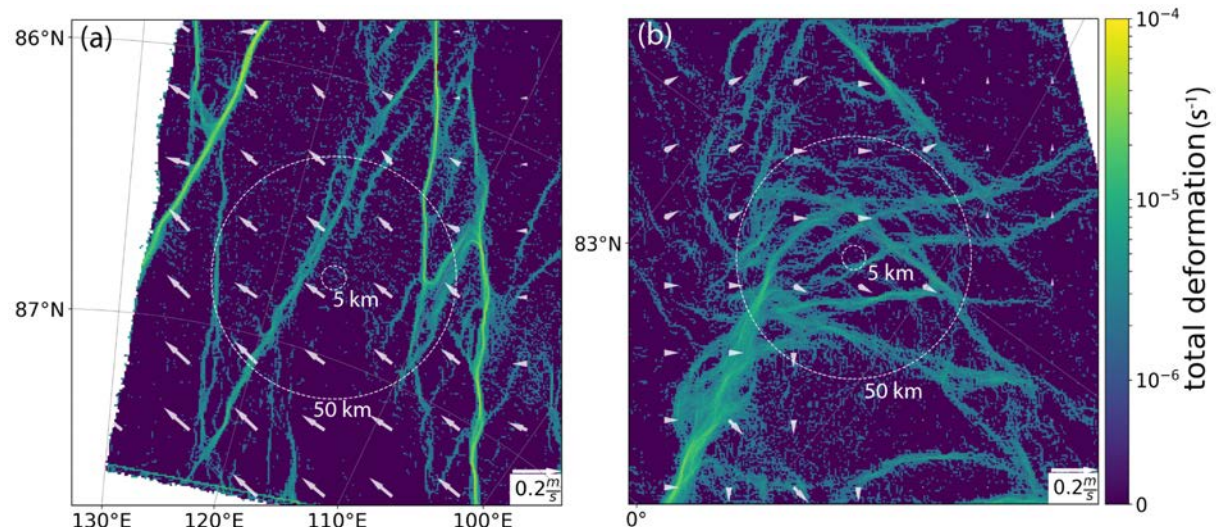


Figure 13. Total deformation derived from two consecutive Sentinel-1 SAR images.

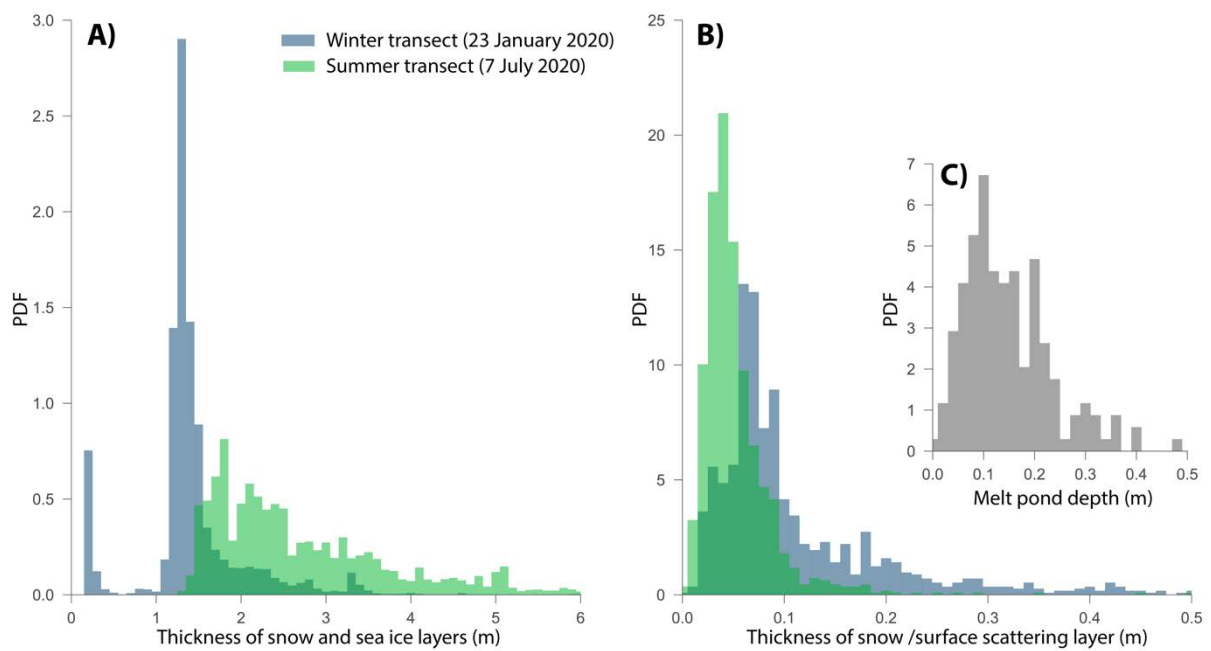


Figure 14. Sea ice thickness and snow depth distributions.

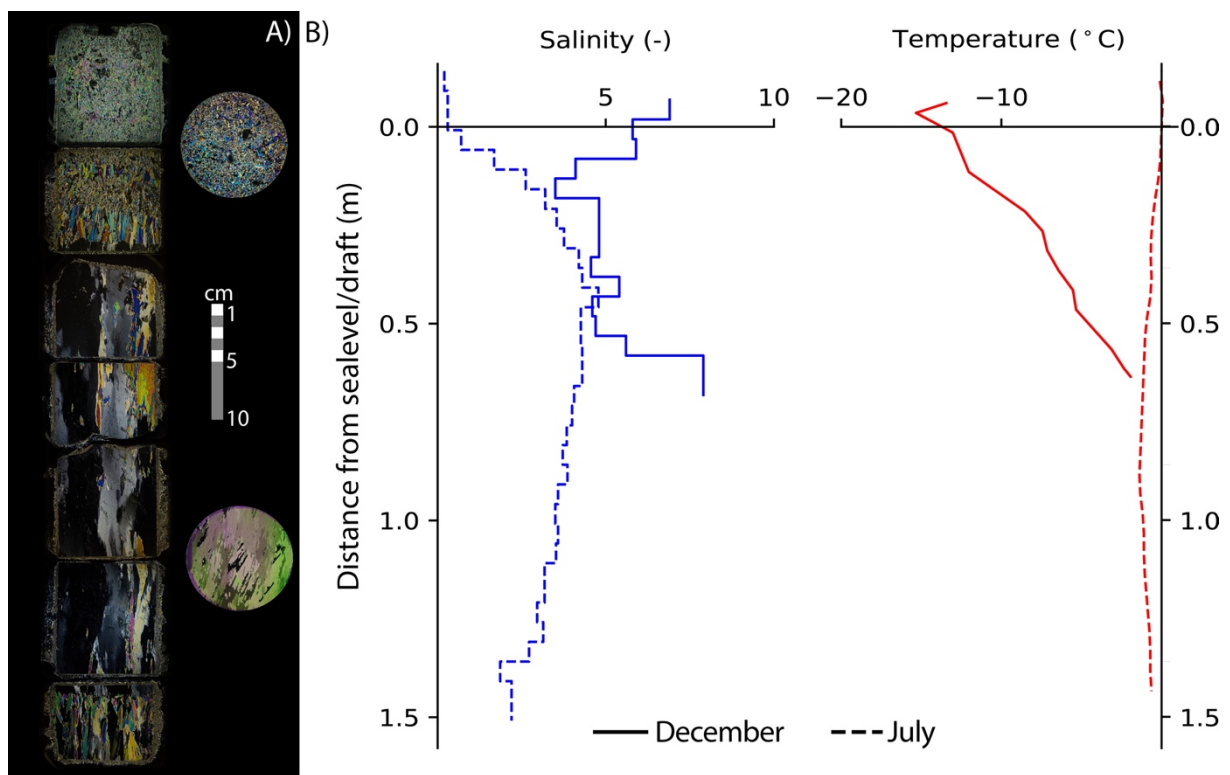


Figure 15. Sea ice physical properties from ice cores.

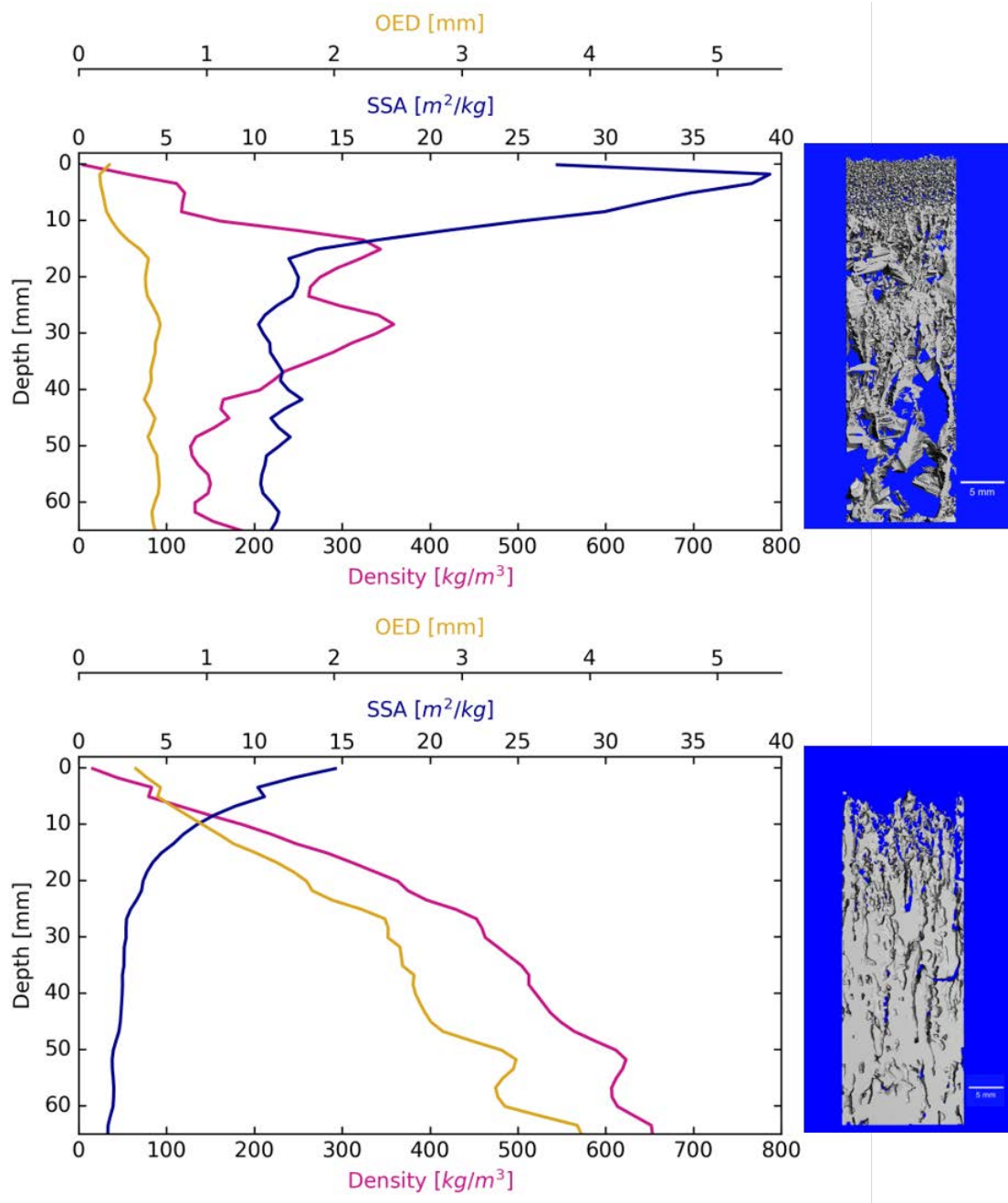


Figure 16: Exemplary vertical profiles of the sea ice surface and snow during winter and summer.

Overview of the MOSAiC expedition – Snow and Sea Ice

Supplemental material

Content of this document

Text S1	Sea ice and snow work and concept
Text S2	Methods and field setup details
	Sea ice coring
	Remotely Operated Vehicle (ROV)
	On-ice remote sensing
	Sea ice drift forecast
	Technological challenges
	References

S1 Sea ice and snow work and concept

The realization of the field program by the highly interdisciplinary ICE team required an extraordinary amount of coordination and interaction. This effort succeeded and initiated manifold new collaborations and scientific exchange. One of the main challenges was to ensure consistency in methodology and data quality of the individual observations over the year, typically including four to five different principal investigators on board and large teams on land, covering a broad range of expertise and specific questions to the same data set. As a result, the task structure, as described in Section 2, is not fully consistent as it merges topics, instruments and ice types, but was found to be most practical in the organization of the daily work in the field. This structure mostly represents how different groups structured their work (operational principles) and data sets.

During the field phase, the ICE team was represented with 12 (Leg 1), 14 (Leg 2), 11 (Leg 3), 14 (Leg 4), 11 (Leg5) berths on *Polarstern* and with 9 berths on *Akademik Fedorov* (Leg 1a). In addition, the ICE team was represented by (co-) cruise leaders on Legs 1 and 2 on board of *Polarstern* and Leg 1a on *Akademik Fedorov*. Overall, 66 different persons participated on both ice breakers. Beyond direct participation on board, strong support was given from land before, during and after the field experiment. Overall, approx. 150 people were involved in the snow and sea ice work and contributed in various ways to the planning, design and successful completion of the work program.

A particular preparation phase was based on the broad experience and expertise across the participating researchers. A main process was the agreement on observational protocols for all field tasks and methods prior to the expedition. Additional workshops and training programs for team members were critical components in preparation for the field experiment. Week-long field training courses were held to cross train team members on the full suite of snow and sea ice measurement protocols and to perform dedicated instrument tests. These courses were held in Hailuoto, Finland (February 22 to March 07, 2019) and Utqiagvik, Alaska (April 07 to 13, 2019). More specialized trainings were performed for flight training and system testing (particularly for navigation systems) for the unmanned aerial systems near

Longyearbyen in April 2019. Various cross-calibration initiatives were also realized before and after the field phase.

During the drift, the daily work was organized along weekly plans with designated time slots per task. Each team member was assigned specific tasks on each day of the week. The same task was mostly carried out by the same people throughout each leg to maintain the highest possible consistency. The work on board was supported by the task members at home, especially by those who carried out the same measurements on earlier or later legs. Snow and sea ice tasks in the field were often supported by volunteers from the other scientific teams as well as by the logistics team. Intense observation periods or case studies were incorporated into the weekly routine to increase the spatial and/or temporal resolution of existing tasks or to capture certain events. A more detailed definition of events during MOSAiC is under development by the project coordinators. An example of an intense observation period is also discussed in Section 4.2.

Figure S1 shows how the work from the different tasks was distributed over the respective week. In addition to the task work (colored time slots), approximately 1/3 of the time slots were used for data work, basic tasks incl. supplemental observations, additional work without immediate task relation (FLEX time), and free time. The week of July 06, 2020, included an intensive observation period of a 24-hour continuous sampling to capture the diurnal cycle under polar day conditions, complementing a similar study during polar night on Leg 1. The different schedules for both case studies demonstrate the general realization of the work program organized through specific tasks over the entire year. The comparison of these two weeks shows how the weekly plans changed over seasons: additional optical measurements ('OPTICS') were carried out under daylight conditions. The rapid changing surface conditions daily snow pit (including surface properties), very frequent 'TRANSECT' and additional 'POND' work in July. The remote sensing work ('REMOTE') was allocated more time in January, for example when a larger suite of instruments was operated on the ice. Different project and process related foci were realized on individual legs like 'RIDGE' and 'POND' work in summer (Leg 4) or 'DYNAMICS' work in winter (Leg 2). The concept of 'FLEX' time, time that was not pre-allocated before the respective leg, turned out to be most beneficial and at the same time essential to enable the planned work program. This time allowed reaction on the continuous changes and challenges in the field. Also allocating sufficient time for in-field data documentation and early processing, as well as dedicated time slots for laboratory work were budgeted and needed. Pre-assigned half days off on Sunday mornings, or on other days when applicable, paid off given the long field phases and continuous high workloads.

Week 20-26 January

Morning						
Monday	Tuesday	Wednesday	Thursday	Friday	Saturday	Sunday
DATA	DATA	DATA	DATA	DATA	DATA	FREE
DATA	DATA	DATA	DATA	DATA	DATA	FREE
DATA	DATA	DATA	STAKES	DATA	DATA	FREE
DATA	LAB	SNOW	STAKES	DATA	LAB	FREE
DATA	LAB	SNOW	STAKES	SNOW	ROV	FREE
HELI	HELI	SNOW	DYNAMIC	SNOW	ROV	FREE
CORES	STAKES	STAKES	DYNAMIC	SNOW	ROV	FREE
CORES	STAKES	STAKES	DYNAMIC	SNOW	LIDAR	FREE
SNOW	STAKES	DYNAMIC	REMOTE	RIDGES	LIDAR	FREE
SNOW	ROV	DYNAMIC	REMOTE	RIDGES	DYNAMIC	FREE
SNOW	ROV	REMOTE	REMOTE	RIDGES	DYNAMIC	FREE
SNOW	ROV	REMOTE	REMOTE	RIDGES	REMOTE	FREE
REMOTE	ROV	REMOTE	REMOTE	REMOTE	REMOTE	LIDAR
REMOTE	DYNAMIC	REMOTE	REMOTE	REMOTE	REMOTE	LIDAR

Afternoon						
Monday	Tuesday	Wednesday	Thursday	Friday	Saturday	Sunday
DATA	DATA	FLEX	HELI	BASIC	DATA	FLEX
DATA	DATA	FLEX	DYNAMIC	DATA	DYNAMIC	FLEX
CORES	DATA	FLEX	DYNAMIC	SNOW	DYNAMIC	FLEX
CORES	LAB	BASIC	DYNAMIC	SNOW	DYNAMIC	FLEX
HELI	LAB	DATA	TRANSECT	SNOW	DYNAMIC	FLEX
SNOW	LAB	DATA	TRANSECT	RIDGES	LIDAR	FLEX
SNOW	HELI	DATA	TRANSECT	RIDGES	LIDAR	FLEX
SNOW	ROV	DATA	TRANSECT	RIDGES	ROV	FLEX
SNOW	ROV	DYNAMIC	TRANSECT	RIDGES	ROV	FLEX
SNOW	ROV	DYNAMIC	TRANSECT	REMOTE	ROV	FLEX
REMOTE	DYNAMIC	REMOTE	TRANSECT	REMOTE	REMOTE	FLEX
REMOTE	DYNAMIC	REMOTE	TRANSECT	REMOTE	REMOTE	FLEX
REMOTE	REMOTE	REMOTE	TRANSECT	REMOTE	REMOTE	FLEX
REMOTE	REMOTE	REMOTE	TRANSECT	REMOTE	REMOTE	FLEX

Week 6-12 July

Morning						
Monday	Tuesday	Wednesday	Thursday	Friday	Saturday	Sunday
FLEX	FLEX	FLEX	FLEX	FLEX	FLEX	FREE
BASIC	BASIC	BASIC	FLEX	FLEX	FLEX	FREE
BASIC	BASIC	BASIC	FLEX	FLEX	FLEX	FREE
HELI	LAB	LAB	BASIC	FLEX	BASIC	FREE
CORES	HELI	HELI	BASIC	FLEX	BASIC	FREE
CORES	SNOW	SNOW	LAB	BASIC	LAB	FREE
CORES	ROV	DYNAMIC	HELI	BASIC	LAB	FREE
SNOW	ROV	PONDS	DYNAMIC	HELI	LAB	FREE
STAKES	ROV	PONDS	RIDGES	STAKES	HELI	FREE
STAKES	PONDS	STAKES	RIDGES	STAKES	SNOW	FREE
STAKES	PONDS	STAKES	RIDGES	RIDGES	OPTICS	FREE
STAKES	DYNAMIC	OPTICS	RIDGES	RIDGES	OPTICS	FREE
REMOTE	REMOTE	REMOTE	RIDGES	TRANSECT	REMOTE	FREE
REMOTE	REMOTE	REMOTE	PONDS	TRANSECT	REMOTE	FREE

Afternoon						
Monday	Tuesday	Wednesday	Thursday	Friday *	Saturday **	Sunday
HELI	FLEX	FLEX	FLEX	FLEX	FLEX	FLEX
CORES	BASIC	FLEX	BASIC	FLEX	FLEX	FLEX
CORES	DATA	FLEX	DATA	FLEX	BASIC	FLEX
CORES	LAB	BASIC	HELI	BASIC	DATA	FLEX
PONDS	HELI	BASIC	SNOW	DATA	HELI	FLEX
PONDS	ROV	BASIC	LIDAR	HELI	LIDAR	FLEX
STAKES	ROV	DATA	LIDAR	SNOW	LIDAR	FLEX
STAKES	ROV	LAB	RIDGES	ROV	ROV	FLEX
TRANSECT	OPTICS	HELI	RIDGES	ROV	ROV	FLEX
TRANSECT	OPTICS	SNOW	RIDGES	ROV	ROV	BASIC
OPTICS	OPTICS	TRANSECT	PONDS	OPTICS	PONDS	DATA
OPTICS	SNOW	TRANSECT	PONDS	OPTICS	PONDS	HELI
REMOTE	TRANSECT	PONDS	REMOTE	REMOTE	OPTICS	OPTICS
REMOTE	TRANSECT	PONDS	REMOTE	REMOTE	OPTICS	DYNAMIC

*24-hour sampling period began; **24-hour sampling period ended

Figure S1: Weekly work plans for snow and sea ice observations.

Schematics from the weeks starting January 20, 2020, (left) and starting July 6, 2020, (right). Each line represents one person. Workdays were split into morning and afternoon blocks. Colors are consistent with the sites in Figure 2. Abbreviations refer to the tasks, as described in Section 2 of the main manuscript, in addition the following terms are used: 'FLEX' for flexible tasks, 'DATA' for data documentation and processing, 'BASIC' for routine work, 'LAB' for (freezer) laboratory work.

S2 Methods and field set-up details

The MOSAiC snow and sea ice program was based on a large number of specialized instruments and methods, which are usually referred to in abbreviations or acronyms. In addition, the field work concept included terminology (and abbreviations) that are unknown to many external readers. All these terms are compiled in Table S1 to ease reading of the manuscript. Abbreviations for all remote sensing instruments are given in Table 2 in the main text; here only names mentioned in the text are listed.

Table S1: Instrument names and abbreviations used in the text.

Short name	Full name / description
ALS	Airborne Laser Scanner
ARIEL	Airborne Radiometer in L-band / used on a mobile sled on transects
CO	Central Observatories (existence of CO1 to CO3)
DN	Distributed Network (existence of DN1 and DN2)
EM	Electro Magnetic
EM-Bird	Helicopter-towed electro-magnetic sounding instrument
FYI	First Year (sea) Ice
GEM	EM induction sounding instrument
GNSS (-R)	Global Navigation Satellite System (and Reflectrometry)
HELiPOD	Helicopter-towed atmospheric sensor suite
HUTRAD	Helsinki University of Technology Radiometer / Microwave radiometer at Remote Sensing site
IMB	(Sea) Ice Mass-balance Buoy
IR	Infrared
LIDAR	Light detection and ranging
Micro-CT	X-ray Micro Computer Tomograph
MOSAiC	Multidisciplinary drifting Observatory for the Study of Arctic Climate
NIR	Near Infrared
ROV	Remotely Operated Vehicle
RS	Remote Sensing
SAR	Synthetic Aperture Radar
SCAT	Scatterometer
SMP	Snow Micro Pen
SSL	Surface Scattering Layer
SYI	Second Year (sea) Ice
TIR	Thermal Infrared
TLS	Terrestrial Laser Scanner
UHI	Underwater Hyperspectral Imager

Sea ice coring

Photographs of the conditions at the coring sites from winter and early summer are shown in Figure S2. The sea ice data used to create Figure 15, is given in Tables S2 and S3.

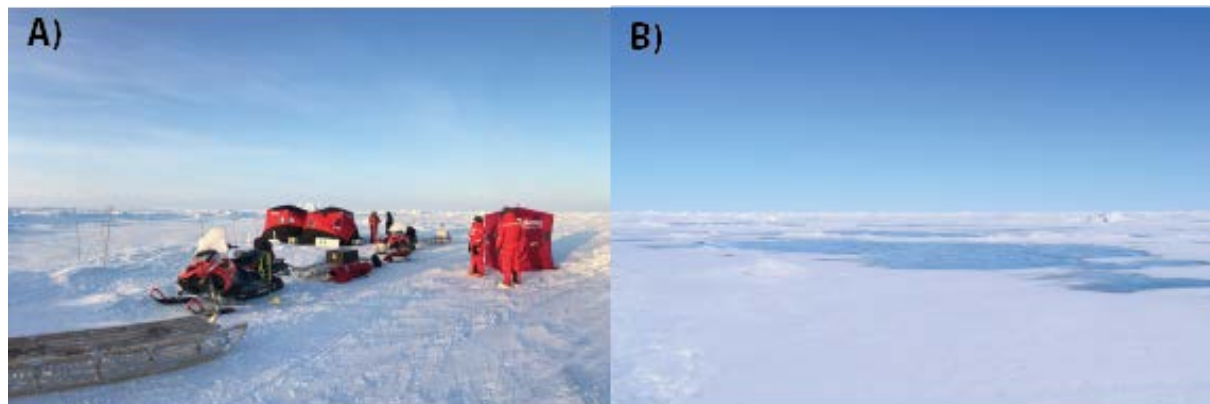


Figure S2: Sea ice coring sites.

Photographs of the coring site during (A) Leg 3 on March 21, 2020, and (B) Leg 4 on June 22, 2020. The photo from the spring Leg 3 also shows the shelters that were temporarily set up for the coring work.

Table S2: Sea ice core data: winter

Salinity (S) and temperature (T) profile for first year (FYI) and second year (SYI) of the 1_10 coring event on December 02, 2019. The upper (z_0) and lower (z_1) boundary of the salinity section depth, and the depth of temperature measurements (z) are given in m relatively to the ice surface. The graph is shown in Figure 16.

FYI			SYI						
z_0 m	z_1 m	S -	z m	T °C	z_0 m	z_1 m	S -	z m	T °C
0.000	0.050	6.9	0.025	-15.3	0.000	0.050	0.9	0.025	-8.3
0.050	0.100	5.8	0.075	-13.0	0.050	0.100	0.5	0.125	-7.8
0.100	0.150	5.9	0.175	-12.0	0.100	0.150	0.9	0.225	-6.5
0.150	0.200	4.1	0.275	-8.5	0.150	0.200	1.1	0.325	-6.1
0.200	0.250	3.5	0.325	-7.4	0.200	0.250	1.2	0.375	-6.2
0.250	0.310	4.8	0.375	-7.1	0.250	0.290	2.4	0.425	-5.8
0.310	0.360	4.8	0.425	-6.4	0.290	0.350	2.3	0.545	-5.0
0.360	0.410	4.8	0.475	-5.5	0.350	0.400	3.9	0.645	-4.3
0.410	0.455	4.5	0.525	-5.3	0.400	0.450	1.7	0.745	-3.3
0.455	0.500	5.5	0.625	-3.1	0.450	0.500	1.2	0.845	-1.9
0.500	0.550	4.6	0.675	-2.3	0.500	0.550	3.1	0.870	-1.7
0.550	0.600	4.7	0.695	-1.9	0.550	0.600	1.6		
0.600	0.650	5.6			0.600	0.650	1.2		
0.650	0.705	7.9			0.650	0.700	1.5		
					0.700	0.750	3.4		
					0.750	0.800	4.3		
					0.800	0.850	5.3		
					0.850	0.900	8.0		

Table S3: Sea ice core data: summer

Salinity (S) and temperature (T) profile for first year (FYI) and second year (SYI) of the 4_46 coring event on July 06, 2020. The upper (z_0) and lower (z_1) boundary of the salinity section depth, and the depth of temperature measurements (z) are given in m relatively to the ice surface. The graph is shown in Figure 16.

FYI			SYI						
z_0 m	z_1 m	S -	z m	T °C	z_0 m	z_1 m	S -	z m	T °C
0.000	0.050	0.2	0.025	-0.1	0.000	0.050	0.2	0.025	0.1
0.050	0.105	0.3	0.050	0.1	0.050	0.100	0.0	0.125	0.5
0.105	0.160	0.3	0.150	0.0	0.090	0.150	0.0	0.225	0.0
0.160	0.210	0.8	0.250	-0.1	0.140	0.200	0.1	0.325	0.0
0.210	0.260	1.9	0.350	-0.5	0.190	0.250	0.1	0.425	0.0
0.260	0.310	2.8	0.450	-0.7	0.240	0.300	0.1	0.525	0.0
0.310	0.360	3.3	0.550	-0.6	0.290	0.350	0.1	0.625	0.0
0.360	0.410	3.6	0.650	-1.0	0.340	0.400	0.1	0.725	0.0
0.410	0.460	3.8	0.750	-1.1	0.390	0.450	0.1	0.790	0.0
0.460	0.510	4.3	0.850	-1.2	0.440	0.500	0.1	0.850	0.0
0.510	0.560	4.3	0.950	-1.3	0.490	0.550	0.1	0.925	0.0
0.560	0.610	4.9	1.050	-1.4	0.540	0.600	0.1	1.025	-0.1
0.610	0.660	4.1	1.150	-1.1	0.590	0.650	0.1	1.100	0.0
0.660	0.710	4.3	1.250	-1.1	0.640	0.700	0.2	1.150	-0.1
0.710	0.760	4.3	1.350	-0.9	0.690	0.750	0.2	1.225	-0.1
0.760	0.810	4.3	1.450	-0.7	0.740	0.800	0.4	1.325	-0.3
0.810	0.860	4.0	1.550	-0.7	0.790	0.850	0.3	1.425	-0.2
0.860	0.910	4.0	1.620	-0.5	0.840	0.900	0.1	1.525	-0.1
0.910	0.960	3.8		0.890	0.950	0.1	1.625	-0.5	
0.960	1.010	3.7		0.940	1.000	0.2	1.725	-0.9	
1.010	1.060	3.9		0.990	1.050	0.2	1.825	-1.0	
1.060	1.110	3.5		1.040	1.100	0.2	1.925	-1.2	
1.110	1.160	3.5		1.090	1.150	0.2	2.025	-1.4	
1.160	1.210	3.6		1.140	1.210	0.2	2.125	-1.4	
1.210	1.260	3.5		1.190	1.260	0.3	2.210	-1.2	
1.260	1.310	3.1		1.240	1.310	0.2			
1.310	1.360	3.2		1.290	1.360	1.1			
1.360	1.410	2.9		1.340	1.410	1.7			
1.410	1.460	3.2		1.390	1.460	1.0			
1.460	1.510	2.6		1.440	1.510	2.3			
1.510	1.545	1.6		1.490	1.560	2.0			
1.545	1.605	2.2		1.540	1.610	0.2			
				1.590	1.660	0.5			
				1.640	1.710	1.1			
				1.690	1.760	1.3			
				1.750	1.810	1.3			
				1.800	1.860	1.4			
				1.850	1.910	3.3			
				1.900	1.960	3.2			
				1.950	2.010	3.4			
				2.000	2.060	3.3			
				2.050	2.110	2.9			
				2.100	2.160	3.1			

Remotely operated vehicle (ROV)

The ROV has been operated from different sites due to the dynamic icescape: Site ROV 1.0 was never used for scientific dives, being immediately replaced by ROV 2.0 during Leg 1 (CO1). Site ROV 3.0 was used on CO1 during Legs 2 and 3, sites ROV 4.0 and 4.5 were operated on CO2 during Leg 4, and site ROV 5.0 was operated on CO3 during Leg 5. Figure S3a shows exemplary photographs of the set up (Leg 2 and Leg 5) and maps to illustrate linkages to other measurements during spring.

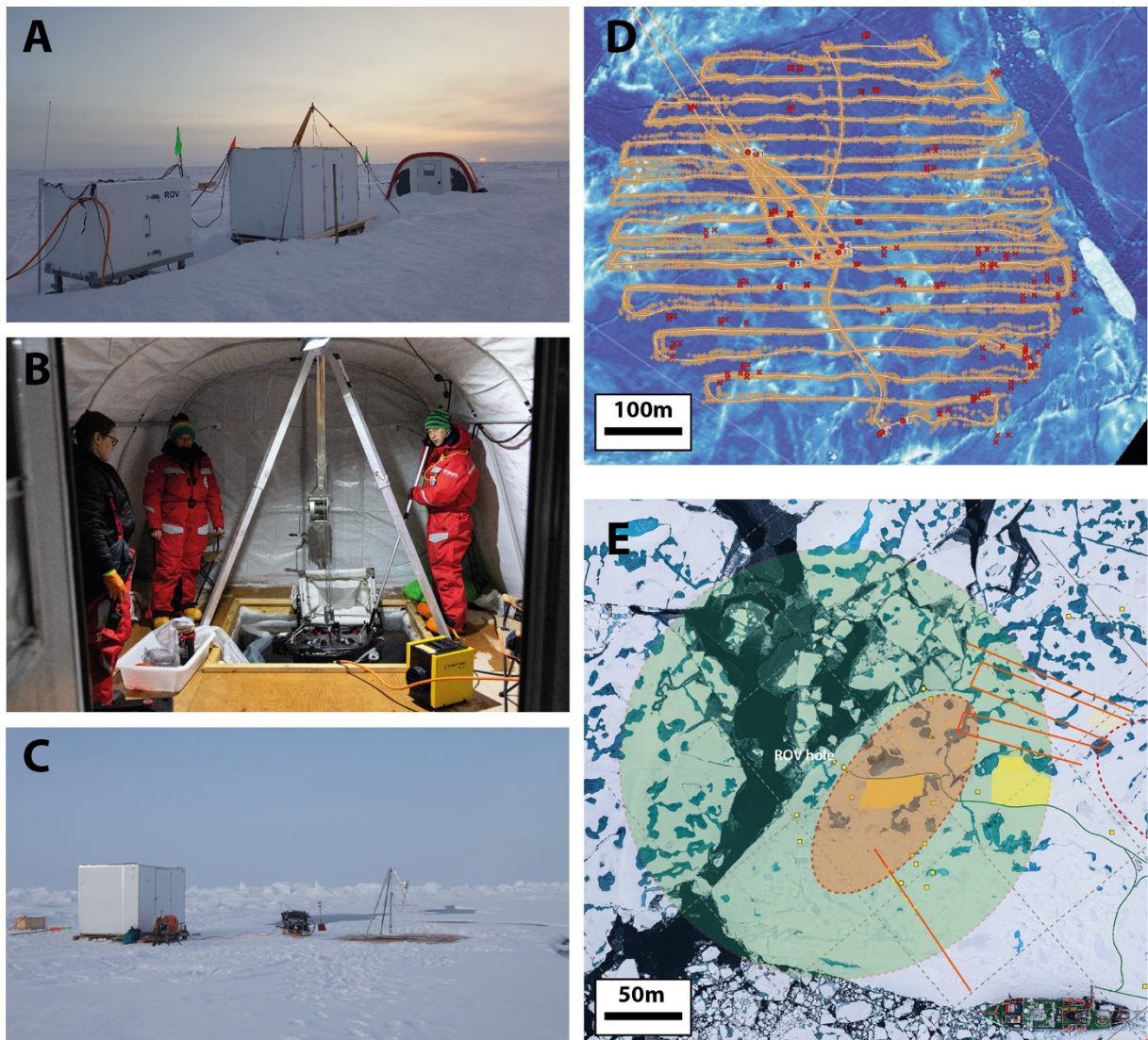


Figure S3: ROV observations.

(A) Remotely operated vehicle (ROV) site consisting of the power hub, the surface unit (white hut), the tent over the hole (photo March 14, 2020), (B) inside the ROV tent (photo December 07, 2019), (C) ROV site consisting of the surface unit and the hole without tent (photo August 25, 2020), (D) dive track (yellow line) and excluded acoustic navigation fixes (red dots) as overlay on the airborne laser scanner topography surface map (dive on February 04, 2020), (E) schematic overview of the ROV dive range (green circle) during autumn (Leg 5, aerial photo from September 06, 2020). Other sites: TLS area in orange ellipse, transects in orange lines, snow and surface studies in yellow patches, other installations and sites as small yellow squares.

On-ice remote sensing

The concept of the on-ice remote sensing measurements was to observe the same snow and sea ice surface, or at least the same surface type, with all instruments. In addition, other manual measurements were co-located on the same site (Figure 2) and ice conditions. Figure S4 shows the arrangement of the individual sensors around the observation site.

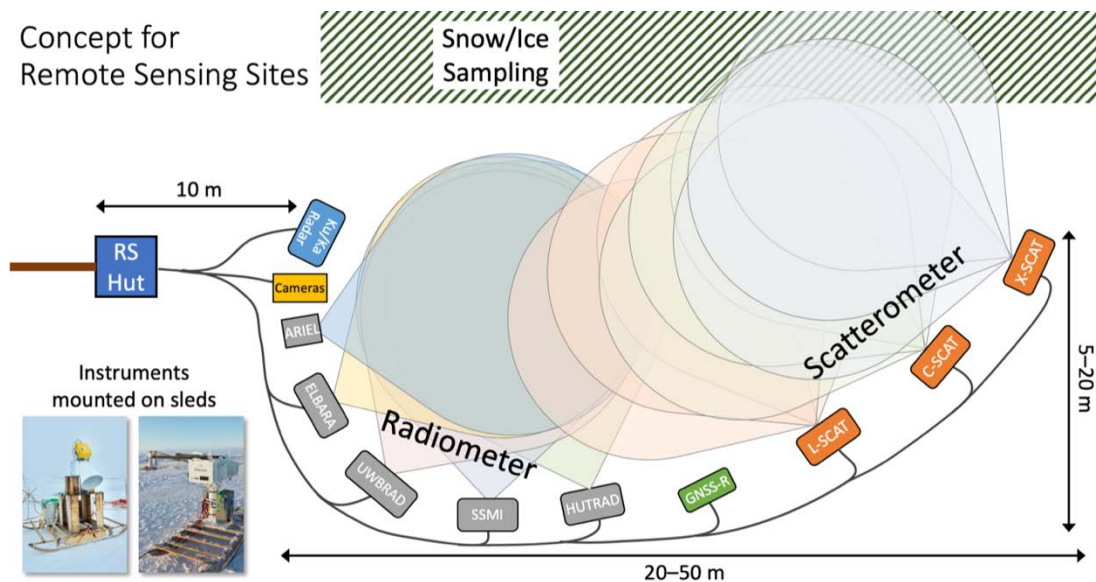


Figure S4: On-ice remote sensing concept.

Conceptual layout used for the Remote Sensing Sites on the MOSAiC ice floe. For comparability all instruments looked at similar ice and snow. Physical ice and snow properties were sampled in the vicinity. Photographs of the Remote Sensing Site are shown in Figure 10. Additional sea ice remote sensing observations were performed from *Polarstern*.

Sea ice drift forecasts

A near-real-time drift forecast product for the MOSAiC floe was provided by the Year of Polar Prediction (YOPP; Jung et al., 2016) Sea Ice Drift Forecast Experiment (SIDFEx). Several operational forecast centers and institutes contributed drift forecasts in near-real-time for lead times ranging from days to a year. For MOSAiC a consensus ensemble forecast product, based on the different forecast systems, was used. Typically, about five different short-term (7–10 days) single-trajectory forecasts, which in particular use recent wind forecasts for driving the ice drift, and one seasonal, climatological forecast were merged into a seamless ensemble forecast. The consensus forecasts were provided onboard *Polarstern* through the MapViewer system to support decision making, and on land through an online tool (<https://sidfex.polarprediction.net>), for placing orders for satellite imagery. Figure S5 exemplifies the consensus forecasts product, showing the forecast issued on February 24, 2020.

Beyond the drift phase, forecast products from fully coupled models were provided on a daily base as well as ensemble predictions of sea ice conditions for the coming months (<https://nps.edu/web/rasm/predictions>). All these sea ice model applications were most supportive for the highly complex logistical operations of the supply vessels. Advancing the fidelity of different models with the hierarchy will allow for the development of optimized

observational networks, as they may be used for sea ice monitoring or advanced field programs in the future.

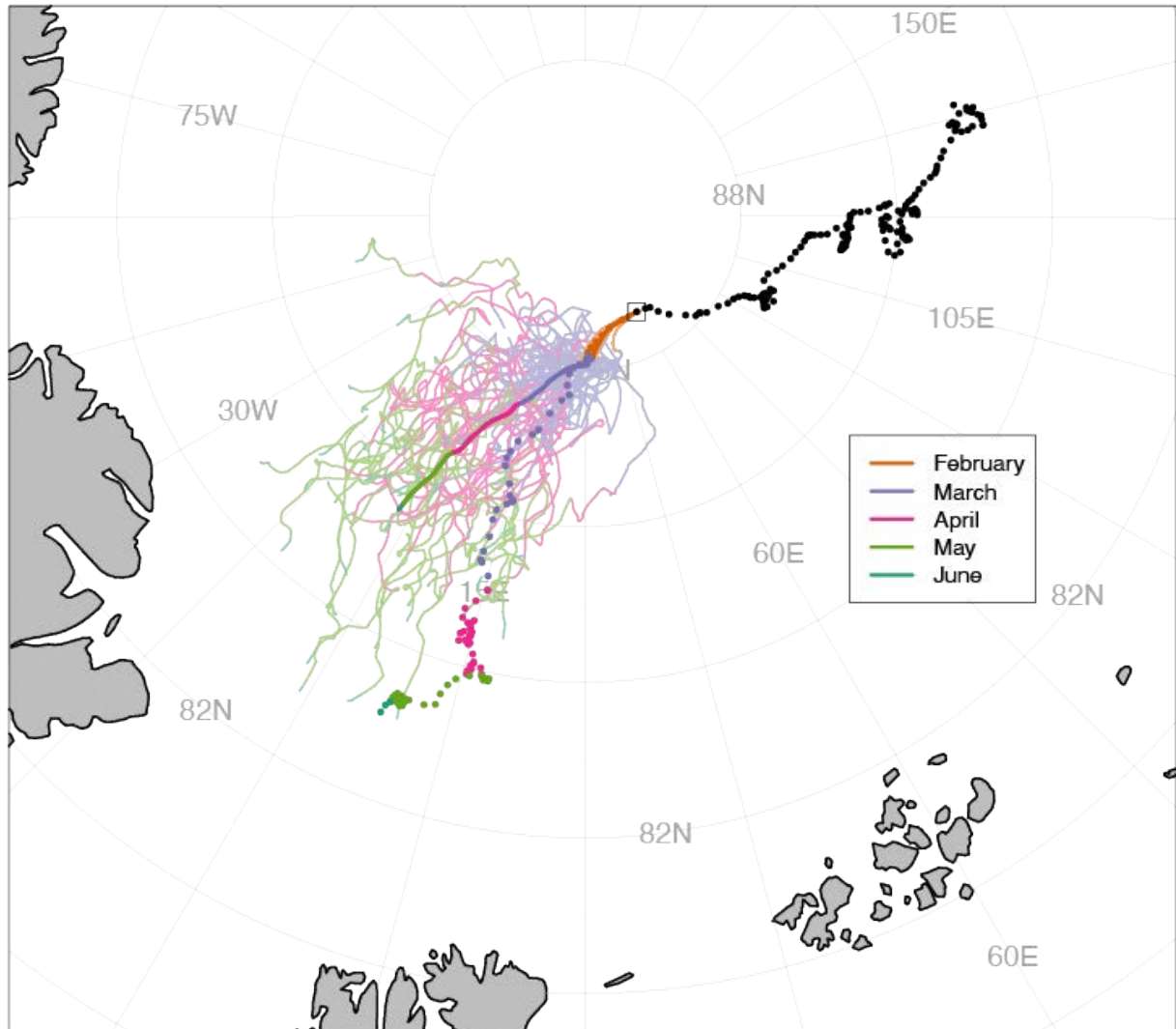


Figure S5: The SIDFEx consensus drift forecast for the MOSAiC central observatory (CO1).

The forecast of the Sea Ice Drift Forecast Experiment (SIDFEx, <https://sidfex.polarprediction.net/>) starts on February 24, 2020, at 00:00 UTC, when Polarstern was at the given position (grey square). Thin solid lines denote individual (merged) forecast ensemble members and the corresponding thick solid line denotes the ensemble mean (centroid). Lines are colored by calendar month. Dots denote daily observed positions of Polarstern before (black) and after (colored by calendar month) February 24, 2020.

Technological challenges

The year-long operations in the central Arctic resulted in specific (technological and methodological challenges), in particular with respect to automated systems.

Challenges were observed in flying the Mavic and Spectra drones close to the North Pole, where operators needed to apply the manual mode because the compass reading was not correct. However, similar problems were not encountered using the HELiX drone, albeit at lower latitudes. Future studies should consider developing and leveraging advanced navigation systems such as the D-GPS navigation employed by the DataHawk unmanned aerial

system deployed to make atmospheric measurements, to avoid the challenges encountered by the Mavic and Spectra copters. In addition to challenges posed by the navigation systems, other factors, including fast ice drift velocities, fog, and icing conditions resulted in a difficult operating environment for drone systems. Despite these challenges, the systems deployed combined to provide unique perspectives on broadband and spectral albedo and their evolution during the melt and refreezing seasons.

Many complex instruments, e.g., most of the remote sensing sensors, were designed for shorter campaigns. Operating them continuously for a full year led to some instrument failures, which only partly could be repaired in the field, and thus led to data gaps or a complete stop of measurements for some channels (Figure 3b). This was partly compensated by the large suite of complementary measurements, but a larger pool of spare parts and more trained personnel could have reduced these downtimes.

References

Jung, T, Gordon, ND, Bauer, P, Bromwich, DH, Chevallier, M, Day, JJ, Dawson, J, Doblas-Reyes, F, Fairall, C, Goessling, HF, Holland, M, Inoue, J, Iversen, T, Klebe, S, Lemke, P, Losch, M, Makshtas, A, Mills, B, Nurmi, P, Perovich, D, Reid, P, Renfrew, IA, Smith, G, Svensson, G, Tolstykh, M, Yang, Q. 2016. Advancing Polar Prediction Capabilities on Daily to Seasonal Time Scales. *B Am Meteorol Soc* **97**(9): 1631-1647.
doi:10.1175/bams-d-14-00246.1.